UNIVERSITÀ DEGLI STUDI DI PAVIA
DOTTORATO DI RICERCA IN FISICA – XXXVII CICLO

Exploring the proton structure with the FAMU experiment: detector performance and first physics results

Riccardo Rossini

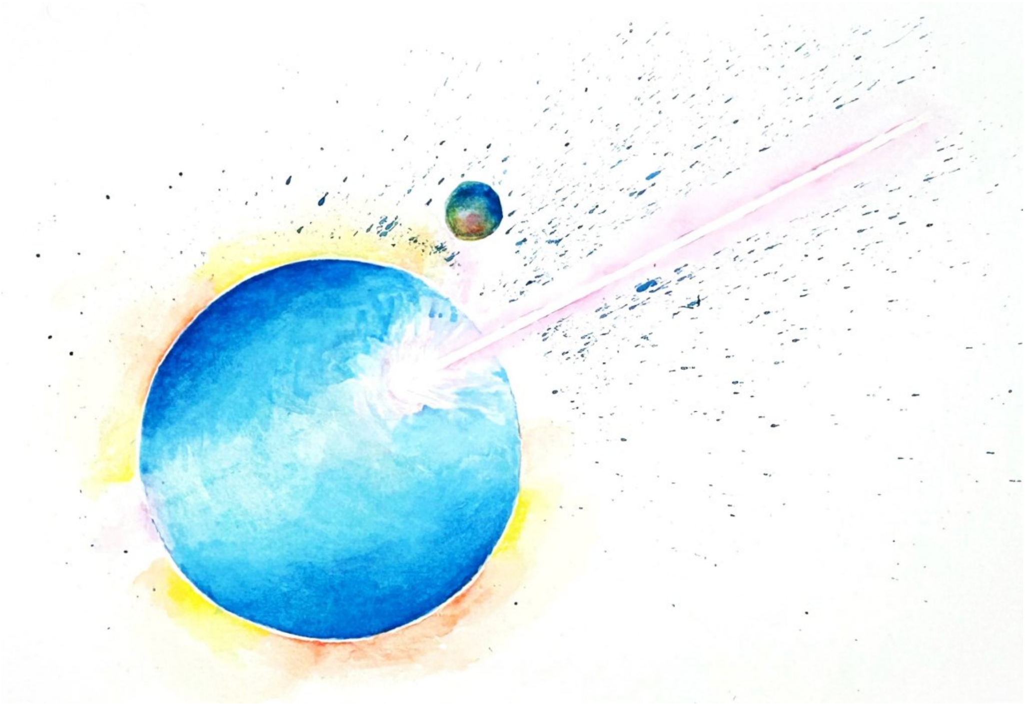

Tesi per il conseguimento del titolo

Università di Pavia
Dipartimento di Fisica

DOTTORATO DI RICERCA IN FISICA – XXXVII CICLO

Exploring the proton structure with the FAMU experiment: detector performance and first physics results

Riccardo Rossini

Submitted to the Graduate School of Physics in partial
fulfilment of the requirements for the degree of
DOTTORE DI RICERCA IN FISICA
DOCTOR OF PHILOSOPHY IN PHYSICS
at the University of Pavia

Supervisors:
Prof. Alessandro Menegolli
Dr. Massimiliano Clemenza

Cover: Muonic target.
Cristina Ferrari, 2024, watercolour on paper.

Exploring the proton structure with the FAMU experiment: detector performance and first physics results
Riccardo Rossini
PhD thesis - University of Pavia
Pavia, Italy, January 2025

Acknowledgements

First and foremost, I would like to express my deepest gratitude to my supervisors Alessandro Menegolli and Massimiliano Clemenza, and the PhD coordinator Daniela Rebuzzi, for their guidance and support throughout my PhD journey. Their insights and feedback made this work possible and greatly contributed to my growth in this field.

I am deeply grateful to the Pavia division of the INFN for providing the funding to my PhD position, as well for covering travel expenses to carry out the research and participate in schools and conferences. I would like to thank the electronics team in Pavia, and specifically Massimo Rossella and Marco Prata.

I would like to extend my thanks to the FAMU team members. In particular, I would like to thank Emiliano Mocchiutti, Cecilia Pizzolotto, Maurizio Bonesini, Roberto Bertoni, Antonello Sbrizzi, Erik Vallazza, and Andrea Vacchi, just to mention the people who helped me the most. Their guidance on different aspects of my work has been enriching and vital. I would also like to thank the laser team, specifically Marco Baruzzo, Luigi Moretti, and Eugenio Fasci, for helping me understand the laser system and its challenges. I am deeply thankful to all the FAMU shifters for the weeks spent at RAL during beamtime, sharing difficulties and successes. I would like to thank Christian Petroselli for our discussions on the hodoscopes.

During my PhD, I also had the privilege of working as a visiting researcher at the University of Milano-Bicocca, in Milan (Italy), and at the ISIS Neutron and Muon Source, in Didcot (UK). I would like to thank all my supervisors in these institutions for their mentorship and support: Daniela Di Martino in Milan; Adrian Hillier, James Lord, Lina Quintieri, and Koji Yokoyama at ISIS. Their contribution and help have been critical during my work.

The reviewers of this tesis, Prof. Francesco Terranova and Prof. Randolf Pohl, are kindly acknowledged for reading the original manuscript and providing valuable insights and interesting suggestions.

I would like to express my deep thanks to my family, my friends, my Italy & UK housemates, and my colleagues: for their advices and support during the last three years.

Contents

Introduction 1

1 Proton radii and muonic atoms 3
- 1.1 Proton charge radius 3
- 1.2 Proton Zemach radius 6
- 1.3 Muonic atom formation and behaviour 10

2 The FAMU experiment 13
- 2.1 Aim and experimental technique 13
- 2.2 FAMU previous experience (2014 – 2018) 15
- 2.3 Muon beam production and delivery 17
- 2.4 Experimental setup 25
  - 2.4.1 Target and optical cavity 25
  - 2.4.2 Laser beam production and delivery 28
  - 2.4.3 X-ray detector setup and performance 30
  - 2.4.4 Data acquisition and trigger system 38

3 Design and characterisation of hodoscopes for high-flux muon beams 41
- 3.1 Hodoscope design and implementation 41
- 3.2 Hodoscope operation and calibration technique 44
  - 3.2.1 Low-flux data reduction with XOR method 46
  - 3.2.2 Low-flux data reduction with time coincidence method 48
- 3.3 Hodoscope simulation 49
  - 3.3.1 Interspaced-fibre hodoscope simulation 49
  - 3.3.2 Adjacent-fibre hodoscope simulation 56
- 3.4 Hodoscope characterisation with low-flux proton beams at CNAO 58
- 3.5 Hodoscope characterisation with low-flux muon beams at RAL 64
- 3.6 Hodoscope operation with high-flux muon beams at RAL 69
  - 3.6.1 Hodoscope linearity and beam focusing check 70
- 3.7 Summary 73

4 FAMU data analysis 75

4.1 FAMU data taking 75

4.1.1 Muon beam performance 76

4.1.2 Laser beam performance 80

4.2 Data analysis workflow 81

4.2.1 On-line data processing: level 2 data and QuickLook . . 82

4.2.2 Off-line level 2 data analysis 87

4.3 Data normalisation 94

4.3.1 Muon beam normalisation 94

4.3.2 Gas condition normalisation 95

4.3.3 Data normalisation summary 102

4.4 X-ray detector performance 103

4.5 Delayed X-ray plots 111

4.6 Summary 117

Conclusion 119

Bibliography 121

List of publications 129

Introduction

My PhD Thesis work has been focused on the activity of the FAMU experiment, aimed at measuring the ground state hyperfine splitting in the muonic hydrogen atom (μH), in order to extract an independent measurement of the Zemach radius of the proton.

The scientific case is introduced in Chapter 1. The field of proton radii re-gained interest in the last 15 years thanks to a new measurement of the proton charge radius, about 7σ away from the CODATA2014 accepted value, measured by the CREMA experiment at PSI by evaluating the Lamb Shift in μH. While the charge radius is only dependent on the electric form factor, the Zemach radius takes into account both the electric and magnetic internal structure of the proton.

The FAMU experimental method and setup are described extensively in Chapter 2. The experiment is being carried out at the RIKEN-RAL Port 1 muon beamline at the ISIS Neutron and Muon Source in Didcot, United Kingdom. The μH atoms are created by injecting a negative muon beam in a pressurised gas target containing hydrogen with a contamination of oxygen. A custom-made laser system with variable wavelength is injected in the chamber to excite the spin flip in μH atoms. The observable consists in an excess of delayed muonic oxygen (μO) X-rays resulting from an enhanced muon transfer probability following the transition. The aim of the experiment is to look for a resonance in this observable as a function of the laser wavelength. The spectral region of interest for the experiment is 100-200 keV. For this reason, the detection setup consists in a set of scintillating crystals surrounding the pressurised target, complemented by a germanium detector for inter-calibration. During my PhD work, I have participated in person in all the phases of commissioning and data acquisition of the experiment.

The main detector studied in this work is the muon beam monitor, which is the focus of Chapter 3. It consists in a scintillating fibre hodoscope which is currently being used also as a flux-meter thanks to the extensive calibration and simulation work hereby presented. The calibration consisted in low-flux measurements to extract the response of a single particle and compare it to the simulated response function, to construct a high-flux response function used for the muon flux estimation. The simulation work was carried out in Geant4 and compared to a model developed with FLUKA-CERN. The work proposed for my thesis, in particular regarding the beam monitor, has been evaluated as crucial for the Collaboration and the success of the experiment. This allowed me to get assigned some of the FAMU allocated beamtime to carry out the studies on the hodoscope described in Chapter 3.

Finally, the FAMU data analysis workflow is presented in Chapter 4, with a specific focus on the muon beam normalisation and quality control carried out with the FAMU beam monitor. The data selection and data analysis on the scintillating detectors is also presented and coupled with the information from the hodoscope to fully characterise and double-check the incoming beam and the setup itself. The ongoing and future steps of data analysis towards the final resonance plot are also presented and discussed.

In Conclusion, the work developed for my PhD Thesis consisted in a wide overview on the FAMU experiment and its hardware and analysis framework. In particular, I developed an innovative method for the extraction of the absolute flux of a high intensity muon beam based on data from a custom beam monitor, initially designed by INFN Pavia and Milano-Bicocca only as a beam shape monitor. This information was fundamental in developing analysis tools I studied for the normalisation of FAMU data. Lastly, I spent part of my PhD work analysing FAMU $LaBr_3$ detector data within the FAMU Analysis Group in order to develop the method to extract the observable, *i.e.* the number of delayed μO X-rays as a function of the injected laser wavelength, which is linked to the μH ground state hyperfine splitting, and therefore to the final goal of the proton Zemach radius.

The research presented in this Thesis has been primarily conducted at the University of Pavia and the INFN Pavia Division, the latter being the funding institution for the PhD. During my doctoral studies, I was hosted as a Visiting PhD Candidate at the ISIS Neutron and Muon Source (Didcot, UK), where the experiment is located, and at the University of Milano-Bicocca, where much of the detector development was carried out.

Chapter 1

Proton radii and muonic atoms

After a brief introduction on the electron-proton (*ep*) scattering, Section 1.1 is centred on the proton radius and specifically on the *proton radius puzzle*, a problem that prompted the research in this field for the last 15 years. The following section (1.2), instead, is focused on the Zemach radius of the proton, which is currently one of the frontiers in the field of proton radius precision measurements. This is also the parameter that the FAMU experiment aims at measuring. Lastly, Section 1.3 is focused on muonic atoms, which proved to be a turning point in the proton radius puzzle, and which are currently being exploited by all experiments looking for the Zemach radius of the proton, including FAMU.

1.1 Proton charge radius

The scattering of electrons against a target of protons, also noted as *ep* scattering, was one of the first activities carried out with particle accelerators. If the electron energy is higher than a few GeV, the Rutherford approximation of elastic scattering doesn't hold. This was interpreted assuming that the electron interacts with the inner components of the proton, which thus can not be considered an elementary particle. Such process is called Deep Inelastic Scattering (DIS)[1, 2]. The differential cross section for the elastic *ep* scattering was written in the 1950's, with an original contribution from Marshall Rosenbluth[3, 4], as:

$$\frac{d\sigma}{d\Omega} = \underbrace{\frac{4\alpha^2 E'^2 \cos^2(\vartheta/2)}{(Q^2)^2}}_{\substack{\sigma_{\text{Mott}}(Q^2) \\ ep \text{ with point-like proton}}} \; \frac{E'}{E} \; \underbrace{\left[\frac{G_E^2 + \tau G_M^2}{1+\tau} + 2\tau G_M^2 \tan^2(\vartheta/2)\right]}_{\substack{G(Q^2) \\ \text{internal proton structure}}}, \tag{1.1}$$

where Q^2 is the squared momentum transfer between the incoming elecron and the target proton, $\alpha = e^2/(4\pi\varepsilon_0\hbar c)$ is the fine-structure constant, E and E' are the initial and final (respectively) kinetic energy of the electron, $\tau :=$

$Q^2/(4M_p^2)$, M_p is the mass of the proton, and ϑ is the scattering angle. The electric form factor G_E was defined in order to encapsulate the underlying electric properties of the interaction, and the magnetic form factor G_M is the analogous for magnetic properties. In non-relativistic picture, they correspond to the Fourier transforms of the spatial density of electric charge and magnetic dipoles, respectively. This expression is convenient because it allows to extract the electric and magnetic form factors through the following approximations, referred to as the *Rosenbluth separation*:

$$\begin{aligned} \text{big } Q^2 \text{ (big } \vartheta) &\Rightarrow \frac{d\sigma}{d\Omega} \propto G_M(Q^2); \\ \text{small } Q^2 \text{ (small } \vartheta) &\Rightarrow \frac{d\sigma}{d\Omega} \propto G_E^2(Q^2) + \tau G_M^2(Q^2). \end{aligned}$$

As a consequence, wide angle data allow to extract G_M, which can then be used to extract G_E at small angles by extrapolation and subtraction.

The most convenient definition for the proton radius is based on the electric structure only and it is therefore called the *charge radius*[1]:

$$r_E^2 := -6 \left. \frac{dG_E}{dQ^2} \right|_{Q^2 \to 0} . \tag{1.2}$$

As a consequence, the most straightforward way to measure the proton charge radius is to exploit the Rosenbluth separation to extract a precise estimation of $G_E(Q^2)$ at different values of $Q^2 \to 0$, i.e. $\vartheta \to 0$ in order to extrapolate the value of r_E^2 using Equation 1.2.

The second way to measure this parameter is through atomic spectroscopy, specifically by measuring the hydrogen Lamb shift, i.e. the energy difference between the atomic levels ${}^2S_{1/2}$ and ${}^2P_{1/2}$. By defining the k^{th} *moment of the electric charge density* $\rho_E(r)$ as:

$$\langle r_E^k \rangle := 4\pi \int_0^{+\infty} dr \; r^{k+2} \rho_E(r), \tag{1.3}$$

it can be proved that the charge radius of the proton can be written as the square root of the second moment, i.e. $r_E = \sqrt{\langle r_E^2 \rangle}$. By introducing also the *third Zemach moment*:

$$\langle r_E^3 \rangle_{(2)} := \frac{48}{\pi} \int_0^{+\infty} \frac{dQ}{Q^4} \left[G_E^2(Q^2) - 1 + \frac{1}{3} \sqrt{\langle r_E^2 \rangle} Q^2 \right], \tag{1.4}$$

and defining the related *Friar radius* $r_F = \sqrt[3]{\langle r_E^3 \rangle_{(2)}}$, one can finally write the proton finite-size contribution to the Lamb shift for hydrogen as:

$$\Delta E_L^{fs} = \frac{\alpha^4 M_r^3}{12} r_E^2 - \frac{\alpha^5 M_r^4}{24} r_F^3, \tag{1.5}$$

where M_r is the reduced mass of the proton-lepton system and the best estimation for the Friar radius is $r_F^3 = 2.85(8)$ fm^3, obtained from *ep* scattering in Mainz[5].

All accepted measurements carried out before 2010 were in agreement and concurred in the CODATA-2010[6] recommended value for the proton charge radius $r_E = 0.8775(51)$ fm. This value was debated after measurements of Lamb shift of muonic hydrogen carried out by the CREMA Collaboration, which returned the value $r_E = 0.84087(39)$ fm[7, 8], having a discrepancy of 7 standard deviations from the CODATA-2010 recommended value. This discrepancy can not be blamed on the Friar radius contribution, as it would need $r_F^3 = 37(7)$ fm^3[9], while it has been proved that $r_F^3 < 4.5$ fm^3[10]. Other similar hypotheses of relevant contributions in this measurement were rejected. In addition, the first results of the PRad experiment[11], specifically designed to explore the scattering cross section at extremely low Q^2, were published in 2019 and returned $r_E = 0.831(14)$ fm, in agreement with the CREMA result and not (by 3σ) with the value recommended by CODATA-2010. Further data acquisition and data analysis are ongoing and a more accurate result should be available in the next years. In addition, some *ep* scattering re-analyses and new hydrogen spectroscopy returned values consistent with the new estimation.

For these reasons, the CODATA-2018[12] recommended value for the proton charge radius is $r_E = 0.8414(19)$ fm, consistently with the new values obtained in the last years with both atomic spectroscopy and *ep* scattering.

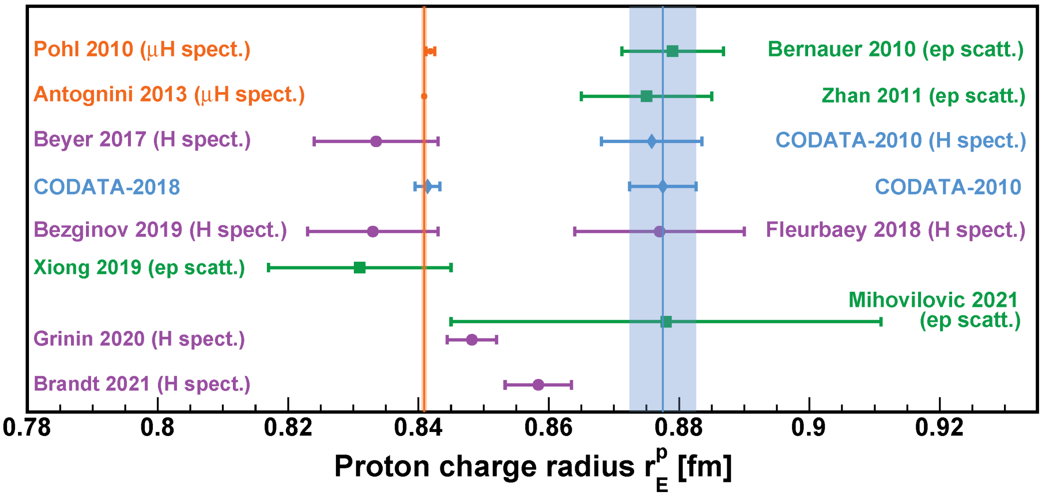

Figure 1.1: *Some of the latest estimations of the proton charge radius from ep scattering[11, 13–15] (green squares), ordinary hydrogen spectroscopy[16–20] (purple circles) and muonic hydrogen spectroscopy[7, 8] (orange dots). The CODATA-2010[6] and CODATA-2018[12] recommended values are also reported (blue diamonds). The coloured bands highlight the comparison between the value from CODATA-2010 (blue, right) and the best estimation given by the CREMA experiment in 2013 (orange, left), which is considered the starting point of the proton radius puzzle. Taken from [21].*

1.2 Proton Zemach radius

In order to define the Zemach radius[1, 2], it is important to understand the nature of the ground state hyperfine splitting (*1S-hfs*). It is defined as the energy shift between the singlet (total spin $F = 0$) and the triplet (total spin $F = 1$) states of the hydrogen ground state $^1S_{1/2}$. Similarly to the previous case, the *magnetic radius* and the k^{th} *moment of the magnetic dipole density* $\rho_M(r)$ are defined respectively as:

$$r_M^2 := -6\, \frac{dG_M}{dQ^2}\bigg|_{Q^2\to 0}, \tag{1.6}$$

$$\langle r_M^k \rangle := 4\pi \int_0^{+\infty} dr\ r^{k+2} \rho_M(r), \tag{1.7}$$

where it can be proved that $r_M = \sqrt{\langle r_M^2 \rangle}$. However, when calculating the hyperfine splitting for hydrogen the first and second order contributions in r_M cancel out, and the first non-zero term is a function of the *Zemach radius*, defined as:

$$r_Z := -\frac{4}{\pi}\int_0^{+\infty} \frac{dQ}{Q^2}\left[\frac{G_E(Q^2)G_M(Q^2)}{1+\kappa_N} - 1\right] = \int r d^3r \int d^3r' \rho_E\left(\vec{r} - \vec{r'}\right)\rho_M\left(\vec{r}\right), \tag{1.8}$$

where κ_N is the anomalous magnetic moment of the proton, i.e. its magnetic moment is given by $G_M(0) = 1 + \kappa_N$. The latest theoretical predictions for the proton Zemach radius are shown in Figure 1.3.

As one can see, this definition of the radius is the convolution of the electric and magnetic space density distributions and it therefore takes into account of both form factors. An accurate measurement of the hyperfine splitting in muonic atoms would therefore allow a precise estimation of the proton Zemach radius, for reasons that can be better understood in Section 1.3. Three collaborations are currently attempting this measurement with different experimental methods, all based on the production of muonic hydrogen[2]: one at PSI in Switzerland (CREMA[22]), one at RIKEN-RAL in the United Kingdom (FAMU[23], on which this work is based) and one at J-PARC in Japan[24]. A scheme of the three experiments is shown in Figure 1.2.

More specifically, this work is focused on the FAMU experiment, which consists in injecting a pulsed muon beam in a mixture of hydrogen and oxygen and looking for an enhanced probability of muon transfer from H to O due to a kinetic energy excess following the excitation of *1S-hfs* with a MIR laser. The details on the experimental method and its implementation in FAMU are presented in Chapter 2.

On the other hand, the CREMA (Charge Radius Experiment on Muonic Atoms) Collaboration, after their measurements of the proton charge radius in the past years, are currently working on *1S-hfs* spectroscopy on μH[22] at

PSI. The experiment is carried out with a continuous muon beam and a muon-triggered MIR laser with a narrow (2 mm) pure hydrogen target. The transfer process exploited is the collision with the gold walls of the chamber, therefore the emission of delayed muonic gold (μAu) characteristic X-rays.

Finally, a group at the J-PARC muon source, in Japan, is working on a third experiment in this field based on detecting angular anomalies in the emission of decay electrons for polarised μH atoms[24].

Experiment	**FAMU** @RAL (UK) by INFN (IT)	**CREMA** @PSI (CH)	@J-PARC (JP)
Scheme	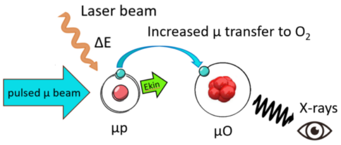	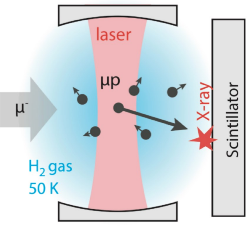	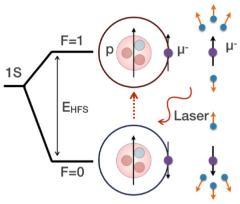
Mechanism	Transfer to O_2	Diffusion to Au walls	Asymmetry
Detection	X-rays	X-rays	Electrons
Muon beam	Pulsed	Continuous	Pulsed

Figure 1.2: *Scheme of the three experiment looking for 1S-hfs in μH to determine the proton Zemach radius. Experiment schemes adapted from [22, 25, 26].*

The dependence between the proton Zemach radius and the ground state hyperfine splitting in μH, can be written as[2]:

$$E_{1\text{S-}hfs}(\mu\text{H}) = \left[A - B\left(\frac{r_Z}{\text{fm}}\right) + C\right]\text{meV}, \tag{1.9}$$

where the latest values for the coefficients are:

$$A = \underbrace{182.443}_{\substack{E_F\\ \text{Fermi energy}}} + \underbrace{1.350(7)}_{\text{QED+weak}} + \underbrace{0.004}_{\text{hVP}}; \tag{1.10}$$

$$B = 1.30653(17); \tag{1.11}$$

$$C = \underbrace{182.443}_{\substack{E_F\\ \text{Fermi energy}}} \left[1.01656(4)\ \underbrace{\Delta_{\text{recoil}}}_{0.000846(6)} + 1.00402 \cdot \underbrace{\Delta_{\text{pol}}}_{0.0004}\right]. \tag{1.12}$$

The first term A contains the Fermi energy, the QED and weak interaction corrections, and the hadronic vacuum polarization, whereas the third term C depends on the proton recoil and proton polarizability corrections. Currently,

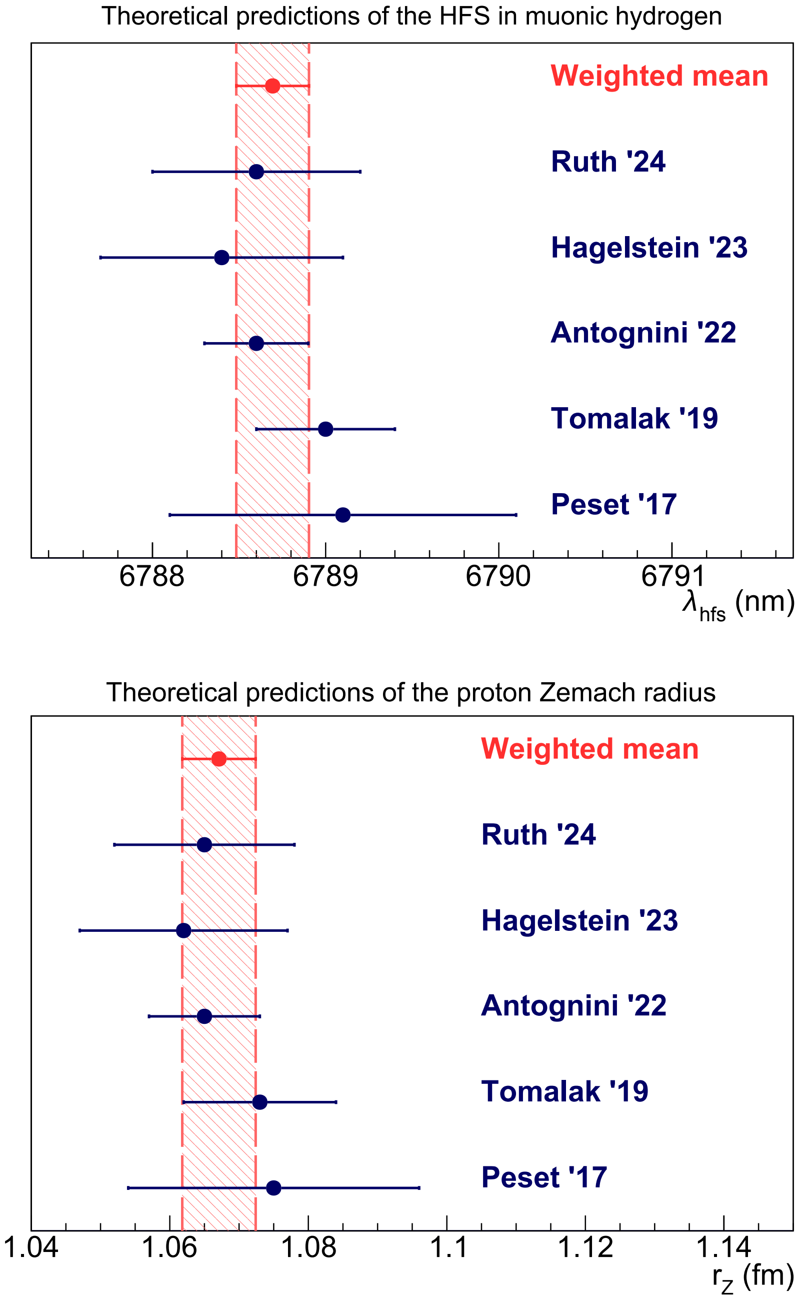

Figure 1.3: *Latest theoretical predictions for the μH 1S hyperfine splitting and the related proton Zemach radius[2, 27–30]. The weighted mean, indicated with a coloured area, has been used as a reference for the spectral range to measure.*

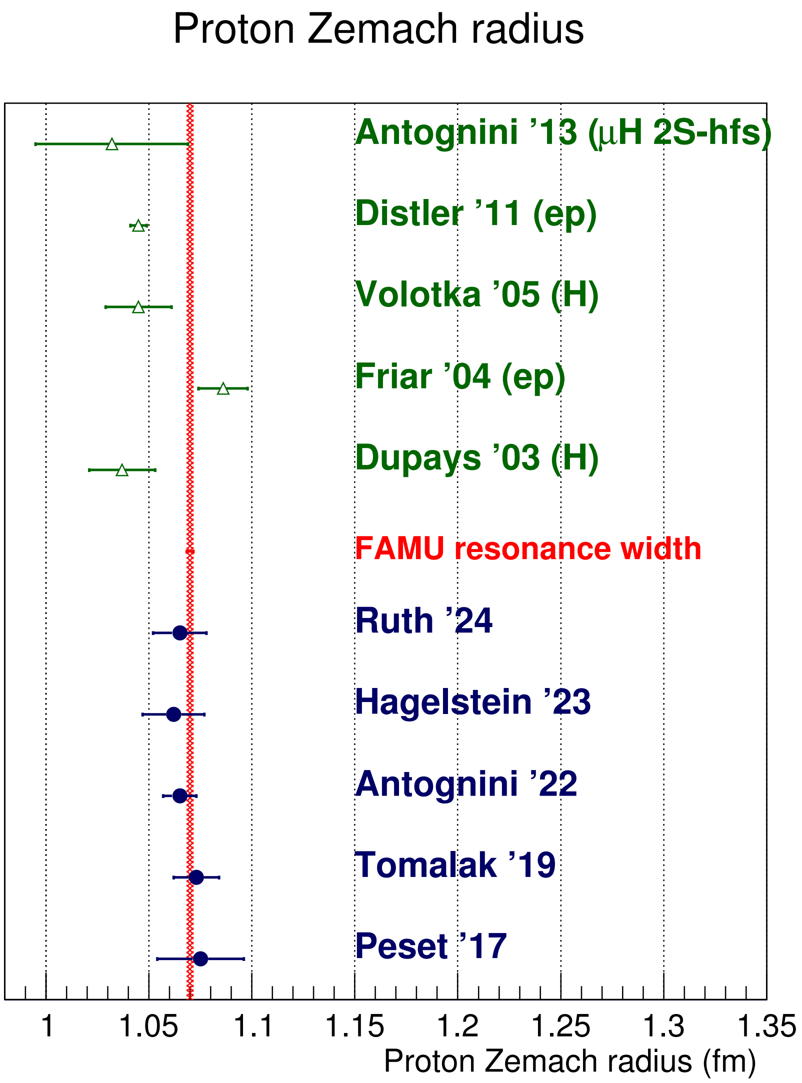

Figure 1.4: *Comparison between the latest theoretical predictions for the proton Zemach radius and the values extracted from experimental data obtained by H spectroscopy[31, 32], ep scattering[5, 33] and μH 2S-hfs[8]. A red band shows the expected resonance width to be observed by FAMU (width 0.003 fm, assuming a 1S-hfs resonance width of 80 pm); the expected uncertainty on r_Z is smaller than this interval width.*

the weighted mean of the 5 latest theoretical predictions[2, 27–30](2017-2024) for the *1S-hfs* is (6788.7 ± 0.2) nm, whereas the weighted mean of the corresponding values of proton Zemach radius is (1.067 ± 0.005) pm. All these predictions are presented in Figure 1.3.

Several measurements of the proton Zemach radius were made available in the past. Calculations were made based on the traditional hydrogen *1S-hfs*[31, 32], which has a wavelength of ~ 21 cm, well known in radioastronomy as the *hydrogen line*. In addition, calculations were made using estimations of $G_E(Q^2)$ and $G_M(Q^2)$ from *ep* scattering[5, 33]. Finally, the CREMA collaboration carried out a measurement of the μH 2S-hfs to derive the Zemach radius[8]. Figure 1.4 shows as summary of some of the experimental measurements, compared to the aforementioned theoretical predictions. In addition, an estimation of the FAMU resonance width is shown: assuming a calculated resonance full width at half maximum of 80 pm, the corresponding width of the r_Z measurement would be of 0.003 pm. This width is smaller than the current best experimental uncertainty for r_Z[33]. If this calculation is true, the uncertainty on the centroid of this resonance, i.e. the uncertainty on r_Z, would be even smaller, resulting in the most accurate measurement of the proton Zemach radius ever made, by at least one order of magnitude.

1.3 Muonic atom formation and behaviour

When a negative muon (μ^-) travels through matter and it interacts with the electromagnetic fields at atomic level, a muonic atom can be formed[34–37]. It is a bound state of nucleus and negative muons, in which the atomic levels are modified by the fact that the muon has mass $M_\mu \simeq 105.7$ MeV/c$^2 \simeq 207 M_e$, where M_e is the mass of the electron. In fact, considering for example the easiest model for atomic levels, the *Bohr model*, in which the energy levels only depend on the principal quantum number n, all energy levels are function of the Rydberg constant $R_\infty \propto M_r = (M_A + M_e)/(M_A M_e)$, where M_r is the reduced mass of the nucleus-electron system, and M_A is the mass of the nucleus. The reduced mass of the nucleus-muon system is 187 times bigger than the one of the nucleus-electron system. As a consequence, one can easily understand that in muonic atoms, the energy levels are modified by the presence of the muon in the atomic structure. Specifically, the modification factor is linear to the reduced mass and therefore the energy levels are the order of 187 times higher than those for ordinary hydrogen. For the same reason, the Bohr radius of each orbit is much smaller, by a factor 187.

When a μ^- is stopped by an atom of element X, the related muonic atom is noted as μX and it is generally produced in an excited state with $n \gtrsim 14$[40]. As a consequence, the production of a muonic atom is generally followed by the de-excitation of the atom. For higher values of n, the de-excitation happens mostly through the emission of Auger electrons; whereas starting from $n \sim 6$ the X-ray emission becomes dominant. This emission is generally referred to

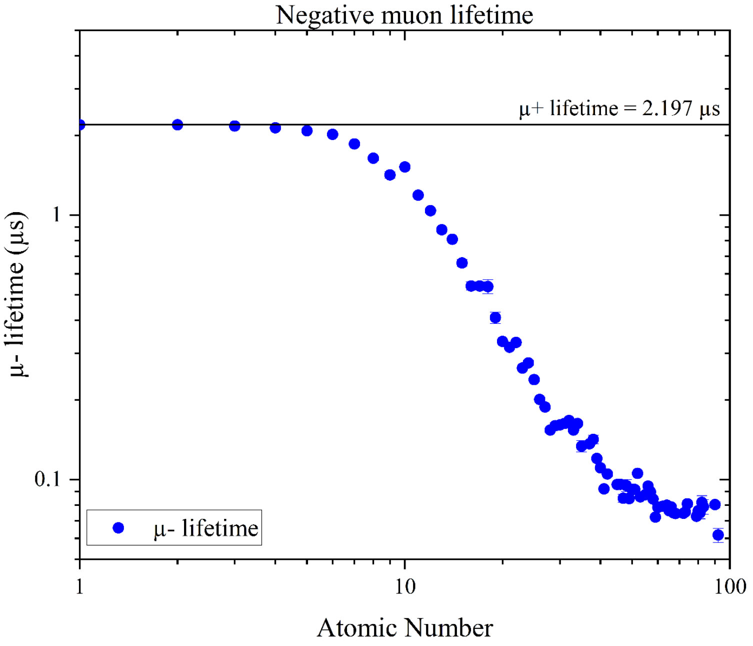

Figure 1.5: *Mean lifetime of negative muons in muonic atoms as a function of the atomic number Z. At higher Z, the lifetime is reduced due to increse in probability of muon capture by the nucleus[38].Taken from [37], data from [39].*

as the *prompt* emission as it happens in a time scale smaller than 1 ns after the muon capture. When the muon reaches the ^{1}S level, it can either be captured by the nucleus or remain in the atomic structure until its decay. The free muon decay time in the rest frame is about 2.2 μs, whereas for muons in atomic shells it can be lower, and specifically it will decrease as the atomic number Z increases due to enhanced nucleus capture probability[38]. The capture reaction is:

$$\mu^- \ p \to n \ \nu_\mu. \tag{1.13}$$

The mean lifetime of the muon in muonic atoms as a function of Z is reported in Figure 1.5. If nuclear capture takes place, the atom becomes an ordinary atom with $Z \to Z-1$ and delayed electronic X-rays from the atom with atomic number $Z-1$ may be observed. On the other hand, if the muon remains in the atomic shells and decays, the resulting atom will still have atomic number Z and therefore X-rays of the same atom may be emitted.

The muonic X-ray transition energies and probabilities can be found in specific experimental databases[40, 41] or can be computed by solving the radial Dirac equation[37, 42].

Chapter 2

The FAMU experiment

The FAMU experiment [23], on which this work is based on, is presented in this Chapter in terms of scientific goal, experimental technique and experimental setup. Some experimental setup performance assessments are also presented.

2.1 Aim and experimental technique

FAMU (*Fisica degli Atomi MUonici*, Muonic Atom Physics) is a nuclear physics experiment funded by the Italian National Institute for Nuclear Physics (INFN, *Istituto Nazionale di Fisica Nucleare*) and currently operating at RAL (Rutherford Appleton Laboratory), in the United Kingdom. The experiment aims at an indirect measurement of the proton Zemach radius by means of atomic spectroscopy measurements in muonic hydrogen (μH). As discussed in Section 1.2, the hydrogen ground state hyperfine splitting (*1S-hfs*) holds a strong dependence on the Zemach radius. FAMU aims at measuring the *1S-hfs* in μH with an accuracy around 10^{-5} in order to estimate the proton Zemach radius with an uncertainty better than 1%.

The general experimental method to carry out such a spectroscopy measurement can be simplified in three phases:

1. **muonic atom formation** carried out by stopping a low-momentum high-rate negative muon beam in a gaseous hydrogen target. For details on the target and the muon beam see Sections 2.3 and 2.4.1, respectively;

2. **excitation of *1S-hfs*** by injecting a Medium-InfraRed (MIR) laser in the target. For details on the laser see Section 2.4.2;

3. **search for an excess in the experiment observable**, which needs to be related to the occurrence of spin-flip due to the laser. The FAMU observable is discussed in the current section alongside with some possible alternatives.

Three different experiments were proposed and are currently being designed, prepared or operated in this framework, as already mentioned in Section 1.2.

FAMU, the one discussed in this work, is based on a pulsed muon beam at the RIKEN-RAL Port1 beamline at the ISIS Neutron and Muon Source, Rutherford Appleton Laboratory (RAL), UK. The beam is delivered in spills with a 40 Hz average repetition rate (see Section 2.3). Every other muon pulse, a laser pulse is injected in the gas target (see Section 2.4.2), which contains a small amount of gaseous oxygen (see Section 2.4.1). The observable in the FAMU experiment is an excess in the amount of delayed muonic Oxygen (μO) X-rays. In fact, as depicted in the scheme in Figure 2.1, the recoil energy held by μH which endured the transition is enough to enhance the probability of collision between oxygen and μH, and the resulting formation of a μO atom, which is delayed with respect to the muon beam injection and subordinated to the injection of the correct laser wavelength. Finding such wavelength is therefore the experimental FAMU goal, by repeating the measurement at different wavelengths and looking for a resonant excess in the number of delayed μO X-rays. The X-rays of interest are $K_\alpha \simeq 133$ keV, $K_\beta \simeq 158$ keV and $K_\gamma \simeq 167$ keV. The illustration of the hypothetic behaviour of this observable is shown in Figure 2.2, which has to be intended only as a qualitative visualisation of the effect (even though the data are taken from a toy Monte Carlo). The FAMU experimental method was first proposed, with transfer to gold foils instead of oxygen, in 1993[43]. The actual experiment started in 2014 with the design of laser, detector and target systems, and the gas mixture was optimised during experimental runs at RIKEN-RAL in 2016 – 2018, as further explained in Section 2.4.1. The experiment started data taking in 2023 with two physics runs in October (RAL202304) and December (RAL202305), two more physics runs in 2024 in July (RAL202404) and October (RAL202405) and it is expected to keep operating also in 2025.

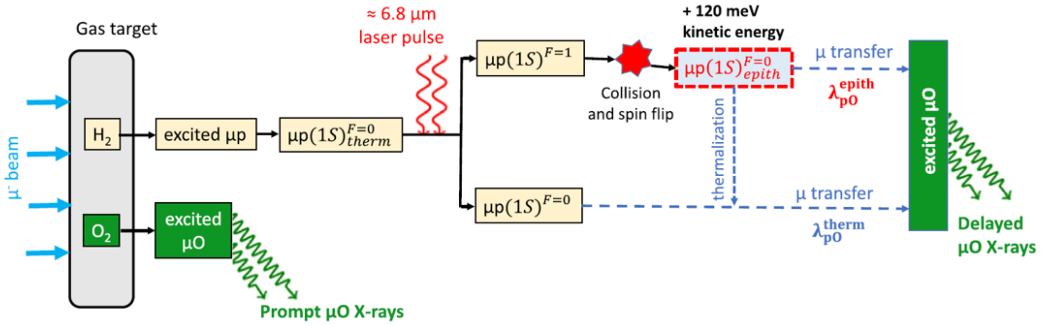

Figure 2.1: *Scheme of the FAMU experimental method[23]. The transition leaves the μH with an excess of 120 meV of kinetic energy, which enhances the probability of muon transfer to oxygen.*

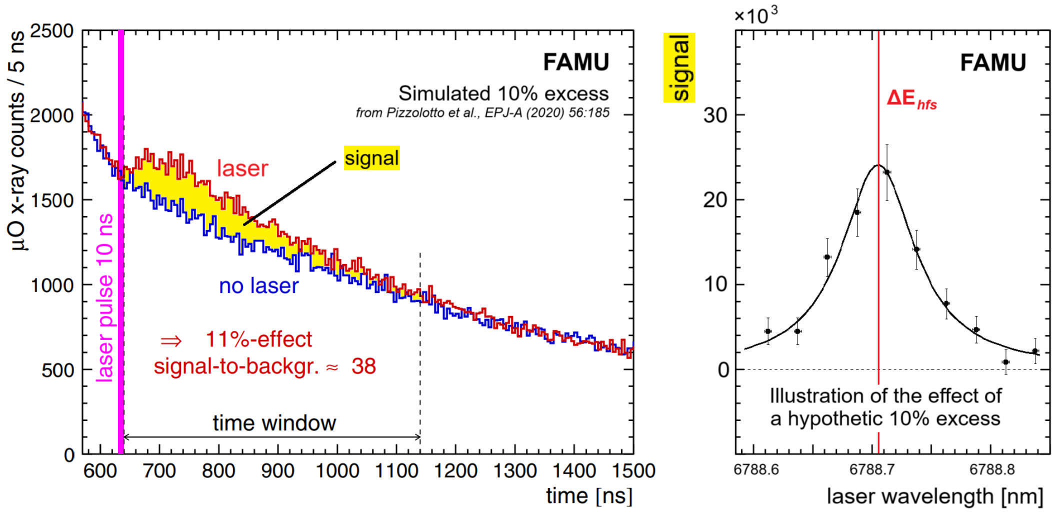

Figure 2.2: *Behaviour of the FAMU observable, the excess of delayed μO X-rays. Left: toy simulation of a hypotetic 10% effect on the FAMU observable (yellow coloured area) [23]. Right: illustration of a hypotetic resonance of the FAMU observable as a function of the laser wavelength, where the mean value is the resulting estimation of* ΔE_{hfs} *(the value chosen here as* ΔE_{hfs} *is the latest prediction[2], not a FAMU experimental result).*

2.2 FAMU previous experience (2014 – 2018)

The FAMU experiment started in 2014 and its activity in the first four years was mostly in the optimisation of the experimental setup for the actual physics data taking phase, which is now undergoing[44–46].

In particular, the choice of the target in terms of size, gas mixture, pressure, temperature needed some experimental campaigns to measure the thermal transfer rate of muons from hydrogen to other gases without any laser excitation.

Three candidate atoms were cosidered: oxygen, argon and carbon. The oxygen data have been analysed and published[45, 46], whereas the argon and carbon data are currently being prepared for publication. The final choice was to use oxygen cooled with liquid nitrogen (77 K) and at only 7 bar of pressure in order to minimise the collisional transfer.

The experimental setup for these runs[44] consisted in a cryostat for the gaseous target and the cooling medium (liquid nitrogen), a scintillating fibre hodoscope for beam shape monitoring and a set of X-ray detectors.

During this phase, FAMU carried out the first ever measurement of the muon transfer rate from μH to oxygen (Λ_{pO}) as a function of temperature, shown in Figure 2.3. This measurement is in accordance with a previous one, carried out at room temperature[47], but it is not in agreement with the theoretical predictions. Further studies were made on argon and carbon, but they have not been published yet. These results, along with massive works in simulating the setup and the processes, resulted in the final design for the FAMU setup, described in detail in Section 2.4.

In particular, oxygen has been chosen for its low thermal transfer rate at liquid nitrogen cryogenic temperatures (77 K). This would allow to improve the signal-to-noise ratio when measuring the FAMU observable, which is the number of muon transfers caused by the laser.

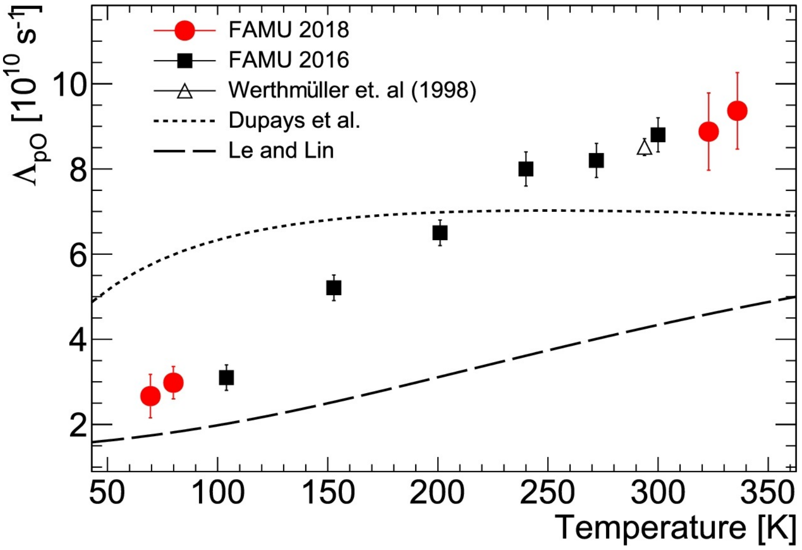

Figure 2.3: *Measurement of the transfer rate from μH to oxygen (Λ_{pO}) as a function of temperature from FAMU 2016[45] and 2018[46] data compared to theoretical models and a previous measurement at room temperature. Plot taken from [46].*

2.3 Muon beam production and delivery

The ISIS Neutron and Muon Source is currently the leading centre in Europe for the production of pulsed neutron and muon beams. The facility is located at the Harwell Campus in Didcot, Oxfordshire (United Kingdom), as part of the Rutherford Appleton Laboratory (RAL). Established in 1984, ISIS is currently managed by the Science and Technology Facilities Council (STFC) and it hosts the brightest pulsed muon facility in the world. The production and transport of muons to the FAMU setup is briefly discussed in this Section[48, 49].

The ISIS muon beam is produced by the collision of an 800 MeV proton beam with a target. The ion source produces H^- ions with an energy of 35 keV, which are then accelerated by a RadioFrequency Quadrupole (RFQ) to 665 keV[50]. At this point, the ions enter the linac (linear accelerator), composed of 4 accelerating tanks with a total length of about 50 m. The output of the linac is a 200 μs continuous stream of 70 MeV H^- ions, which is injected in the synchrotron[51].

The ISIS proton synchrotron[51, 52] has a radius of 26 m and it is located in the experimental hall previously occupied by the 7 GeV Nimrod proton synchrotron (1964 – 1978). The 70 MeV continuous H^- beam is injected in the synchrotron through the injection straight. This component contains a thin stripping foil (0.25 μm carbon) which removes the two electrons from H^- in order to get a proton beam. Once the injection is complete, the synchrotron contains a uniform ring of protons. The acceleration process divides the particle in two co-rotating opposite bunches. When the top energy of 800 MeV is reached, a proton travels at $0.84c$ and it travels a full turn around the synchrotron (circumference: 163 m) in approximately 640 ns. As a consequence, the centres of the two bunches are 320 ns apart. The proton beam extraction is carried out with a rate of 50 Hz, extracting particles from both proton bunches. For this reason, a proton spill is extracted every 20 ms, and it is composed of two proton bunches separated by 320 ns.

The proton beam is extracted and directed to two different neutron production areas: Target Station 1 (TS1) and Target Station 2 (TS2). Every five proton spills, four are sent to TS1 and one to TS2. As a consequence, the average repetition rate of protons against the muon production target is 40 Hz.

The muon production target[53] is positioned about 20 m before the TS1 on the same beampipe, therefore it is immersed in the proton beam directed to TS1, blocking approximately 5% of the protons to TS1. The most suitable way to produce a muon beam is through single- and double-pion production by hitting a low-Z target with a proton beam[54]. If the energy of the proton is $E_p > 280$ MeV, single-pion production can take place from the interaction of the proton beam with protons and neutrons in the target. These processes

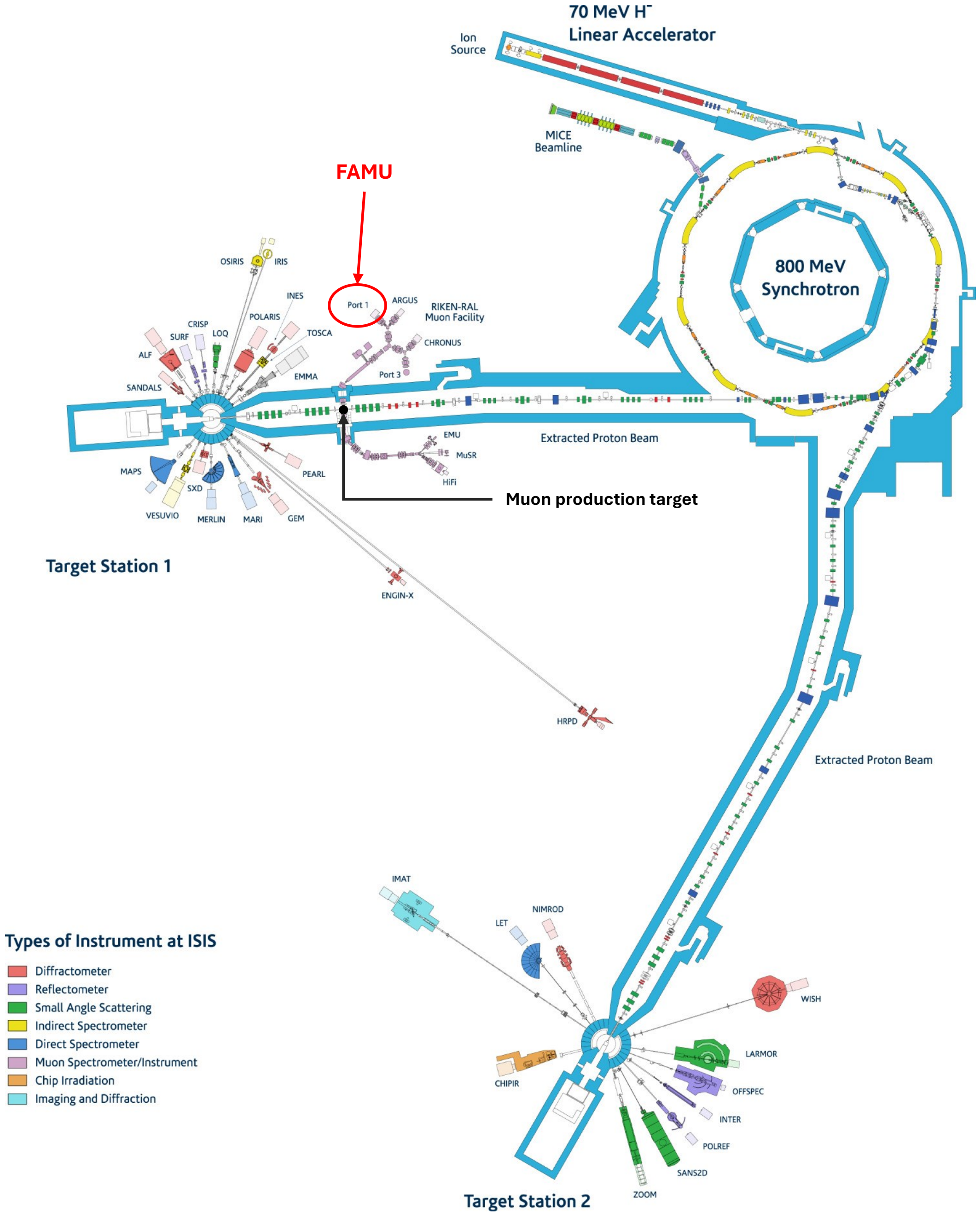

Figure 2.4: *Scheme of the ISIS Neutron and Muon Source with highlighted position of the muon production target and the FAMU experiment[51].*

peak between 500 MeV and 1 GeV:

$$\begin{aligned} p\,p &\rightarrow p\,n\,\pi^{+}, \\ p\,n &\rightarrow p\,p\,\pi^{-}. \end{aligned} \tag{2.1}$$

The threshold for double-pion production is instead $E_p > 600$ MeV, with peak production at 1.5 GeV:

$$\begin{aligned} p\,p &\rightarrow p\,p\,\pi^{+}\pi^{-}, \\ p\,n &\rightarrow p\,n\,\pi^{+}\pi^{-}. \end{aligned} \tag{2.2}$$

The pions produced in the muon production target will then decay with a time constant of $\sim$ 26 ns in muons and neutrinos:

$$\begin{aligned} \pi^{+} &\rightarrow \mu^{+}\,\nu_{\mu}, \\ \pi^{-} &\rightarrow \mu^{-}\,\bar{\nu}_{\mu}, \end{aligned} \tag{2.3}$$

giving rise to the desired muon beam. Let $c = 1$, for a decay at rest ($E_\pi = M_\pi$), the total final momentum will be zero (i.e. $p_\mu = p_\nu =: p$). Considering a massless neutrino ($E_\nu = p$), the conservation of energy $E_\pi = E_\mu + E_\nu$ gives the relationship $E_\mu = M_\pi - p$. Equalling this expression with the definition of total energy for the muon $E_\mu^2 = p_\mu^2 + M_\mu^2$ one can derive the momentum of the muon emitted at rest:

$$p_\mu\,(= p = p_\nu = E_\nu) \simeq 29.65 \text{ MeV}. \tag{2.4}$$

Depending on whether the pions decay at rest inside the target or escape it, two species of muons can be extracted:

- **surface muons** are μ^+ originated from the decay at rest of π^+ produced close to the surface of the graphite target. This production mode doesn't work for μ^- as they are captured by carbon atoms in the target, forming muonic carbon atoms (μC). The flux is generally high (over 10^6 muons/s), their momenum peaks at about 29 MeV/c, as they are produced at rest. At ISIS, surface muons are normally sent to the beamlines forming the European Commission (EC) muon facility (EMU, μSR and HiFi);

- **decay muons** are μ^+ or μ^- formed by transporting the pions out of the target, selecting their desired momentum, and letting them decay in order to produce a muon beam of a certain momentum. At ISIS, they are normally sent to the RIKEN-RAL muon facility, with a momentum-dependent flux. RIKEN-RAL is theoretically capable of delivering muons between 17 and 120 MeV/c, limited to 90 MeV/c for technical reasons. In particular, the beam delivered to FAMU is a 55 MeV/c decay μ^- beam.

Regarding the pion decay in motion, as the muon production is a two-body collision (Equation 2.3), the daughter particles are always emitted back-to-back. The muon momentum at rest will be 29.65 MeV (as in Equation 2.4)The first limit case is when the muon is emitted in the same direction as the pion in the pion rest frame, namely it is a *forward muon*. In this case, the final muon will always move in forward direction with respect to the decayed pion, with a higher momentum, as the momentum in the laboratory frame will be $p'_\mu = \gamma_\pi\left(+p_\mu + \beta_\pi E_\mu\right)$. In the opposite case, the *backward muon* is emitted, in the pion rest frame, in the opposite direction, but in the laboratory frame $p'_\mu = \gamma_\pi\left(-p_\mu + \beta_\pi E_\mu\right)$. Hence, if

$$\beta_\pi > \frac{p_\mu\,[29.6\ \mathrm{MeV/c}]}{\sqrt{p_\mu^2 + M_\mu^2}} \Leftrightarrow p'_\pi > \frac{M_\pi}{M_\mu} p_\mu \simeq 39.1\ \mathrm{MeV/c}, \tag{2.5}$$

the muon is still emitted in the same direction of motion as the pion, but with a lower momentum.

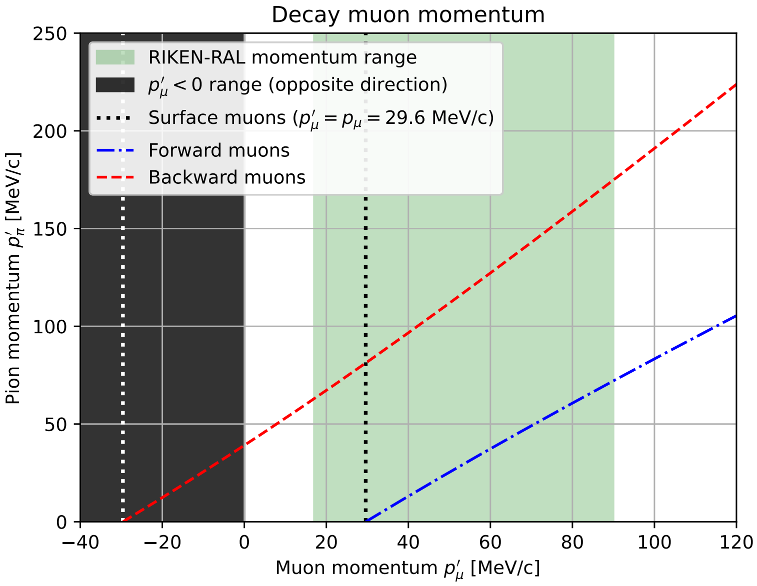

Figure 2.5: *Relationship between the initial pion momentum and the momentum of the forward and backward decay muon, calculated by boosting p_μ with p'_π as explained in Section 2.3.*

Figure 2.5 shows how the pion beam and decay muon momenta are related, for the two limit cases of forward and backward muons, in the range of the RIKEN-RAL facility. Values of the muon momentum below 29.6 MeV/c can therefore be obtained by backward emission with pion momentum between ~ 39 and ~ 78 MeV/c, whereas both forward and backward emission can cover the region of muon momentum over 29.6 MeV/c. For pions with momentum below ~ 39 MeV, the backward muons are emitted in backward direction also in the laboratory frame, and they are lost.

The RIKEN-RAL facility at the ISIS Neutron and Muon Source is designed to extract pions from the ISIS muon production target and produce a beam of selected muon momentum (either μ^+ or, as in this case, μ^-).

The ISIS muon production target consists of a 10 mm-thick graphite layer, set at 45° with respect to the proton beam. It is immersed in the proton beam directed to TS1 and it capures about 5% of the incoming protons. The 45° inclination allows the side of the target facing the incoming proton beam to be also facing the EC muon facility. In this way, the surface muon delivery to EMU, μSR and HiFi is optimised.

Figure 2.6 shows the path followed by particles in the RIKEN-RAL facility before reaching Port1, where the FAMU setup is located. The particle path through the facility can be divided in three major sections: the *pion injection system* transports the pions of the desired charge and momentum, the *superconducting solenoid*, where most of the $\pi \to \mu\ \nu_\mu$ decays take place, and the *muon extraction system*, responsible for the muon beam optimisation and transport to the four irradiation ports.

The first section of the beampipe, also referred to as *pion injection system*, transports pions to the superconducting solenoid. It is composed of two quadrupole magnets (RQ1, RQ2) and a bending magnet(RB1), which are set in order to focus and inject the pions in the solenoid with the required momentum and remove uncharged particles. A hollow of the pion injection system holds three Cherenkov chambers used to trigger the experiments, including FAMU, carried out at the facility.

The *superconducting solenoid* is the part of the beampipe designed to host most of the pion decays. It is 5.5 m long and produces a strong magnetic field (up to 5.5 T), acting as a decay channel for pions. The length of the solenoid corresponds to the mean decay length of 100 MeV/c pions:

$$\lambda_\pi = v\gamma\tau_\pi = \frac{c \cdot \tau_\pi\,[2.6 \cdot 10^{-}8\ \mathrm{s}]}{m_\pi\,\left[139.6\ \mathrm{MeV/c^2}\right]}\ p_\pi\,[\mathrm{MeV/c}] \simeq 0.055\ \frac{p_\pi}{\mathrm{MeV/c}}\,[\mathrm{m}]\,. \tag{2.6}$$

The current of the solenoid is optimised for the required muon beam momentum, up to 730 A. The magnetic field generated by the solenoid forces the emitted decay muons to propagate in the same direction as the initial pion beam. In fact, the pion decay at rest is isotropic. Even though it is not isotropic in the laboratory frame, as already discussed, most muons are not emitted in a direction parallel to the beampipe, and they would therefore be lost on the walls.

After the decay solenoid, the beam is mostly composed of muons and enters the third part of the beamline, called the *muon delivery system*, which carries the required muon beam to the four irradiation ports. The muon delivery system to each port is made of three straight beampipes, each one with three quadrupole magnets for beam focusing and shaping, connected by two bending magnets in order to select the particle momentum. The series of quadrupole (RQ) - dipole (RB) for FAMU (Port1) is: RQ3-4-5, RB2, RQ6-7-8, RB3, RQ9-10-11, positioned as depicted in Figure 2.6. The bending magnet RB2 is featured with a kicker, a device with variable magnetic field which allows to direct the two beam bunches in different beamlines (one to Port1 or Port2, the other to Port3 or Port4). This device is not in use for the FAMU experiment, *i.e.* both bunches in each muon spill are directed to FAMU at Port1, to maximise the μH production.

Figure 2.7 shows an estimation of the maximum flux which can be reached at the RIKEN-RAL muon facility as a function of the muon momentum[48, 49].

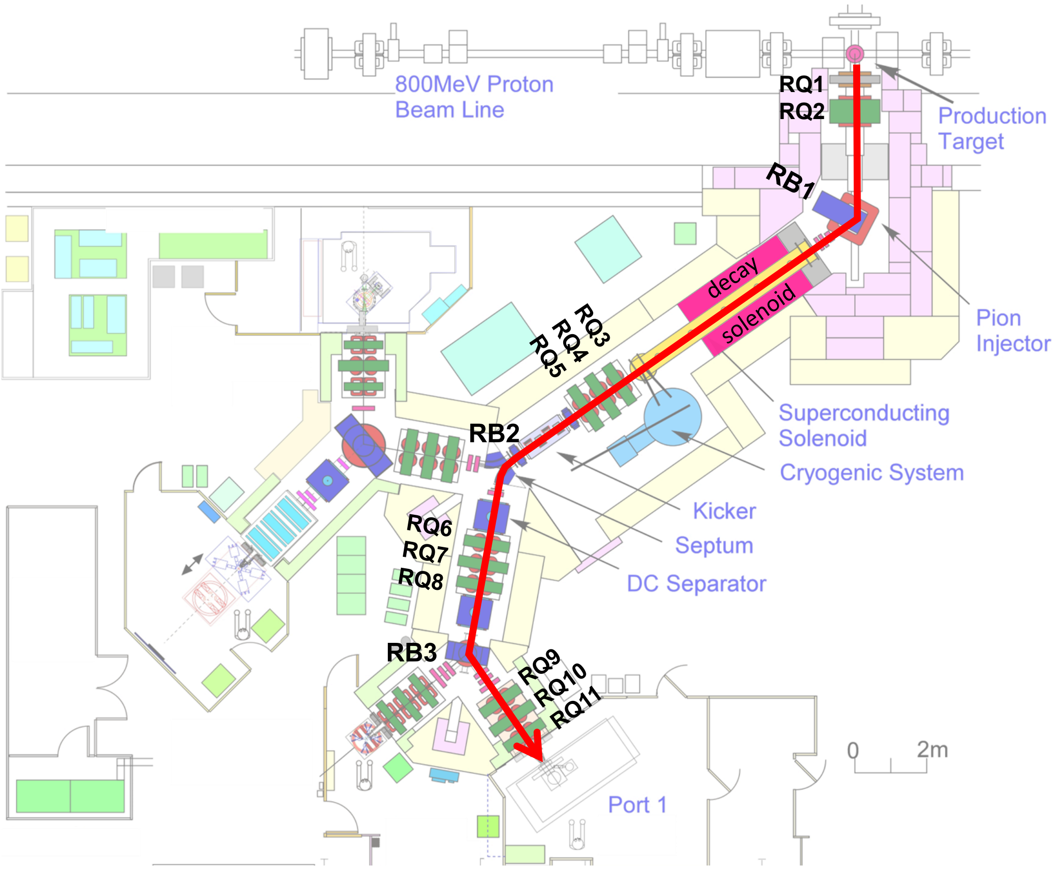

Figure 2.6: *Scheme of the path followed by muons directed to the FAMU target in the RIKEN-RAL muon facility. The positions of the bending (RB) and quadrupole (RQ) magnets involved in the beam delivery to FAMU are labelled[48, 55].*

The muon beam commissioning for the FAMU experiment took place in July 2023 and consisted in tuning the current of the last four magnets (RB3, RQ9, RQ10, RQ11 - see Figure 2.6 for reference) to optimise the beam shape and the number of muons directed in the gas target. In particular, RB3 is varied in order to centre the beam to the last section of the beampipe, whereas the values of current for the last three quadrupoles are varied from the initial values using the following linear combinations calculated for this specific

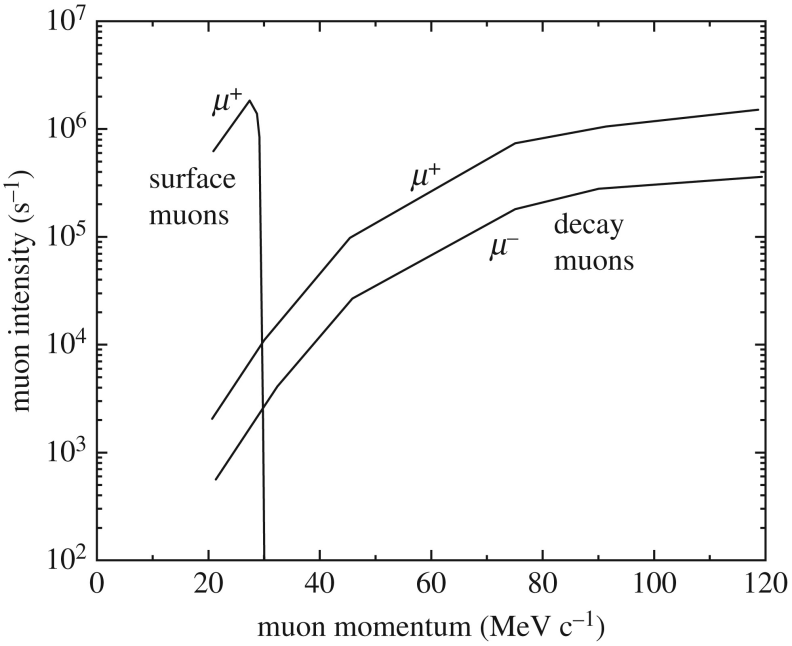

Figure 2.7: *Simulated muon flux as a function of momentum at the RIKEN-RAL facility ports[48, 49].*

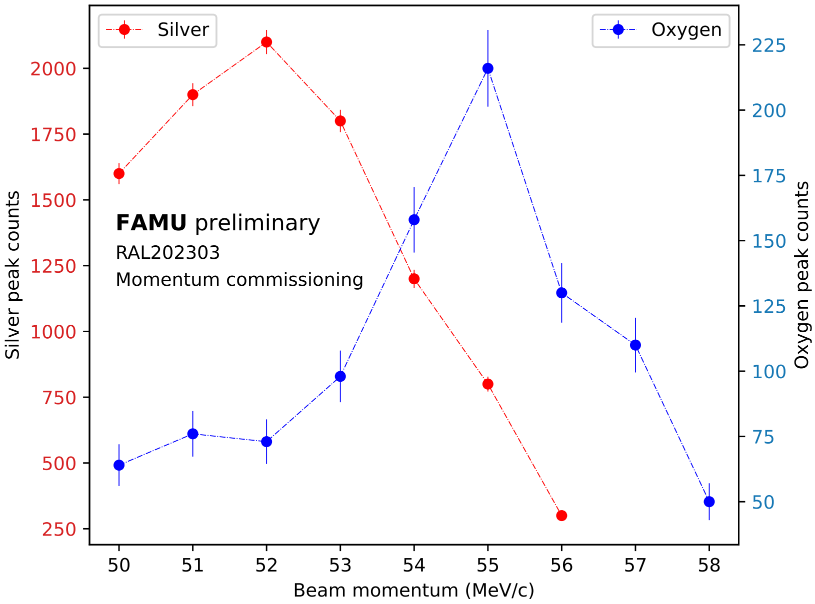

Figure 2.8: *Variation of the number of prompt μAg and delayed μO X-rays as a function of beam momentum (different scales). By selecting $p'_{\mu} = 55$ MeV/c, the number of muons stopped in the gas is maximised.*

beamline:

$$\begin{pmatrix} I_{RQ9} \\ I_{RQ10} \\ I_{RQ11} \end{pmatrix} = \begin{pmatrix} I^0_{RQ9} \\ I^0_{RQ10} \\ I^0_{RQ11} \end{pmatrix} + \begin{pmatrix} -0.13 & +0.28 & -1.00 \\ +0.13 & +1.00 & -0.20 \\ +1.00 & +0.22 & +0.45 \end{pmatrix} \begin{pmatrix} \texttt{tuneX} \\ \texttt{tuneY} \\ \texttt{tuneM} \end{pmatrix} \tag{2.7}$$

where the parameters `tuneX`, `tuneY` and `tuneM` are designed to squeeze the beam spot on the X direction, on the Y direction and vary the beam spot X/Y ratio, respectively. These three parameters were varied in order to minimise the beam size and maximise the amount of prompt muonic silver X-rays (141 keV) produced by the target entrance window. This guarantees the optimal focus of the beam on the target.

After this, the beam momentum was changed in order to maximise the amount of muons stopped in the gas target. This was done by evaluating the number of prompt muonic silver X-rays (141 keV) and the number of delayed muonic oxygen X-rays (133 keV). In fact, as explained in Section 2.4.1, the target entrance window is featured with a silver layer to enhance the muon energy loss prior to the gas target. The optimal beam momentum is the one which maximises the muon stopping in gas. Each measurement was carried out with full beam current and collecting 120k events (2400 s of acquisition time). The final momentum value, used for all FAMU experimental measurements, is $p'_\mu = 55$ MeV/c.

In September 2024, the power supply of RB2 was changed, and a new tuning of its current has been carried out, using directly the FAMU hodoscope. The tuning plot is shown in Figure 2.9, and the current corresponding to the maximum hodoscope deposited charge (Q_{tot}, proportional to the muon flux, see Chapter 3 for details) was kept.

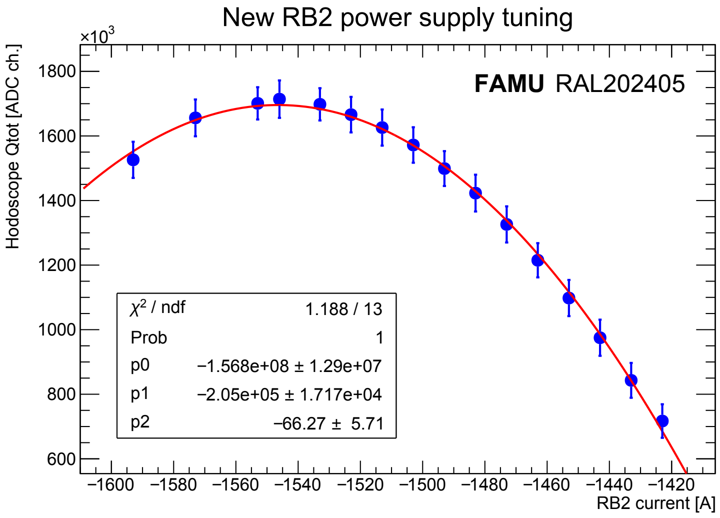

Figure 2.9: *Tuning of the new power supply for the RB2 magnet, carried out in September 2024. The points have been fitted with a 2^{nd}-degree polynomial.*

2.4 Experimental setup

In this section, the full setup of the FAMU experiment is described in detail, specifically regarding the X-ray detectors. The beam monitor is described extensively in Chapter 3. A picture of the full setup, taken after the June 2023 beam commissioning, is shown in Figure 2.10.

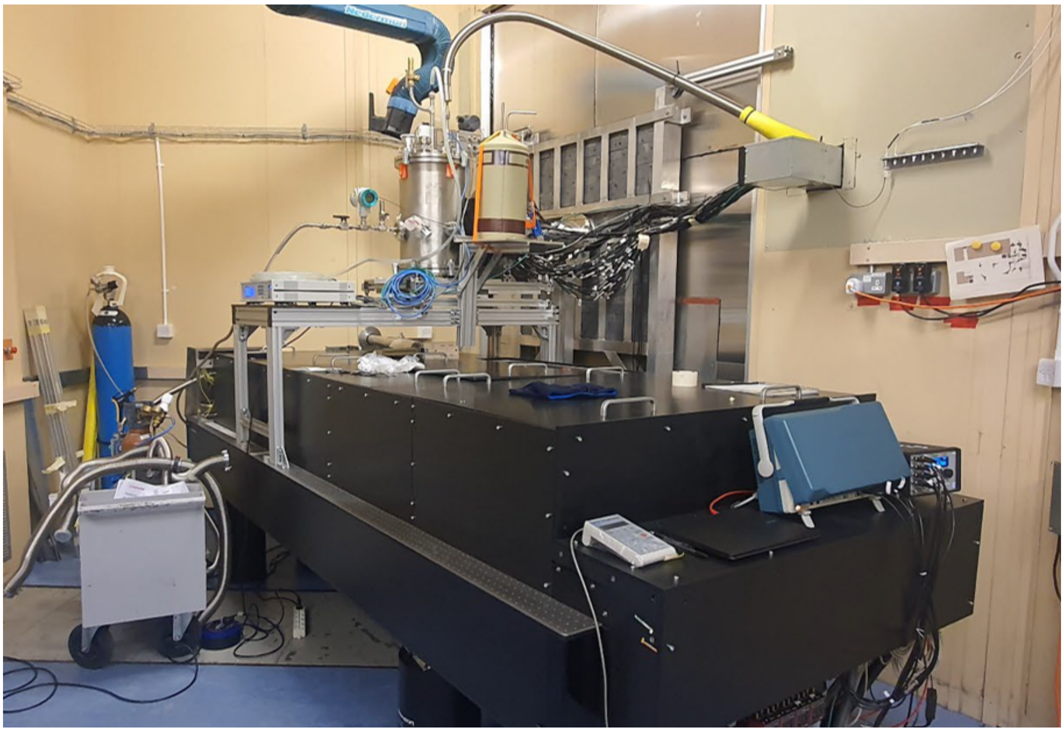

Figure 2.10: *Picture of the fully mounted FAMU experiment at RIKEN-RAL, taken in September 2023 after the commissioning but before the first data taking. The cryostat is clearly visible on top of the laser optical table (black) and surrounded by the X-ray detectors.*

2.4.1 Target and optical cavity

Following what one can see in Figure 2.3, in order to minimise the kinetic transfer of the muon to oxygen (acting as a background contribution), the experiment would ideally work at the lowest possible temperature for the hydrogen-oxygen mixture. However, the condensation temperature for O_2 limits the temperature to be above $\sim$ 60 K. For this reason, it has been decided to use liquid nitrogen (77 K) as the target cooling medium.

The target cryostat had to be designed with care to match all the FAMU requirements[23]. In particular:

- thin high-Z muon beam entrance window, in order to maximise the momentum loss in the entrance window and therefore the muon capture in the gas;

- low-Z materials in other directions to let 100 – 200 keV X-rays out of the target, where detectors are placed;
- an optical window is needed to inject the laser beam, and it must fit an optical cavity to maximise the gas-laser interaction.

Eventually, the current target has been simulated, optimised, designed and mounted in collaboration with CRIOTEC Impianti Srl to match the requirements. Figure 2.11 shows the position of the target in the FAMU final setup. A lateral section of the FAMU target cryostat is shown in Figure 2.12. In particular, the chamber containing the gas is shown in green and it is cooled by thermal contact with a tank containing 5 litres of liquid nitrogen at 77 K. This solution allows a vibrationless cooling process, which is crucial to avoid laser misalignments during the experimental runs.

In order to monitor the gas condition, the target chamber is featured with a pressure sensor (sensitivity 0.01 mbar) and two temperature sensors (sensitivity 1 mK). These sensors played an important role in assessing the tightness of the chamber and correct for small gas leakage, as shown in Section 4.3.2.

The muon beam exits the beampipe, crosses the FAMU beam monitor (see Chapter 3) and then passes through a beam collimator. It is composed of lead bricks, with a vertically-oriented slit of 5×1 cm^2 and 5 cm depth. It is aimed at injecting the muon beam only in the central area of the target and the optical cavity. Muons enter the cryostat through a 0.2 mm aluminated mylar window, then cross the 1 mm-thick aluminium wall of the gaseous target chamber, and lastly encounter a 0.6 mm layer of silver. The role of this Ag layer is to maximise the number of muons stopping in the gas by slowing them down just before entering the volume illuminated by the laser.

In this volume, an optical cavity[57] with silica mirrors and steel structure is placed. The cavity is aimed at enhancing the probability of interaction between μH atoms and the laser beam. It is studied to let the laser beam bounce back and forth minimising its power loss, in order to increase the interaction path between the gas hit by muons and the laser beam. The cavity mirrors, with cylindrical ends, are coated with ZnS/Ge multilayers to provide the best possible reflectivity (99.890(2)% at 6.78 μm).

According to a ray tracing simulation carried out in MATLAB, the light fills up all the cavity volume and about 10^3 reflections take place. The total lifetime of the laser beam in the gas is 304 ns, and the interaction path between laser light and μH atoms is 91 m. The simulation code is structured in two logical parts. The first one is the ray tracing, which takes into account the shape of the mirrors (flat with cylindrical sides), their distance, the beam injection point, and the beam injection angle. This part has been crucial in designing the cavity shape and injection angle in order to maximise the number of reflections confined in the cavity. The second part of the simulation takes into account of the beam loss due to the reflectivity of the spectra: for every round trip, the fraction of beam loss is quantified by $\alpha = 1 - \sqrt{R_1 R_2}$, where $R_{1,2}$ are

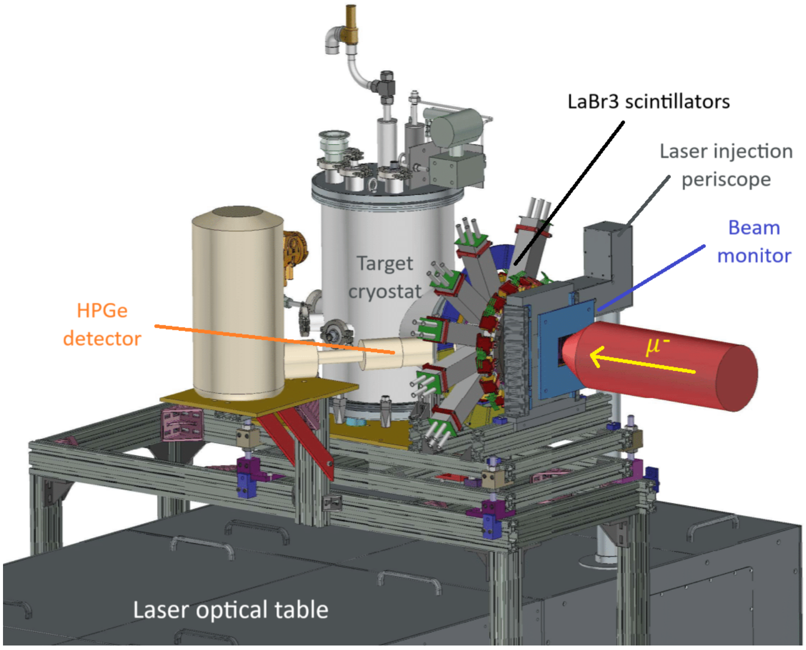

Figure 2.11: *CAD drawing of the 2023 FAMU setup. The target is positioned over the laser optical table, from which the laser is injected into the target through a periscope. The muon beam enters the target after passing through the beam hodoscope (muon beam monitor) and a lead collimator. All 35 X-ray detectors (34 LaBr*$_3$ *scintillators and 1 HPGe detector) are positioned around the gas target[56].*

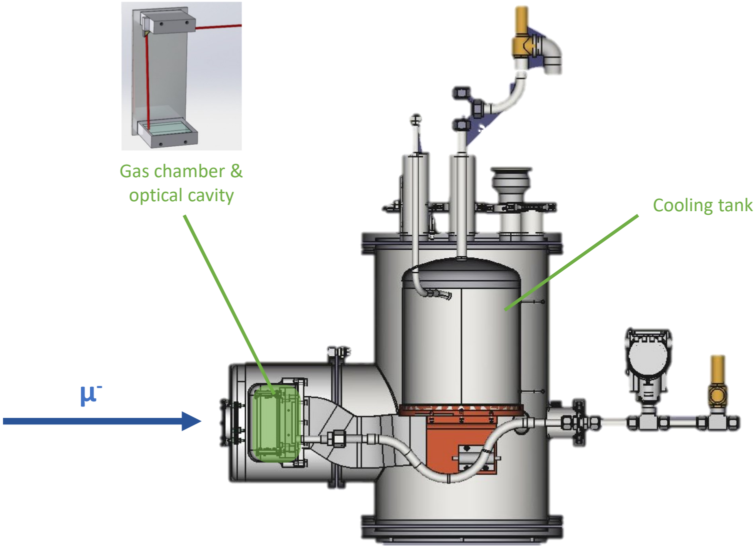

Figure 2.12: *Side section view of the target cryostat (CAD drawing), where the target chamber, the liquid nitrogen tank and the muon beam direction are clearly marked. The three detector-holding rings are attached to the target cryostat around the target chamber (green volume)[56].*

the values of reflectivity of the two mirrors. The geometrical parameters and the reflectivity values are based on the measurements carried out and certified by the manufacturer on the cavity itself before despatch. All uncertainties on geometric distances (including the curvature radius of cylindrical mirror sides) are around 0.2%, whereas the reflectivity values are $R_{1,2} = 99.890(2)\%$. All these values have negligible effects on the estimation of the number of reflections and the mean path of a photon in the optical cavity.

2.4.2 Laser beam production and delivery

The FAMU laser system, extensively described in [58], is a custom-made Mid InfraRed (MIR)laser system. The requirements for the laser were wavelength around 6789 ± 3 nm, energy over 1 mJ, linewidth below 0.07 nm, tunability step below 0.03 nm, pulse duration below 10 ns and 25 Hz repetition rate. The rate is half of the synchrotron rate in order to inject the laser every other beam spill, and use the spills with no laser as a background measurement. All these requirements were accomplished and overtaken, as resumed in Table 2.1. As of 2024, the FAMU laser system is the most powerful pulsed 6.8 μm tunable narrow-linewidth laser in the world, at the best of our knowledge.

The setup consists of two lasers: a fixed 1064 nm Nd:YAG oscillator, and a tunable (1262 ± 5) nm Cr:forsterite oscillator. The latter is featured with a diffraction grating, and the two cavity mirrors are placed on piezoelectric motors in order to allow the adjustment of the wavelength. The two beams are then properly coupled and injected in a non-linear Difference Frequency Generator (DFG), in this case a crystal of barium-gallium selenide ($BaGa_4Se_7$). The output of the crystal is a laser beam with frequency given by the relation $\lambda^{-1}_{\mathrm{DFG}} = \lambda^{-1}_{\mathrm{Nd:YAG}} - \lambda^{-1}_{\mathrm{Cr:forst}}$, which is in the required wavelength range. By tuning the wavelength of the Cr:forsterite laser it is therefore possible to tune the wavelength to be injected in the FAMU target optical cavity for the experiment. A schematic layout of the FAMU laser system is shown in Figure 2.13.

Table 2.1: *Comparison between requirements and results of the FAMU laser[58].*

Parameter	**FAMU requirement**	**Current FAMU result**
Wavelength	6786–6792 nm	6730–7135 nm
Energy output	> 1 mJ	1.2 mJ
Line-width	< 0.07 nm	0.009 nm
Tunability step	< 10 nm	7 nm
Pulse duration	< 10 ns	7 ns
Repetition rate	25 Hz	25 Hz

The laser was designed and perfectioned by INFN Trieste in collaboration with Elettra Sincrotrone in Trieste (Italy) and then installed and characterised extensively at RAL. For example, Figure 2.14 shows the comparison between the expected and measured water absorption lines in the range of wavelength of the system. From fitting the points and comparing them to the tabulated values, the laser has an absolute accuracy better than 100 pm on the wavelength.

Further metrology studies on narrow absorption lines of ethylene are undergoing, as they would enable a much more accurate calibration of the wavelength meter, hence a better wavelength absolute accuracy.

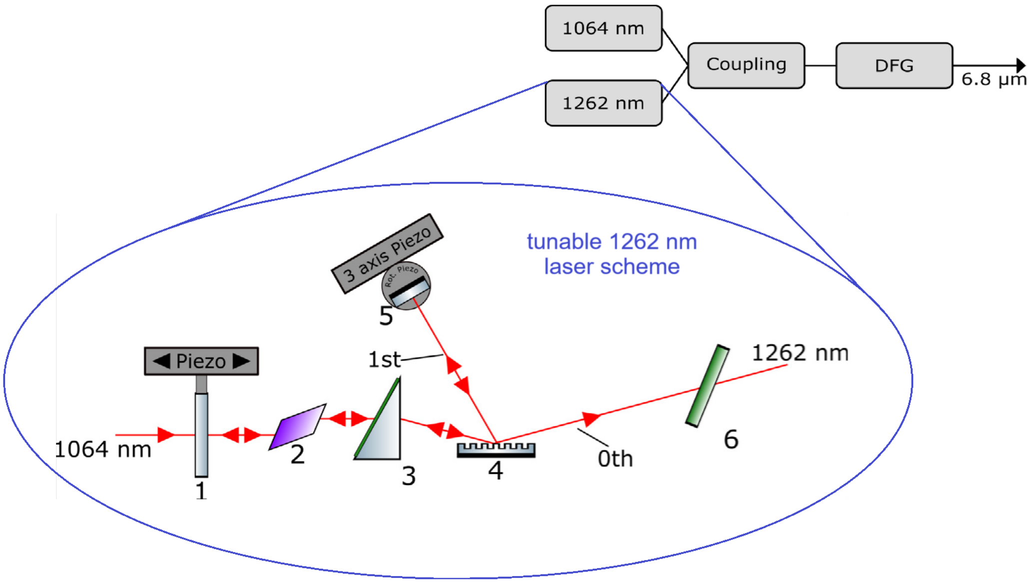

Figure 2.13: *Simplified sketch of the FAMU laser system and detail of the tunable 1262 nm laser (1 input mirror, 2 Cr:forsterite crystal oscillator, 3 beam-expanding prism, 4 diffraction grating, 5 back mirror, 6 output window), used to tune the final wavelength. Adapted from [58].*

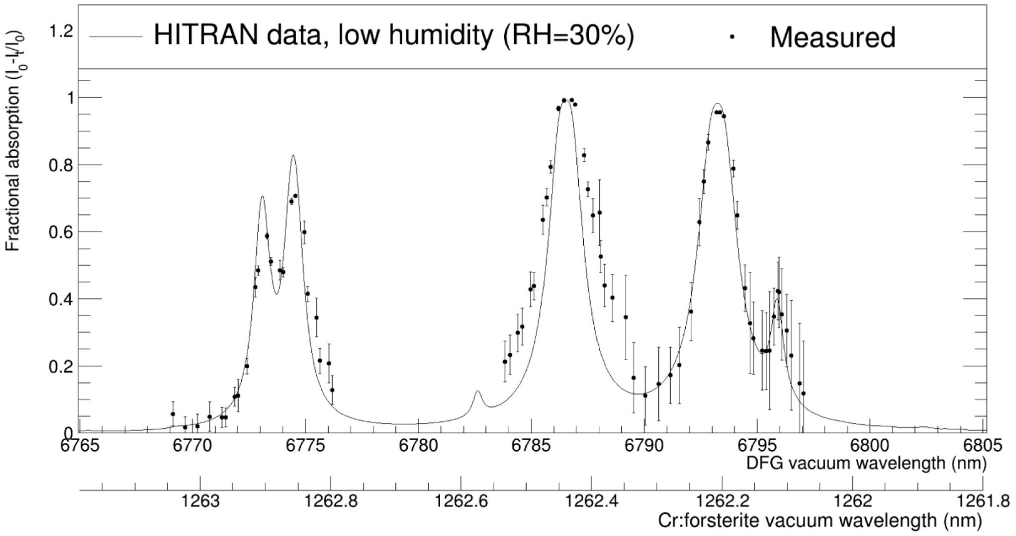

Figure 2.14: *air humidity absorption spectrum in the 6769–6798 nm collected with the FAMU laser system in 100 cm compared to the tabulated value (firm line). This study enabled to estimate a wavelength accuracy better than 100 pm for the system[58].*

2.4.3 X-ray detector setup and performance

This section has also been published on two papers about the 2023 FAMU detectors setup [56] and the upgrades carried out in the first half of 2024 [59].

The FAMU experimental technique requires a good compromise among time resolution performance, efficiency and energy resolution at 100 – 200 keV. As a consequence, it was decided to focus on inorganic scintillating crystals, specifically lanthanum bromide scintillating crystals doped with cerium, $LaBr_3$(Ce). The optimisation of timing performances first led to read out the scintillation light using PhotoMultiplier Tubes (PMTs). To increase the solid angle coverage with detectors with a small-size readout system, solutions with Silicon PhotoMultipliers (SiPM) were also studied and implemented, with much effort being made to make the timing performance comparable with the one of the PMT-read detectors. In addition, the presence of a detector with good energy resolution, even with worse timing performance, is important to always get a check on the X-ray lines present in the spectra and to cross-check the spectra of the scintillators. On this purpose, a coaxial High-Purity Germanium (HPGe) detector has been installed. A sketch of the 2023 FAMU experimental setup is shown in Figure 2.11, where the laser, target and detectors positions are marked. The position of the three detector-holding rings is visible in Figure 2.15. The detector system also includes a muon beam monitor, which plays a crucial role in allowing data normalisation based on the muon flux impinging the gas target in each beam spill. In fact, the muon flux is proportional to the number of muonic atoms and hence the number of target atoms for the transition. The activity of the muon beam monitor, also called beam hodoscope, is the main focus of this work and it is discussed in detail in Chapters 3 and 4.

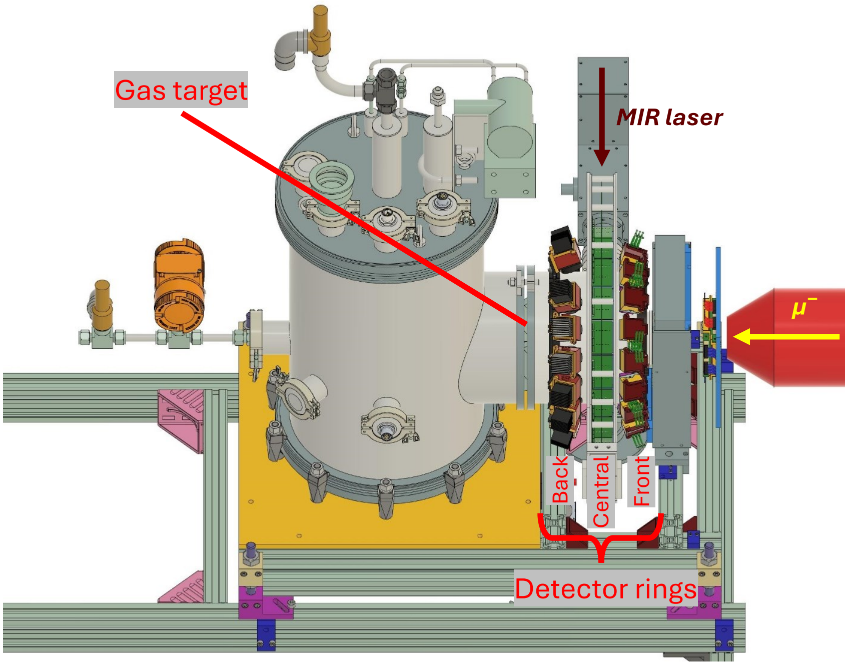

Figure 2.15: *Position of the three detector rings in the FAMU setup. The HPGe detector is not shown for visualisation purposes[59].*

Scintillating detectors

The FAMU experiment is featured with three different kinds of scintillating detector, placed around the target chamber by three circular holders, in order to exploit the different features of these crystals. The details on the setup are shown in Figure 2.16. All these detectors are based on lanthanum bromide doped with cerium scintillating crystals, $LaBr_3(Ce)$.

The first kind of detector featured in the experiment consists in a set of cylindrical crystals, having 1″ diameter and 1″ thickness, read out by Hamamatsu R11260-200 PMTs, which have a very short rise time (~ 12 ns). Details on these detectors are to be found in [60]. Six detectors of this kind are mounted on the central detector holder, shown in Figure 2.16 as long gray boxes marked with “LaBr”.

1″ and 1/2″ detectors with SiPM readout have also been developed[61–63]. Crystals for these detectors have two different geometries: cylinders with 1″ diameter and 0.5″ thickness (called 1″ crystals for simplicity), and cubes with 0.5″ side (1/2″ crystals, for the time being). They use Hamamatsu S14161-3050-AS and S14161-6050-AS SiPM arrays at nominal voltages. While 1/2″ detectors have a standard parallel ganging, 1″ detectors use a custom 4-1 PCB developed with Nuclear Instruments Srl[63]. The reason is that the increase in detector area, and therefore in SiPM array area, caused an increase in capacitance. This prompts both a worsening of the parallel noise and an increase in the signal duration. This is particularly important as most X-rays are generated in the prompt X-ray time region (few ns as the muon stopping), which makes most delayed X-rays preceeded by prompt ones. As a consequence, pile-up should be avoided and short signals are preferred. For the same reasons, initial attempts using passive circuits (e.g. pole zero circuits or hybrid ganging) had to be avoided as they introduced undershoot or further baseline oscillations, which would worsen the quality of delayed X-ray signals.

The performances, measured in laboratory, of the 1/2″ and 1″ detectors are summarised in Table 2.2. The 2023 setup consisted of 34 $LaBr_3$(Ce) scintillators:

- 6 cylindrical 1″-diameter 1″-thick read by PMTs[60];
- 16 cylindrical 1″-diameter ½″-thick read by SiPM arrays[62, 63];
- 12 cubic ½″-sided read by SiPMs[61].

As the latest upgrade on the PCBs for the read-out of 1″ detectors with SiPMs[63] enabled great improvements in time performances, it has been decided to substitute the ½″-SiPM detectors with 1″-SiPM detectors. The 2024 $LaBr_3$(Ce) detector configuration has been installed at RIKEN-RAL Port1 during the first half 2024 FAMU shutdown phase. It is composed of 34 $LaBr_3$(Ce) scintillator as follows:

- 6 cylindrical 1″-diameter 1″-thick read by PMTs;
- 28 cylindrical 1″-diameter ½″-thick read by SiPM arrays.

Each of the new detectors has around 3 times the frontal area (hence the geometrical acceptance) than an old ½″ detector. As a consequence, the total area of $LaBr_3$(Ce) detectors facing the target, and thus the acceptance, is increased by $\sim 32\%$ when passing from the 2023 to the 2024 setup. Regarding the set of scintillators installed in FAMU, detectors read by PMTs have better time performance, whereas those read by SiPMs have better energy resolution.

Table 2.2: *Time and energy performance of SiPM-based detectors determined during laboratory tests with radioactive sources, focusing on the 662 keV peak from ^{137}Cs and the 122 keV peak from ^{57}Co. Energy resolutions are calculated from the FWHM of photopeaks[61, 63].*

	rise time (ns)	fall time (ns)	Res. (%) @ ^{137}Cs	Res. (%) @ ^{57}Co
1″	29.3 ± 1.5	147 ± 13	3.01 ± 0.16	7.9 ± 0.4
1/2″	43 ± 5	372 ± 17	3.27 ± 0.11	8.4 ± 0.6

Both detector configurations are shown in Figure 2.16, where crystals read by SiPMs are marked with “MIB” (as they were developed by INFN Milano-Bicocca, in collaboration with INFN Pavia) and the ½″ detectors are marked with blue and italic text.

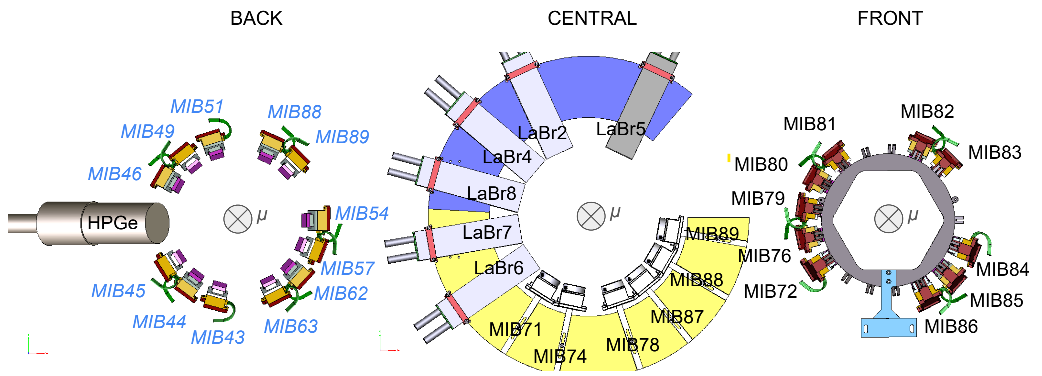

2023 detector setup (*RAL202303*, *RAL202304*, *RAL202305*):

[July'23 commissioning] *[Oct.'23]* *[Dec.'23]*

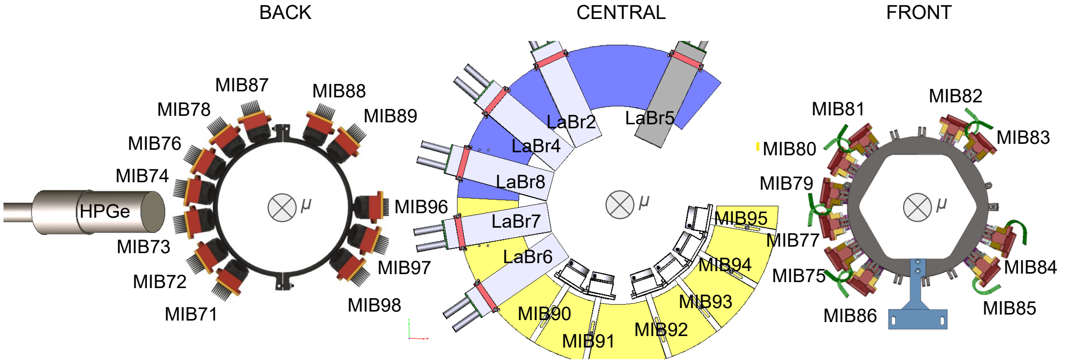

2024 detector setup (starting from *RAL202404*):

[July'24]

Figure 2.16: *X-ray detector positions in the three detector holders in the 2023 and 2024 setups. Detectors read by PMTs are marked with "LaBr", while detectors read by SiPMs with "MIB", which include also the ½″ ones in 2023 only (marked with text in blue and italics). Adapted from [56, 59].*

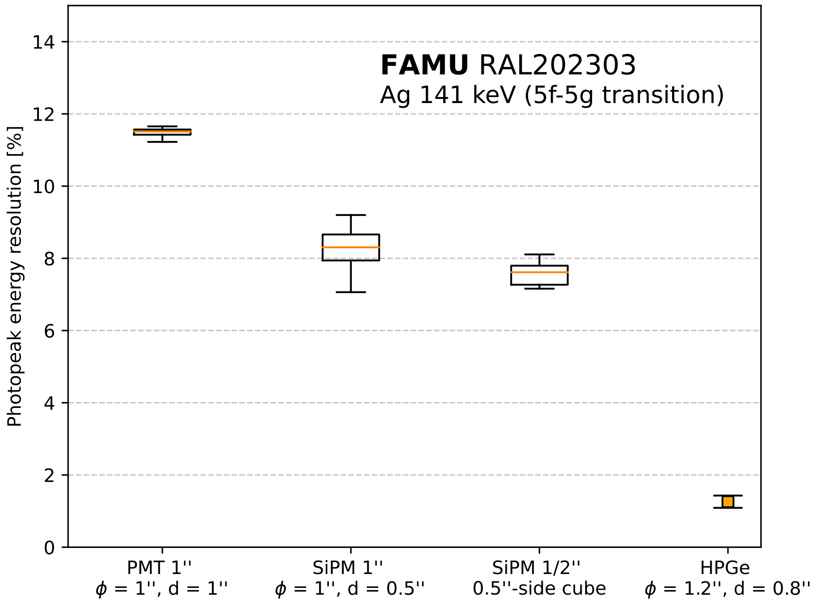

Figure 2.17: *Distribution of FWHM energy resolutions at the muonic silver peak corresponding to the 5f-5g transition (141 keV, theoretically calculated, chosen as close to the μO X-rays). The standard boxplot rules hold for scintillators: a set of box, errorbar and orange line mark the four quartiles in each dataset (i.e. the orange line corrsponds to the median value). Adapted from [56].*

Energy resolutions on the beamline, obtained from the reconstructed muonic silver peak at 141 keV for all detectors in a typical run on the full experiment setup with 55 MeV/c impinging muons, are reported in Figure 2.17.

Germanium detector

A commercial ORTEC GEM-S5020P4 High-Purity Germanium (HPGe) detector has been installed in the FAMU setup along with the scintillating detectors. The detector core is is a p-type coaxial germanium crystal (length 20.8 mm, diameter 30.4 mm) with a 0.9 mm carbon entrance window. The detector is supplied with 1.5 kV positive bias and the signals are treated with an ORTEC A257P preamplifier and an ORTEC 672 gaussian amplifier, with 0.5 µs shaping time. From the same measurements as the ones presented in the previous section, the FWHM energy resolution for the HPGe detector at the 141 keV muonic silver peak is $(1.26 \pm 0.17)\%$. Although the shaping time and the typical signal length of HPGe detectors do not allow to extract timing information in the scale of hundreds of nanoseconds, the good energy resolution is a key factor in the target monitoring and in the beam optimisation for the experiment.

During the previous phases of the experiment[45, 46], the experimental setup involved several HPGe detectors to optimise the energy resolution. As the final FAMU setup required more focus on the timing performances of detectors, it has been decided to maximise the number of scintillating crystals and leave only one germanium detector, to be used for inter-calibration. To do so, the collaboration had to select which of the previously used detectors could be used for the 2023 setup of the experiment. In particular, two detectors were available:

- a n-type coaxial germanium detector (ORTEC **GEM-S**) with 21 mm thickness, 30 mm diameter, biased with +1.5 kV and a 900 μm carbon fibre entrance window;
- a planar germanium detector (ORTEC GLP **GEPLA**) with 7 mm thickness, 10 mm diameter, biased with −1.0 kV and a 130 μm beryllium entrance window.

Given that the two detectors and electronic chains have comparable timing performances, the main parameters to compare are the energy resolution and the detection efficiency in the FAMU energy region of interest (FAMU ROI, between 100 and 200 keV).

To compare the energy resolutions, a 0.1 μCi ^{57}Co radioactive source was used. This source fits for the job as it emits two X-rays at 122 keV and 136 keV, which are both in the FAMU ROI. As usual, the energy resolution is obtained as the FWHM from fitting the peak with a gaussian. Table 2.3 shows the energy resolutions for the two detectors corresponding to these two peaks. The planar detector has better energy resolution by a factor > 2, but both are much better than those obtained with the scintillators (see Table 2.2).

Table 2.3: *Energy resolution for GEM-S and GEPLA HPGe detectors measured at the 122 keV and 136 keV peaks in ^{57}Co.*

Detector	En. Res. (%) @122 keV	En. Res. (%) @136 keV
GEM-S	1.0099 ± 0.0007	1.015 ± 0.002
GEPLA	0.4159 ± 0.0007	0.398 ± 0.002

On the other hand, determining the detection efficiency is not as straightforward. In fact, only sources with a certified activity can be used. This allows to convert the number of counts below a peak in an estimation of the efficiency, as the activity is considered well known. The source available is Eckert & Ziegler UW878, containing certified amounts of ^{241}Am (60 keV), ^{137}Cs (662 keV) and ^{60}Co (1173 keV, 1333 keV). These sources don't allow an estimation of the efficiency in the FAMU ROI, but they can be used to optimise a simulation of the detector[64], which can then be used to calculate the efficiency in the ROI.

All simulations have been carried out using Arby[65], an interface to the simulation toolkit Geant4[66] based on the interpretation of a configuration file. The simulation geometry for both detectors had already been carried out as a part of the past FAMU activities. The optimisation consists in slightly modifying detector volumes thickness to minimise the distance between the simulated and measured efficiencies, calculated respectively as:

$$\varepsilon_{\mathrm{MC}} = \frac{C}{\mathrm{BR}N}, \qquad \varepsilon_{\mathrm{exp}} = \frac{C}{\mathrm{BR}A\Delta t}, \tag{2.8}$$

where C is the integral under the peak (counts), `BR` the branching ratio of the observed γ-ray, N the number of simulated decays, Δt the measurement live duration and A the activity for the analysed isotope in the day of the measurement. The value of A is obtained from the certified value A_0 as $A(t) = A_0 e^{-t/\tau}$, where A_0 is the certified activity, t is the time distance between the certification and the measurement and τ the mean lifetime of the analysed isotope. The activities in the day of the measurements were approximately 3.4 kBq for ^{241}Am, 2.2 kBq for ^{137}Cs and 1.0 kBq for ^{60}Co. Figure 2.18 shows the comparison among experimental and simulated data with the optimised and unoptimised geometry for GEM-S.

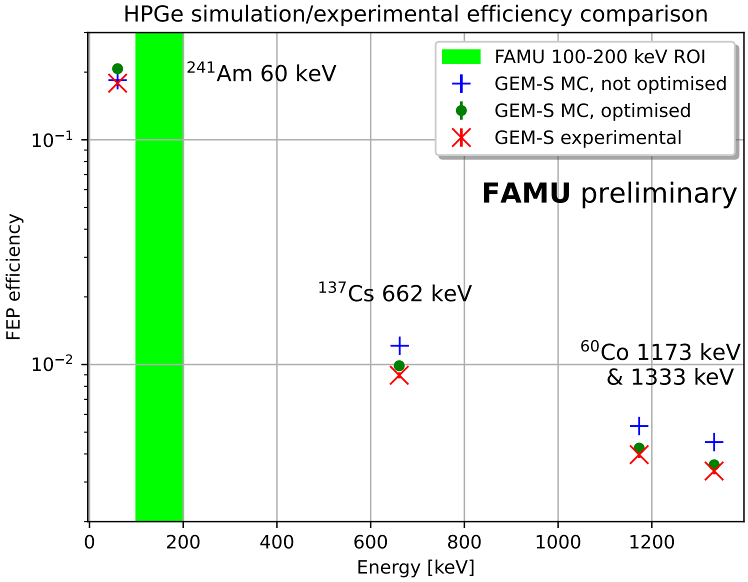

Figure 2.18: *Comparison among efficiencies determined from experimental measurements (red cross) and Monte Carlo (MC) simulation with the declared geometry (blue plus), and the optimised geometry (green point). Results obtained using γ-rays from ^{241}Am, ^{137}Cs and ^{60}Co, which are out of the highlighted FAMU energy region of interest.*

Eventually, Figure 2.19 shows the efficiency curves obtained with the optimised geometry for the two detectors. It is important to notice that these estimations hold for the simulated geometry (source UW878 in front of the entrance window), and not for the FAMU setup, in principle. However, the comparison between the two curves in the FAMU ROI gives an estimation of

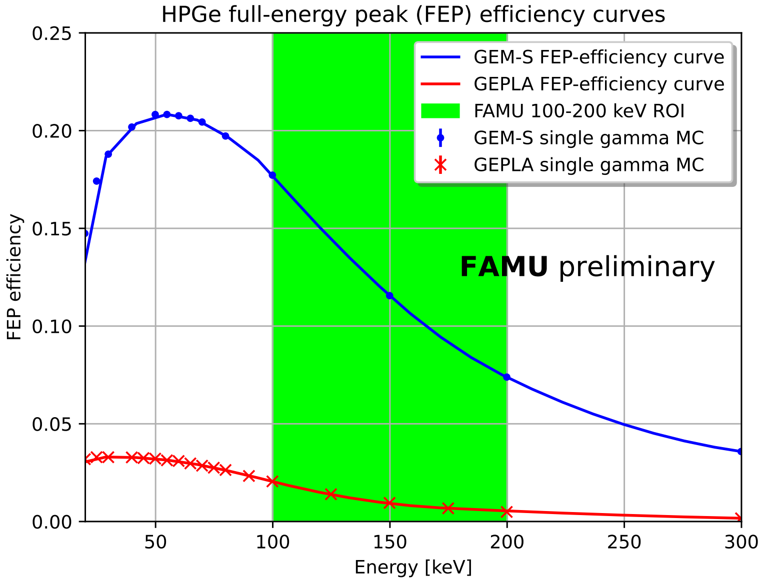

Figure 2.19: *Simulated efficiency curves for the UW878 source. The higher efficiency for GEM-S in the FAMU ROI is the reason why this detector has been chosen for the final setup.*

the ratio between the efficiencies in this energy range, which can also hold for the FAMU esperiment provided the two detectors are positioned in the same place. The efficiency for GEM-S is more than 8 times higher than the efficiency for GEPLA, despite having only more than 2 times the energy resolution.

For these reasons, detector GEM-S has been evaluated as the best choice for a single HPGe detector in the FAMU experiment.

The measurement with the UW878 source lasted 1500 s (live time), with a dead time lower than 0.4% for both detectors, and the source in contact with the entrance window. The simulations to check the optimisation of the geometry were carried out by letting 10 million (N) isotopes decay in a random position within the active source volume. On the other hand, the simulations to plot the efficiency curve were carried out with 1 million events per each point, letting γ-rays of fixed energy to be emitted from random positions of the aource active volume.

2.4.4 Data acquisition and trigger system

The data acquisition system of FAMU (FAMU-DAQ)[67] handles 6 digitisers in two VME crates, located out of Port 1, to digitise all the required signals. A scheme of the typical readout system for each type of detector in the FAMU setup is shown in Figure 2.20, together with a picture of the main VME crate.

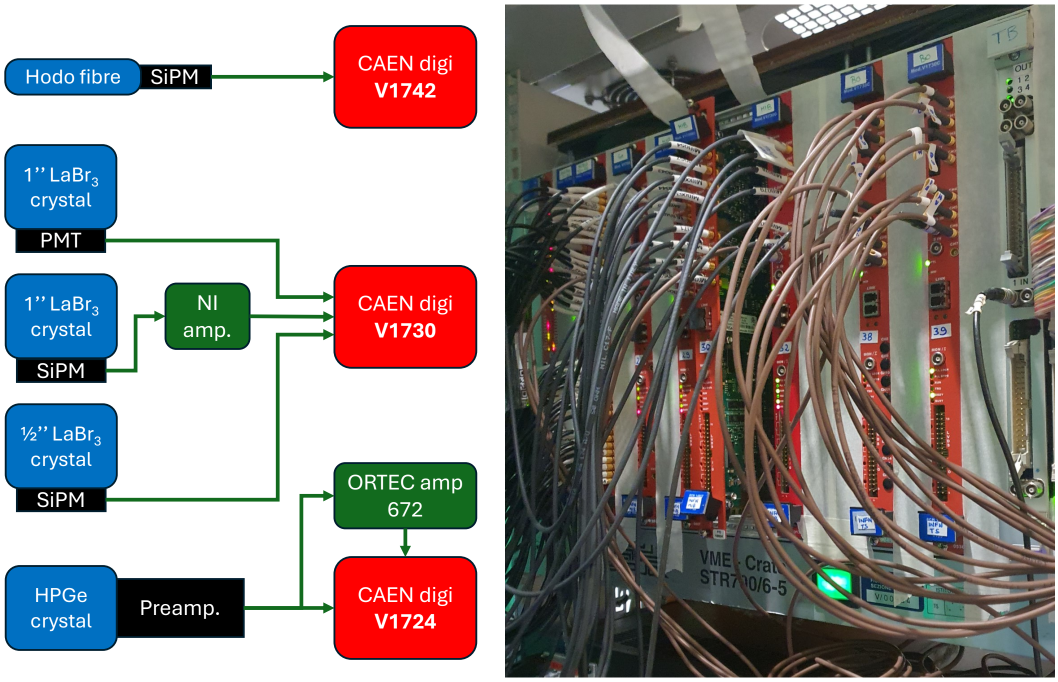

Figure 2.20: *Scheme of the DAQ electronics for all types of detectors (hodoscope fibres, scintillating crystals with different readout and HPGe detector) and close-up view of the main VME crate hosting the digitisers.*

The whole DAQ system is triggered by the muon beam and specifically by the Cherenkov scintillators placed in a hollow of the pion injection system.

The beam hodoscope signals are fanned out from the detector with 64 MCX connectors and each of them is digitised as-it-is. Two CAEN V1742 digitisers (32 channels, 5 GS/s, 12 bit) are used for this purpose, limited at 1 GS/s which is enough for the purpose.

All the signals coming from the scintillators, regardless of their readout system (PMT, SiPM or SiPM+amplifier), are fanned out through MCX connectors and digitised using a total of six CAEN V1730/V1730S ADCs (8 channels, 500 MS/s, 14 bit).

The germanium detector long signals are acquired with a CAEN V1724 (8 channels, 100 MS/s, 14 bit) in order to digitise over a longer time window and lower sampling rate. In particular, the signal is digitised both as-it-is and with a shaping carried out with an ORTEC 672 amplifier with 3 µs shaping time.

The trigger system allows three modes of operation: random trigger for hardware debug, external NIM trigger for normal beam operation and external TTL trigger for calibration. In particular, the latter is used to calibrate detectors with radioactive sources: one channel is used as a source of the TTL trigger signal, which is then distrbuted to all digitisers through a trigger board. During normal beam operation, instead, a NIM signal coming from the Cherenkov detectors in the pion beamline is distributed to the digitisers by the same trigger board.

The FAMU data acquisition system saves data in raw .root files, also called *raw* files. These files are then processed both online and offline as described in detail in Section 4.2 to obtain the final data. The software writes a *file* every 400 events, and 500 files (i.e. 200k events) form a *run*.

Chapter 3

Design and characterisation of hodoscopes for high-flux muon beams

The FAMU observable, thoroughly described in Chapter 2, is strongly dependent on the muon beam injected in the target, which changes the number of muonic hydrogen atoms formed. As a consequence, the presence of a beam monitor in FAMU is clearly crucial both for beam control (Section 2.3) and data normalisation (Section 4.3.1). As further specified, most of the research activities presented in this Chapter have been published in 2024[55, 68].

3.1 Hodoscope design and implementation

A set of scintillating fibre-based hodoscopes have been designed and implemented for the FAMU experiment. The main requirements for the detectors were:

- the limited amount of DAQ channels, 64, divided in two separate digitisers;
- having a broad active area of few cm in order to see the whole beam spot;
- having a good space resolution, in the order of the mm, to be sensitive to small variations in the beam focusing;
- having little material immersed in the beam, in order not to interfere much with the rest of the experiment.

In order not to have circuit boards or other complex materials immersed in the beam, and to keep costs low, the geometry consists of two planes of polystyrene scintillating fibres (with perpendicular directions) read-out by one side by a Silicon PhotoMultiplier (SiPM). The fibres are model BCF-12 by Bicron/Saint-Gobain/Luxium, with blue scintillation light (peak wavelength 435 nm), 3.2 ns of decay time, and a light yield of $\sim$ 8000 photons/MeV for Minimum Ionising Particles (MIP). The scintillating fibres have squared section, in order to have a standardised distance travelled by particles in the fibre, and a varnish coating to avoid optical cross-talk. The coating material and thickness is different between the different models of hodoscope.

Fibres are read-out on alternate ends by SiPMs held in four Printed Board Circuits (PCBs). Each PCB provides the same bias to all 16 SiPMs and fans out the 16 signals through MCX connectors. Three models of hodoscope were developed, as summarised in Table 3.1, in order to optimise the compliance to the upper conditions.

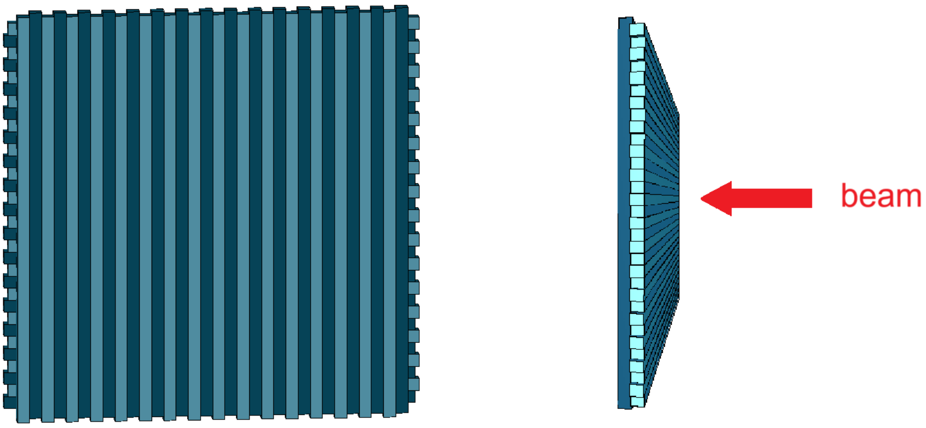

Figure 3.1: *CAD drawing of the fibre planes of a 3 mm-pitch hodoscope. Close-up of the vertical fibre plane (X plane), while the horizontal fibre plane (Y plane) is visible behind. The particle beam enters the hodoscope perpendicular to the two planes, as shown on the right. Courtesy of INFN Milano-Bicocca mechanical workshop (G. Ceruti).*

The first prototype was produced in two versions: Hodo-2 and Hodo-3[69, 70]. They are wide-area hodoscopes made with 32+32 adjacent 3 mm-pitch fibres, resulting in a 9.6×9.6 mm^2 active area. Each fibre is coated with a 50 µm aluminium foil and it is read-out by a Hamamatsu S12752-3050 SiPM, with area 3×3 mm and 50 µm cell size. This detector was mounted in the the first FAMU data taking in 2014 (R484). However, the space resolution over 3 mm and the detector thickness of 6 mm prompted the R&D aiming at other solutions.

Hodo-1[68–70] is a compact detector composed of 32+32 adjacent 1 mm-pitch scintillating fibres coated with a $\sim$ 15 µm layer of TiO_2-based extramural absorber. Originally projected for the FAMU 2015 – 2016 data taking (R582) to reduce the detector thickness (2 mm), it has a smaller active area of 32×32 mm^2. The fibre read-out is done using AdvanSiD 1×1 mm^2 SiPMs with 40 µm cells.

Hodo-4[55, 56, 71, 72] is the final detector mounted in the FAMU setup in 2023. For this reason, this is also hereby referred to as just *the FAMU hodoscope*. It is a compromise between the previous designs, and it hosts 32+32 1 mm-pitch scintillating fibres, coated with ~ 15 μm of TiO_2, interspaced by 1 mm from each other. The interspacing allows for an increase of the detector area with respect to Hodo-1 (64×64 mm^2), keeping a maximum thickness of 2 mm. However, this detector has a much more complex response function, as the energy deposited by a particle depends on how many fibres (0, 1 or 2 most likely) are on its path.

In the FAMU Data Acquisition System (FAMU-DAQ)[67], hodoscope signals are fanned out through MCX connectors and acquired using two CAEN V1742 digitisers (32 channels, 5 GS/s, 12 bit).

Table 3.1: *Design features of the set of FAMU hodoscopes.*

Hodoscope	**Fibre pitch**	**Interspacing**	**Thickness**	**Active area**
Hodo 1	1 mm	0 mm	2 mm	3.2×3.2 cm^2
Hodo 2/3	3 mm	0 mm	6 mm	9.6×9.6 cm^2
Hodo 4	1 mm	1 mm	0 – 2 mm	6.4×6.4 cm^2

All setups have been simulated in Geant4 to understand their behaviour (see Section 3.3). Hodo-1 was tested with low rate at CNAO, as reported in Section 3.4, whereas Hodo-4 was tested directly in its final FAMU setup at RIKEN-RAL Port1, see Section 3.5.

3.2 Hodoscope operation and calibration technique

This section explains how to operate the detector as a flux monitor and presents the low-rate calibration technique for hodoscopes and the two different analysis techniques that were used for low-flux data reduction. The results and methods exposed in this section have also been published in two articles[55, 68].

During normal operation of the FAMU experiment, the beam is tuned to have the highest possible flux (for details see Section 2.3). As the order of magnitude for the muon flux at 55 MeV/c is 10^5 muons per second and every second two beam spills are delivered with an average repetition rate of 40 Hz, more than 100 muons are delivered in every spill. The width of each spill is $50 - 70$ ns, making it impossible to de-convolve single muon signals (typical signal length in Hodo-4: 20 ns).

To enable the estimation of the muon flux, a low-rate calibration is needed, to determine the average charge deposited by a single muon in the detector (Q_μ). In principle, this value can be compared to the total charge deposited during a beam double spill (Q_{tot}) to extract the number of muons crossing the detector[71, 72]. To do so, a low-rate source of heavy charged particles is needed. Isotopes emitting β rays (such as ^{90}Sr/^{90}Y) can be used to test the DAQ but not for detector calibration due to their continuous spectra and the different interaction carried out by electrons. In fact, muons mostly behave as heavy charged particles in matter and not as electrons.

A first approach is to use cosmic rays, positioning the detector horizontally over a trigger scintillator and measuring the average charge deposited by a cosmic muon (Q_c). Considering cosmic muons Minimum Ionising Particles (MIPs), the valus of Q_c has to be converted to Q_μ by scaling it using the Bethe-Bloch profile for dE/dx, which introduces a systematic uncertainty on the value of Q_μ. As a consequence, calibrating with a beam of particles dropping a charge Q_μ allows a direct estimation of its value and it is more trusted. This procedure had been tested in the past on Hodo-1,2,3[70].

A second possible approach is to tune a low flux proton beam, available at most proton synchrotrons, to match the simulated energy loss of the muons to be used in the experiment. This enables a direct estimation of Q_μ, even though it still carries some systematic uncertainty due to the different beam shape and the particles not exactly matching their behaviours. This approach has been carried out on Hodo-1 at the CNAO synchrotron in Pavia using low-flux 150 MeV protons, as presented in Section 3.4 and published[68].

Eventually, the best possible approach is to tune the used muon beam to deliver a very low rate which allows single particle identification. This is quite delicate as it requires thorough beam tuning and it needs to be carried out directly at RIKEN-RAL Port1, subject to beam availability and magnet capabilities. However, it allows to test the detector with the same particles used for the experiment, at the same momentum, without moving the detector from its position. This enables a more accurate calibration, which can be easily repeated over time to check the detector performance. This procedure has been carried out for Hodo-4 as reported in Section 3.5 and in a paper[55].

In principle, for an ideal dense and continuous hodoscope and a collimated and non-diverging muon beam, the number of muons in a single muon spill can be derived from the integrated charge on the detector during the spill (Q_{tot}) as $N = \frac{Q_{tot}}{Q_\mu}$. Knowing the spill repetition rate r one can then derive the muon rate as:

$$\varphi_\mu^{\text{ideal}} = \frac{r}{Q_\mu} Q_{tot}. \tag{3.1}$$

However, the volume occupied by fibre spacing and fibre coating is not active and degradates the value of Q_μ. This effect has to be evaluated by simulating the detector in order to understand the amount of particles interacting with 0, 1, 2 fibres or more. In addition, the beam divergence and the spread of scattering angles have to be carefully evaluated in order to exclude that further effects have to be taken into account. Let's assume a fraction W_2 of muons interact with 2 fibres depositing on average a charge Q_2, then a fraction of particles W_1 interact with 1 fibre depositing on average Q_1 and a fraction of particles W_0 don't interact with active areas and deposit no charge in the fibres ($Q_0 = 0$). In addition, to refine the estimation, the charge deposited by muons interacting with 1 fibre might change between the front and back plane. We will therefore write separately the probability of passing from the front W_1^F and the back plane W_1^B and their deposited charges, Q_1^F and Q_1^B, respectively. As a consequence, the general equation for the flux estimation is:

$$\varphi_\mu = \frac{r}{W_2 Q_2 + W_1^F Q_1^F + W_1^B Q_1^B}\, Q_{tot}, \tag{3.2}$$

where the three charges Q_2, Q_1^F and Q_1^B are a function of the experimental value of Q_μ, depending on the hodoscope geometry. As a consequence, whereas r is generally known and Q_μ is obtained through low-flux calibration, all the other factors have to be extracted from the simulation, and the equation can be therefore simplified for the specific case. The details, operative equations and computed parameters for the specific cases studied in this work are reported in Section 3.3.

In order to extract Q_μ with a trusted procedure from low-rate data, it is important to select the events in which only one particle interacted with both planes of fibres. In this work, two methods have been applied:

- the first and simplest approach consists in asking that one and only one fibre on each plane has a signal (*i.e.* integrated charge over a given threshold) in the time window following a trigger. This method is described in Section 3.2.1;
- the advanced approach consists in looking for waveforms in the fibres and asking that there are one and only one signal per plane (*i.e.* pulse height over a given threshold) within a time frame of 50 ns. This second approach is described in Section 3.2.2.

When data reduction is carried out, the resulting histogram of deposited charge has to be fitted in order to extract the average charge deposited in two fibres Q_μ. The value of total deposited energy for every event is the sum on all fibres of the integrated charge $Q_{tot} = \sum_{j=1}^{64} Q_j$. This holds for both low- and high-rate measurements. As one can see in Sections 3.4, 3.5, the shape of the Q_{tot} histogram for low-rate measurements is asymmetric. After exploring some possibilities (combination of Landau and Gauss profiles), it has been decided to fit this histogram with the convolution of a Gaussian and a decreasing exponential profile, i.e.:

$$\begin{aligned} F(x) &= A \int_{-\infty}^{x} dt\ e^{-t/\tau}\ G_{\mu,\sigma}(x-t) \qquad (3.3) \\ &= C + A \exp\left[-\frac{x-\mu}{\tau} + \frac{\sigma^2}{2\tau^2}\right] \left(1 + \operatorname{erf}\left(\frac{x-\mu-\sigma^2/\tau}{\sqrt{2}\sigma}\right)\right), \end{aligned}$$

having 5 free parameters: additive constant C, amplitude A, Gaussian mean μ, Gaussian sigma σ and exponential decay constant τ. The fit boundaries are chosen by looking for optimal and stable reduced χ^2. The maximum, which corresponds to the estimate for Q_μ, has no known analytical expression. As a consequence, it has been determined on the fit function through numerical Brent method[1]. The uncertainty on Q_μ is obtained by variations of the fit boundaries around the optimum. This is done recursively in order to select a region in the two fitting boundaries in which $\chi^2/NDF < 1.3$. The variation of Q_μ in this region is then used as an estimation for its uncertainty.

3.2.1 Low-flux data reduction with XOR method

The threshold-XOR data reduction method has been described in [68]. The first step consists in extracting, for every *event* (i.e. for every trigger), the pulse integral over time of each fibre. As a SiPM signal consists in a current pulse $I_{fib}(t)$, its integral is a total deposited charge Q_{fib}, which is proportional to the total energy deposited by the particle in the fibre ΔE_{fib}.

Two conditions are applied for each event as follows. The first condition is to decide whether a fibre is to be considered ON or OFF on that event. This is done by imposing that Q_{fib} is greater than a given threshold `thrs`. After the first step, we want to select single-particle events only. In the easiest approximation ($W_2 = 1$), particles are expected to cross one fibre for each plane and exit the detector on the other side. Thus, single-particle discrimination is obtained by checking for each event if exactly two fibres are ON, and in particular they must be one on the X-oriented plane and one on the Y-oriented plane. As the strongest condition here is the exclusive `OR` (`XOR`) on each fibre plane, this condition is referred to as the *XOR condition.*

---

[1] using ROOT [73] method TF1::GetMaximumX()

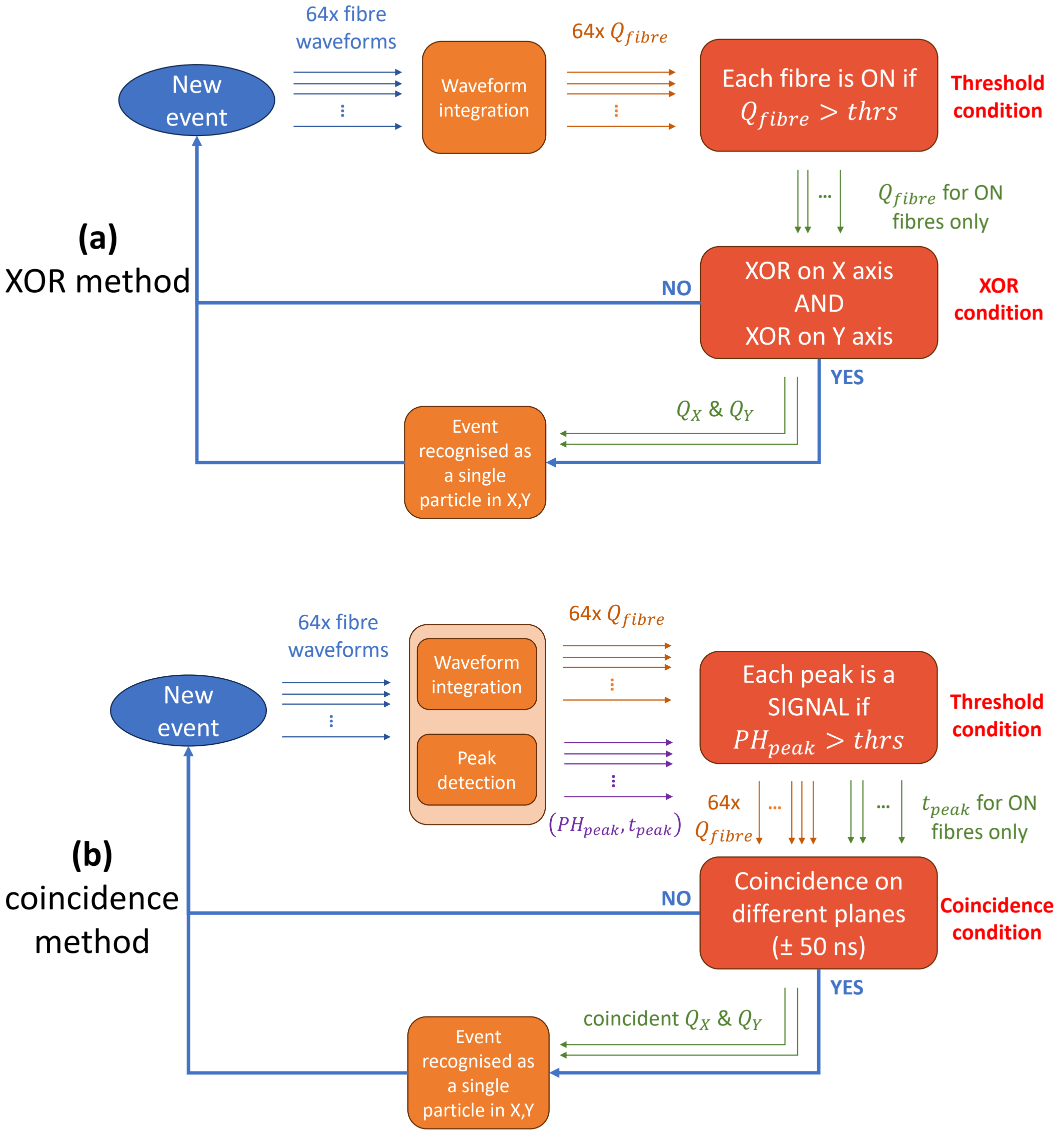

Figure 3.2: *Hodoscope data reduction methods used in this work: (a) the first approach* i.e. *the threshold-XOR method (see Section 3.2.1) and (b) the upgraded threshold-coincidence method (see Section 3.2.2). Taken from [55, 68], respectively.*

These two conditions can be summed up with the following logic equation ($\oplus =$ `XOR`):

$$\forall \text{ event, if } \left(\bigoplus_{j=1}^{32} Q_{fib}^{Xj} > \texttt{thrs}\right) \texttt{AND} \left(\bigoplus_{k=1}^{32} Q_{fib}^{Yk} > \texttt{thrs}\right) \Rightarrow \text{ single-particle,} \tag{3.4}$$

where it is clear that the number of selected events strongly depends on the value chosen for the threshold. In fact:

- if `thrs` $\to 0$, the threshold condition becomes too lose. In this case, fibres are considered ON even with background signals and therefore the XOR condition rejects almost all events;
- if `thrs` $\to \max(Q_{fib})$, the threshold condition becomes too strict and fibres with signals are considered OFF. In this case, it is the threshold condition rejecting all events.

As a consequence, there exists an optimum value of threshold which rejects most of the background without impacting too much the true signal. The method is summarised in Figure 3.2(a).

3.2.2 Low-flux data reduction with time coincidence method

In order to make sure that the signals result from the same particle interacting with the detector, it has been decided to move to a more strict data reduction process involving the time of arrival of the signal. The threshold-coincidence method has been described and applied in [55]. For each event and for each hodoscope fibre j, the hodoscope low-rate data processing system retrieves the waveform and looks for peaks, returning the total integrated charge Q_j and, for every peak k, the time-of-arrival t_j^k and the pulse height PH_j^k. At this point, the coincidence is imposed, with a tolerance of 50 ns (small enough to exclude particles coming from two different spills), for hodoscope peaks having PH_j^k over a certain threshold to be determined. Events having only one coincidence between the two planes are selected as single-particle events and therefore used for the hodoscope characterisation. Considerations similar to the ones made in the previous Section for the value of the threshold apply. This method is summarised in Figure 3.2(b).

3.3 Hodoscope simulation

In order to understand the energy loss of muons in the detectors, and therefore their theoretical response function, the hodoscopes have been simulated using the Geant4 [66] toolkit. The geometry consists of the fibres, coatings and entrance windows as described in Section 3.1. Each polystyrene fibre (pitch depending on the hodoscope as in Table 3.1) is coated with the corresponding coating and positioned in a 32-fibre plane. For Hodo-4, a 1 mm coating-to-coating fibre spacing is implemented. Two planes are juxtaposed with crossing fibre direction, separated from the world volume with a 0.1 mm-thick PVC window.

The muon beam simulated for this work is a 55 MeV/c negative muon beam with 2-dimensional gaussian shape, with $\sigma_X = (8.15 \pm 0.02)$ mm and $\sigma_Y = (10.354 \pm 0.012)$ mm. The shape was obtained from the FAMU hodoscope during 12 hours of full-rate data acquisition in the final beam configuration optimised for the experiment. The momentum corresponds to the central value of momentum used in FAMU.

In order to obtain an uncertainty budget, all simulations were repeated with gaussian dispersion of momentum (σ_p/p up to 10%, despite the nominal value is 4%[49]), variable beam size within the σ_X-σ_Y uncertainties, and variable coating thickness and fibre pitch (considering tolerances of 5 μm on the coating and 30 μm on the fibre pitch). This resulted in a geometric systematic uncertainty, which was added to the uncertainty budget as an independent contribution.

All primaries have been tracked and assigned flags depending on whether they passed by front and back plane fibres. In particular, muons passing by 0, 1 (front or back) and 2 fibres have been marked, and the related values of W_0, W_1^F, W_1^B and W_2 are calculated (see Equation 3.2). In hodoscopes with fibre spacing such as Hodo-4, it is crucial to evaluate the probability of interacting with 0, 1 or 2 fibres to estimate the muon flux. In hodoscopes without fibre spacing, the expected values would be $W_0 = W_1^F = W_1^B = 0$ and $W_2 = 100\%$, but the presence of the coating reduces W_2 in favour of W_0 and $W_1^{F/B}$. As a consequence the simulation is important to get a closer estimation of the beam.

3.3.1 Interspaced-fibre hodoscope simulation

In fibre-spaced hodoscopes such as Hodo-4, the probability of hitting 0, 1 or 2 fibres is about 25%, 50% and 25%, respectively, as one can derive from geometrical considerations from Figure 3.3, whose code-colour is used in the whole work, for clarity (0=blue, 1=orange, 2=green). However, the exact values of W_2 and W_1 depend on beam geometry, scattering processes and coating thickness, as a consequence they have to be extracted from the simulation. No difference is observed between muons interacting only with the first or only with the second plane of fibres. For this reason, Equation 3.2 can be written

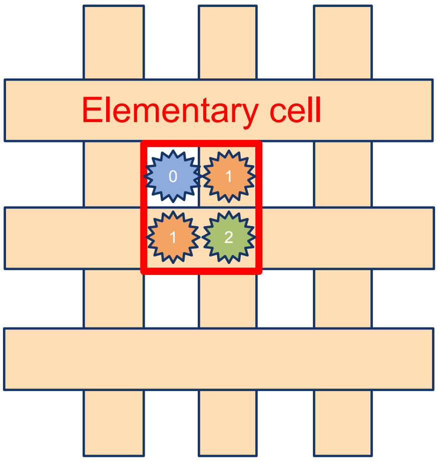

Figure 3.3: *Graphical representation of the hodoscope subdivision in elementary cells (red). As one can derive from the scheme, assuming uniform flux, muons can interact with either 0 (blue), 1 (orange) or 2 fibres (green) with probabilities* ∼ *25%, 50% and 25%, respectively. As a consequence, the heuristic values to be compared to the simulation are* $W_2 \sim 0.25$ *and* $W_1 \sim 0.5$*[55].*

with $W_1 = W_1^F + W_1^B$, $Q_2 = Q_\mu$ and $Q_1 = Q_1^F = Q_1^B = Q_\mu/\eta$, and it simplifies as follows:

$$\varphi_\mu = \frac{r}{\left(W_2 + \frac{W_1}{\eta}\right) Q_\mu} Q_{tot}, \tag{3.5}$$

where $\eta = E_2/E_1$ is the fraction of energy deposited in 1 fibre with respect to the one deposited in 2 fibres. The values of W_2, W_1 and η have to be extracted from the simulation to use this kind of hodoscope as a flux monitor.

Figure 3.4 shows the correlation between the energy deposit on the two planes of hodoscope fibres. The contributions from muons interacting with 0, 1 and 2 fibres are also plotted separately. The colour scale is fixed in range [0; 3000] counts for better contrast. The 0-hit case fills the (0,0) bin, in the 1-hit case the bins along the two axes are populated (as energy is released only on one fibre plane), while the area of the canvas is mostly due to 2-hit events. The points outside the expected areas are due to secondary particles interacting with fibres.

When running the simulation by launching 10^6 events, about $\frac{1}{4}$ of the muons interacted with two fibres, resulting in an estimation of W_2 with a statistical counting uncertainty of $\sim 0.2\%$. The uncertainty has been studied by repeating the simulation with variations in parameters as explained in Section 3.3. Other effects on W_2, such as small fibre misplacements, are expected to be averaged and cancelled out due to the beam spot size. In conclusion, the total uncertainty on W_2 is about 1.8%, and it is dominated by the uncertainty on the coating thickness. The final estimate for the double-hit fraction is $W_2 = (24.9 \pm 0.4)\%$. Similarly, the estimation of the single-hit fraction gives

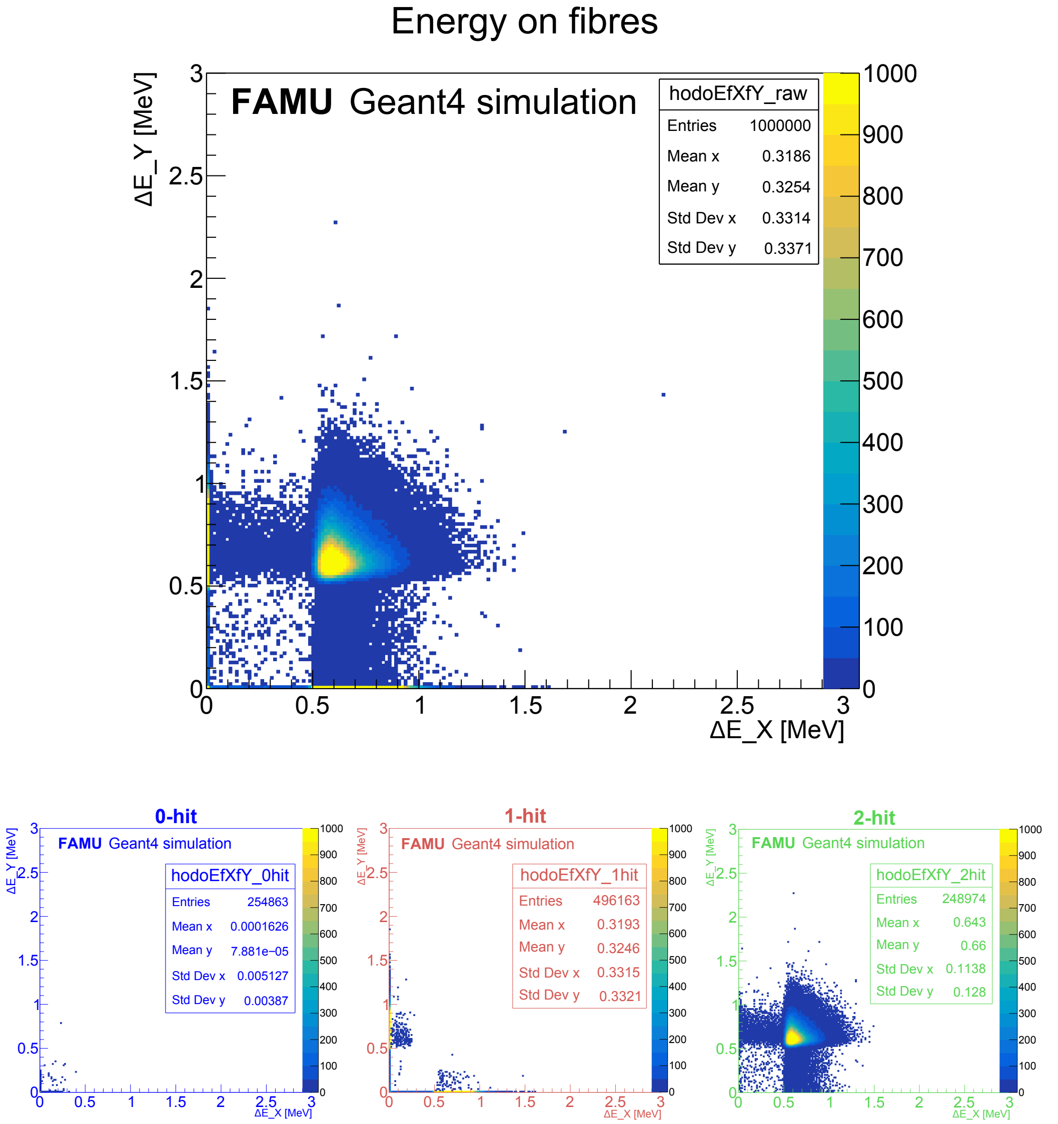

Figure 3.4: *Geant4 simulation (10^6 events): energy deposited by 55 MeV/c muons on the two planes of the Hodo-1 detector. The upper canvas contains the total plot, whereas the lower panels show the contributions from muons interacting with 0 (first, blue), 1 (second, orange) and 2 fibres (third, green). The contributions produce zero deposit, deposit on the two axes and deposit in the area, respectively. Outliers from these contriutions are given by secondary particles interacting with fibres. The colour scale is fixed 0 – 1000 to enhance contrast; values exceeding 1000 are plotted with the same colour.*

$W_1 = (49.61 \pm 0.09)\%$. In principle, assuming local linearity of the Bethe-Bloch curve, one could assume that the energy released by single-hitting muons is $Q_\mu/2$ (i.e. that $\eta = 2$). To check this, single- and double-hit simulated spectra have been fitted with Equation 3.3. Following uncertainty estimation through parameter variation, the estimated energy deposits are $E_2 = (1.23 \pm 0.06)$ MeV for the 2-hit case and $E_1 = (0.58 \pm 0.03)$ MeV for the 1-hit case. The beam momentum straggling following from this energy deposits are comparable to the incoming beam momentum bite ($dp/p \sim 4\%$ ([49])). As a consequence, the presence of the hodoscope doesn't influence the FAMU data. The estimate for the ratio between the double-hit and the single-hit mean deposited energy is $\eta = E_2/E_1 = 2.11 \pm 0.05$.

The Geant4-simulated spectrum is plotted in Figure 3.5, overlayed with the separate contributions for muons interacting with 0, 1, 2 fibres. Figure 3.6 shows that the energy deposit on the entrance and exit PVC windows is of about 0.1 MeV each. The energy deposit in coatings is shown in Figure 3.7, where two main behaviours are visible:

A. the structure from 0.1 to 0.4 MeV corresponds to muons entering the coating twice, before and after interacting with a fibre, and it is therefore absent in the 0-hit case;

B. the peak between 2 and 2.5 MeV/c corresponds to muons interacting only with the coating and parallel to the fibre, hence it is not present in the 2-hit case.

In parallel, an independent simulation based on the FLUKA-CERN ([74, 75]) toolkit was also developed using the Flair interface ([76]) at the ISIS Neutron and Muon Source, for comparison. This toolkit will be reported just as FLUKA for simplicity. The FLUKA simulation has been modeled to match the exact detector and beam geometry as the Geant4 one. The geometric factors estimated with the FLUKA simulation are $W_2^{\texttt{FLUKA}} = (25.17 \pm 0.06_{\text{stat}})\%$ and $W_1^{\texttt{FLUKA}} = (49.94 \pm 0.07_{\text{stat}})\%$, with underestimated uncertainties as they comprise the statistical component only. Nonetheless, both values differ by less than 3 standard deviations (t-Student test) from the Geant4 predictions. Figure 3.8 shows a comparison between the Geant4 and FLUKA histograms. The FLUKA total spectrum has been fitted with Equation 3.3, to extract the 2-hit and 1-hit energy deposit predicitons: $E_2^{\texttt{FLUKA}} = (1.32 \pm 0.03)$ MeV and $E_1^{\texttt{FLUKA}} = (0.62 \pm 0.02)$ MeV. These values deposits differ by about 7% and 6%, respectively, from the Geant4 values, which is generally considered good accordance between the two models. Their ratio is $\eta^{\texttt{FLUKA}} = 2.13 \pm 0.08$, which is consistent with the value extracted from the Geant4 simulation.

The FLUKA simulation has been used to estimate the effective backscattering probability, *i.e.* the fraction of particles interacting with one fibre in the first plane, one in the second plane and then one back in the first plane, as a result of backscattering. The ideal value for this parameter is zero, for better

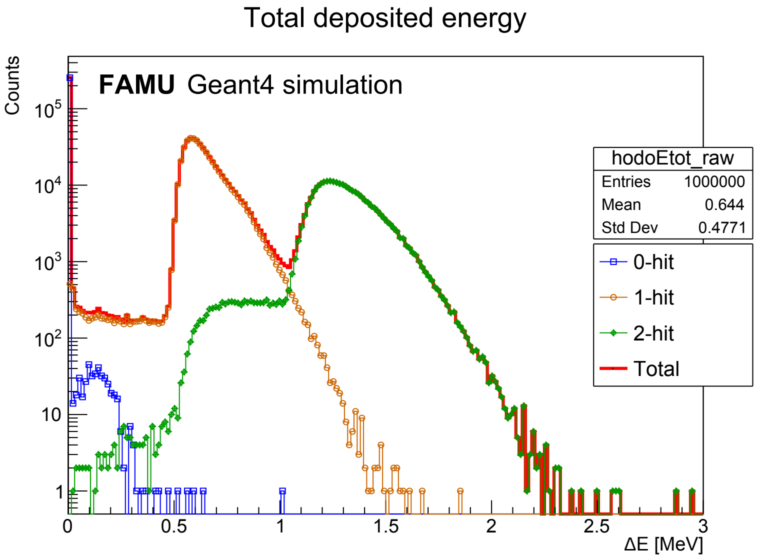

Figure 3.5: *Geant4 simulation (10^6 events): energy deposited in scintillating fibres by muons interacting with 0 (blue squares), 1 (orange circles) and 2 (green diamonds) fibres. The total contribution (thick red line) is the expected response function of the detector[55].*

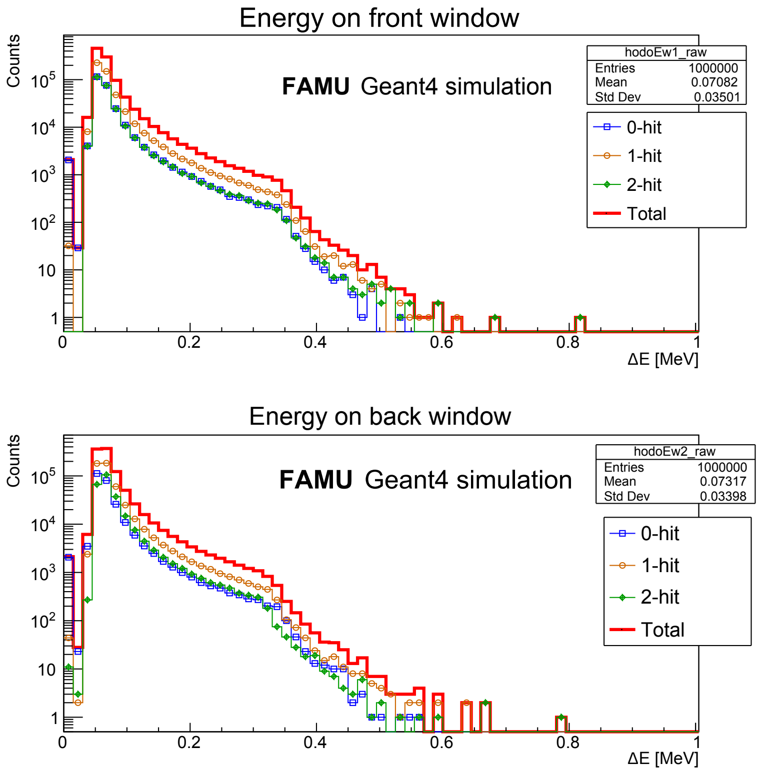

Figure 3.6: *Geant4-simulated (10^6 events) energy deposit for 55 MeV/c muons in front and back entrance windows (0.1 mm PVC) of Hodo-4.*

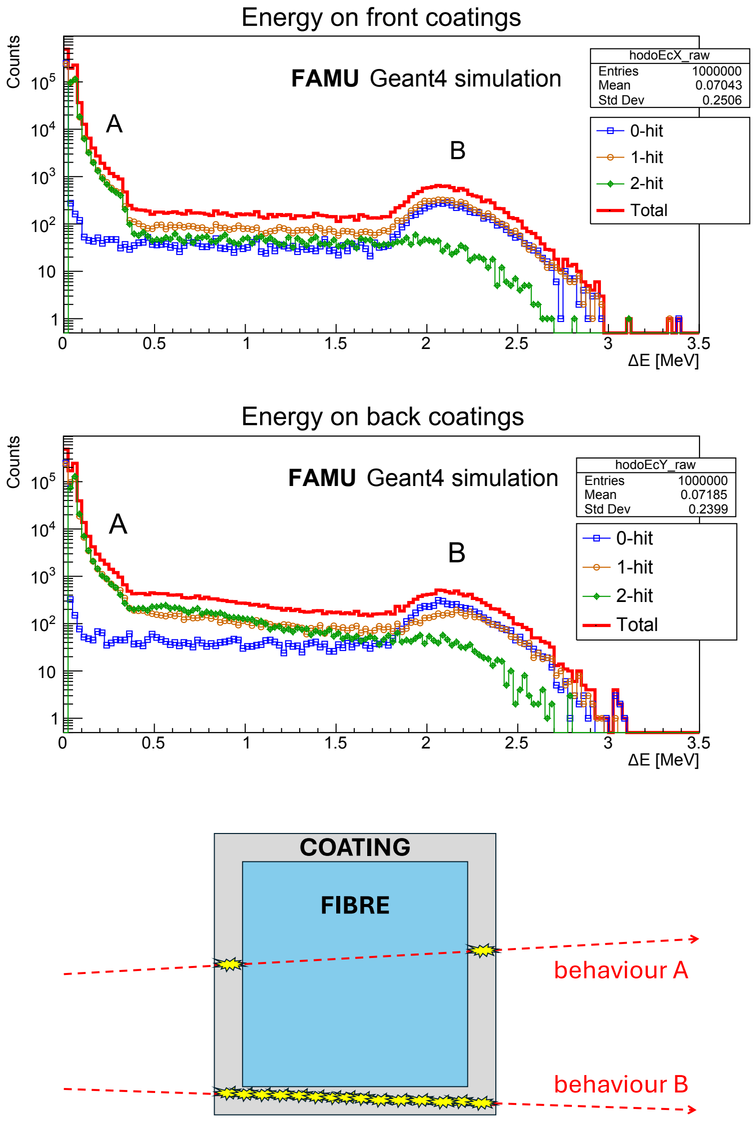

Figure 3.7: *Geant4-simulated (10^6 events) energy deposit for 55 MeV/c muons in front and back plane fibre coatings (0.015 mm TiO_2) of Hodo-4. The two main behaviours of muons in the coatings are shown in the scheme below: behaviour A is responsible for the structure in 0.1 – 0.4 MeV (which in fact is not present in case 0-hit), whereas behaviour B is responsible for the 2.0 – 2.5 MeV peak (absent in the 2-hit case).*

hodoscope accuracy. The effective backscattering rate is (0.013 ± 0.004) ‰, negligible.

Table 3.2: *Comparison between parameters estimated by the Geant4 and FLUKA simulation with* 10^6 *events simulated. The uncertainty balances are obtained through parameter variation, whereas those marked with "stat" are statistical only. The values of* W_2 *are consistent with each other, while the values of* W_1 *are comparable and differ by less than 3 standard deviations (t-Student test). The estimates of* E_2 *and* E_1 *differ by 7% and 6%, respectively, which is generally considered an acceptable range to compare results from different or independent simulation toolkits.[55]*

Tool	$\mathbf{W_2}$	$\mathbf{W_1}$	$\mathbf{E_2}$ (MeV)	$\mathbf{E_1}$ (MeV)	$\boldsymbol{\eta} = E_2/E_1$
Geant4	24.9 ± 0.4	49.61 ± 0.09	1.23 ± 0.06	0.58 ± 0.03	2.11 ± 0.05
FLUKA	$25.17 \pm (0.06)_{\mathrm{stat}}$	$49.94 \pm (0.07)_{\mathrm{stat}}$	1.32 ± 0.03	0.62 ± 0.02	2.13 ± 0.08

All the useful parameters extracted from Geant4 and FLUKA simulations are reported in Table 3.2. The coefficients for Equation 3.5 used in this work for flux estimation are taken from the Geant4 simulation, since the applied physics lists and transport thresholds had been already tuned and validated for the FAMU experiment.

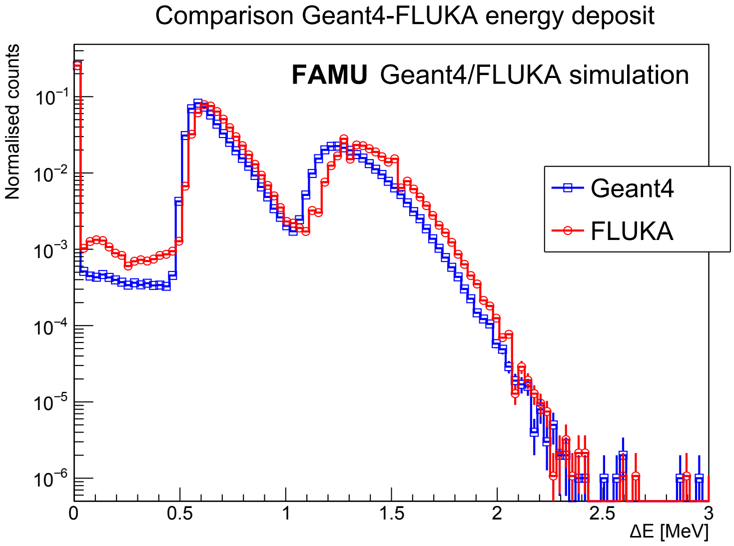

Figure 3.8: *Comparison of Geant4 (blue squares) and FLUKA (red circles) simulated energy deposited in hodoscope fibres* (10^6 *events). The two energy peaks differ by 6 – 7%, which is considered good accordance between the two approaches. Fine differences between the spectra are currently being investigated[55].*

3.3.2 Adjacent-fibre hodoscope simulation

The Geant4 simulation simulation developed for Hodo-4 was then applied to both 1 mm and 3 mm pitch hodoscopes without fibre spacing, in order to better understand their response function to the muon beam. Despite being simulated for various coating and entrance window features, the results reported in this paragraph were obtained with the same coating and windows as Hodo-4, for better understanding and comparison. In these cases, the yield of muons interacting with two fibres (one per plane) is clearly enhanced by the absence of spacing between adjacent fibres. Considering a 15 μm TiO_2 coating, the value of W_2 is estimated as $(96.45 \pm 0.10_{\mathrm{stat}})\%$ for 1 mm fibres and $(99.95 \pm 0.10_{\mathrm{stat}})\%$ for 3 mm fibres. As these detectors are not to be mounted in the FAMU setup, at the moment the other effects are not taken into account, and the flux is estimated as if $W_2 = 1$, i.e. with Equation 3.1.

Figure 3.9 shows the energy deposit by 55 MeV/c muons in the 1 mm (orange circles) and the 3 mm (green diamonds) adjacent fibre hodoscopes. Figure 3.10 shows the energy deposit in the two fibre planes. In the 1 mm case, the contribution of muons interacting with 0 or 1 fibres is visible and the plot is similar to the interspaced case. In the 3 mm case instead, most muons interact with two fibres and the effect of the coating is visible by the shifting of ΔE_Y. This happens because muons interacting only with the Y (back) plane have interacted with more than 3 mm of coating, which is denser than the fibre, and they are much less energetic than those who interacted with a fibre in the front plane.

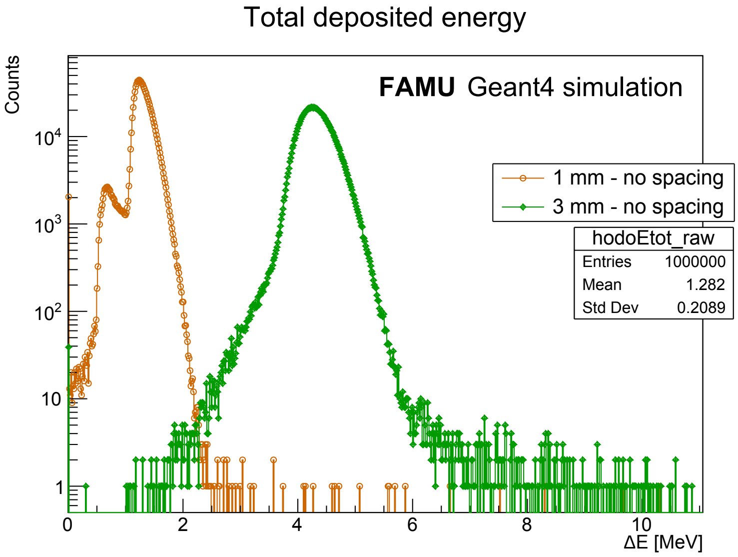

Figure 3.9: *Geant4 simulation (10^6 events): total energy deposited in scintillating fibres by 55 MeV/c muons interacting with contiguous 1 mm (orange circles) and 3 mm (green diamonds) fibres hodoscopes.*

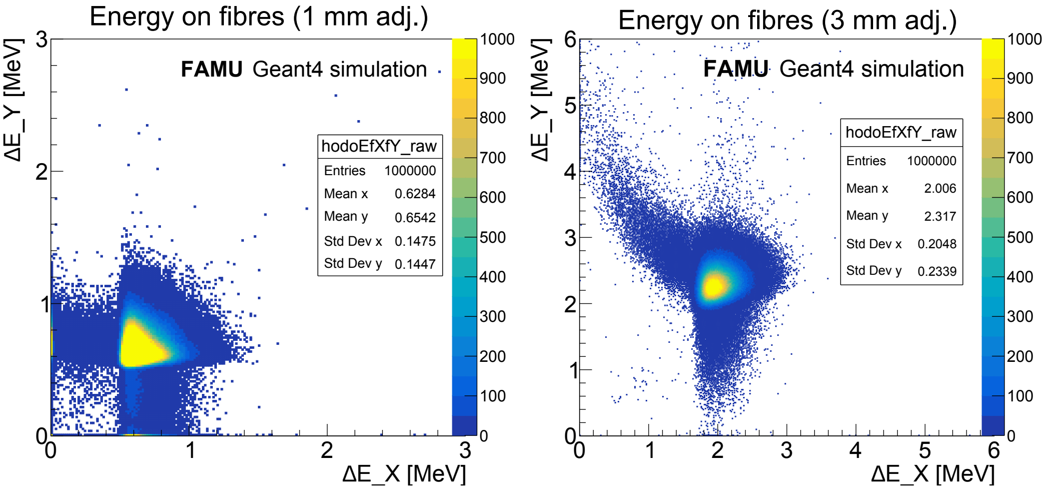

Figure 3.10: *Geant4 simulation (10^6 events): energy deposited by 55 MeV/c muons on the two planes of the adjacent-fibre detectors with 1 mm (left) and 3 mm fibres (right). While the former is similar to Figure 3.4, the latter is asymmetric as muons interacting with the back (Y) plane only have lost much energy by trespassing 3 mm of coating. Notice: the plots have different scales, but the colour scale is fixed at [0, 1000] counts for better contrast.*

3.4 Hodoscope characterisation with low-flux proton beams at CNAO

To enable the estimation of the muon flux, preliminary calibrations with cosmic muons have been made[69, 70]. However, cosmic muons deposit a different energy with respect to FAMU muons and the result need to be weighed by the correct dE/dx, introducing systematics. A new calibration method based on single particle measurement has been proposed for the FAMU hodoscopes[71, 72].

The method consists in calibrating the detector with proton beams, much more available than muon beams even at low rate, selecting the energy in order to match the dE/dx of FAMU muons thanks to detector simulation. Test beams at the CNAO synchrotron enabled the set-up of the analysis protocols described in Sections 3.2.1 and 3.2.2 and the test of DAQ performance. The test beam carried out on Hodo-1 (1 mm fibres, without spacing) is presented in this Section, and a paper based on it has also been published[68].

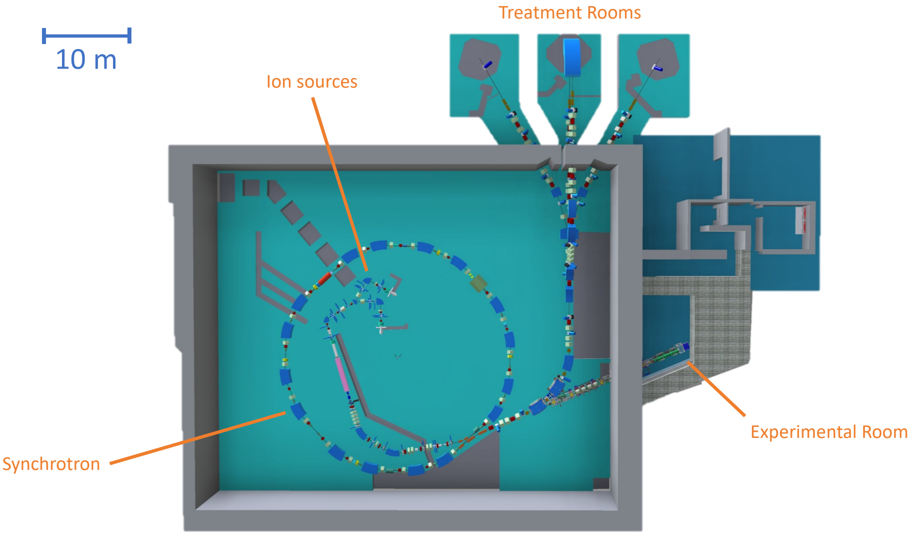

Figure 3.11: *The CNAO synchrotron: ion sources and position of experimental and treatment halls[68].*

Centro Nazionale di Adroterapia Oncologica (CNAO, *Italian National Centre for Oncologic Hadron Therapy*), in Pavia (Italy), is one of the four centres in Europe, and six worldwide, offering treatment of tumours with both protons and carbon ions. Besides clinical activity, CNAO has also *research* as institutional purpose. For this reason, in addition to the three treatment rooms, the CNAO center is equipped with an *experimental room* (CNAO-XPR) dedicated to experimental activities and available also to external researchers (see Figure 3.11 for a scheme of the facility). A scheme of the CNAO accelerator and beamline layout is shown in Figure 3.11. The CNAO synchrotron provides protons with kinetic energies between 63 MeV and 227 MeV. The beam is extracted from the synchrotron by a *resonant slow extraction*, to distribute the extracted particles over a time of about 3 s (called a spill). This leads to a discontinuous time structure of the beam with a pause of a couple of seconds between one spill and the following one.

Thorough Monte Carlo simulation of the detector in Geant4 shows that such protons have total energy of 150 MeV (momentum 550 MeV/c). A low-rate 150 MeV proton beam is a reachable condition at CNAO in treatment and experimental rooms, where the measurements reported here were carried out. Figure 3.12 shows the hodoscope mounted at the experimental beamline of the CNAO synchrotron. The detector is positioned in correspondance to the so-called isocentre. A cubed plastic scintillator (1 cm^3), positioned downstream from the hodoscope, was used to trigger the acquisition system. The beam was tuned to have a rate low enough to acquire single particles on each trigger.

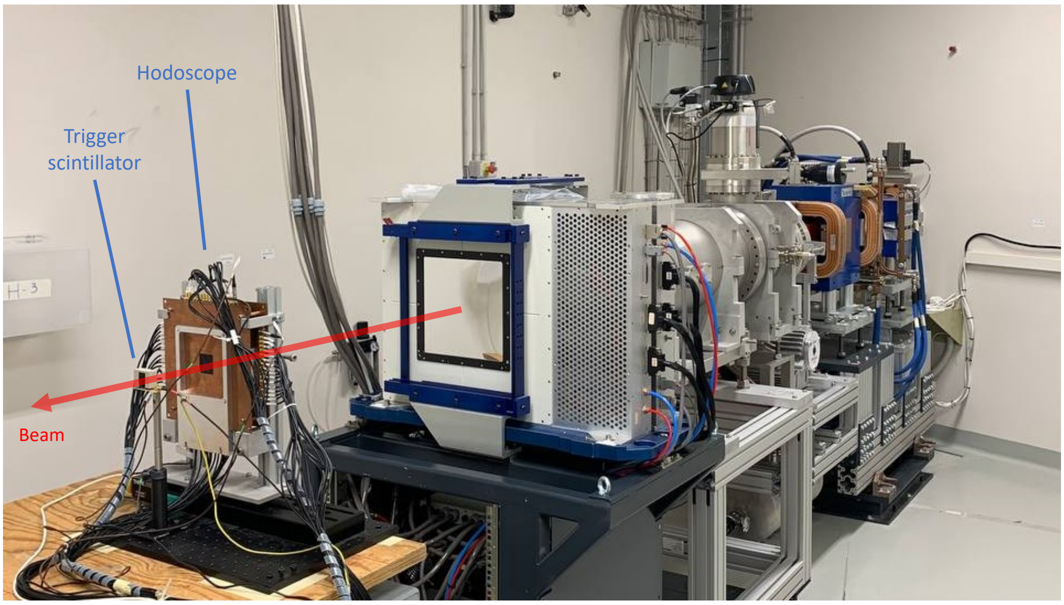

Figure 3.12: *The Hodo-1 beam monitor at the CNAO-XPR proton beamline[68].*

The calibration procedure described in [71, 72] has been carried out in February 2023 on a detector made of two planes of 32 adjacent scintillating fibres having 1 mm pitch. The measurements have been carried out at the CNAO synchrotron and the conditions applied during the analysis allowed to select the single-particle events.

Data reduction was initially carried out with the threshold-XOR procedure (described in Section 3.2.1) and the results are presented here and in [68]. Figure 3.13 shows the reconstructed beam shape with the optimised threshold (3500 ADC channels). The charge deposit on the two planes of the hodoscope is shown in Figure 3.14, where the optimised threshold (3500 ADC channels) is also shown. This value has been obtained as an optimum between background rejection and signal conservation. The background measurement, obtained by acquiring data without beam and with a random trigger, is also plotted in gray with the X-Y projections in Figure 3.14 for reference.

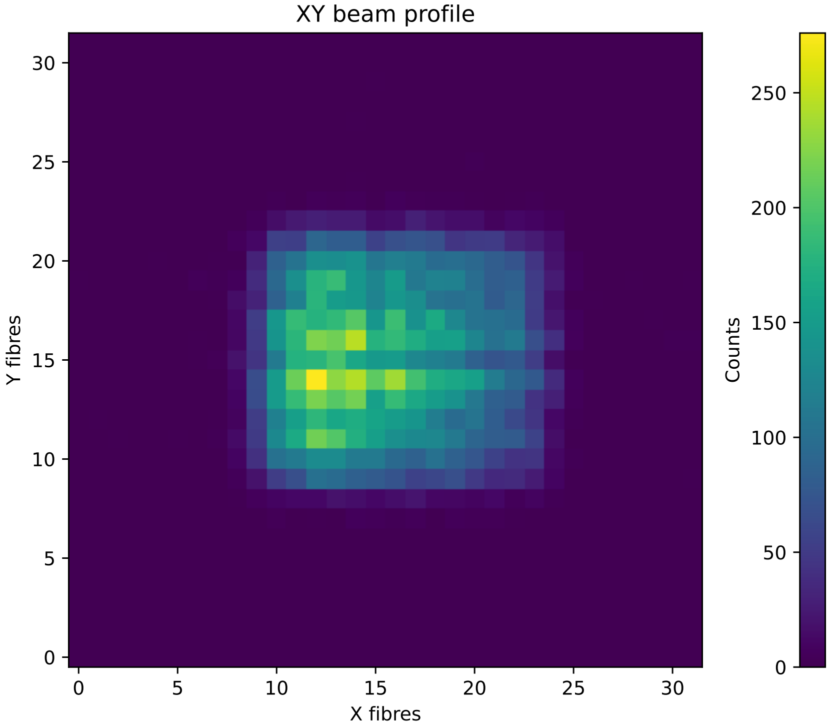

Figure 3.13: *Reconstructed CNAO 150 MeV proton beam shape with the threshold-XOR method (threshold 3500 ADC channels, 50k events) using the 1 mm fibre detector.*

This test beam was also used to develop the coincidence procedure (described in Section 3.2.2), and the results are reported here and compared to the previous ones. Also the threshold required by this method has been finely optimised during the procedure (final value: pulse height > 80 ADC channels). Figure 3.15 shows the comparison between the time of arrival on the X fibre plane for all reconstructed events (upper blue) and those above the threshold in time coincidence with similar signals on the Y plane (lower red). The time coincidence method, with an optimised choice of pulse height threshold, enables to select only beam events, which have a fixed ~ 515 ns delay from the beginning of the triggered acquisition window (pre-trigger).

Figure 3.16 shows a comparison of the deposited charge histograms obtained with the two analysis protocols. The Q_{tot} plots have been fitted with Eq. 3.3 to extract the average value of charge deposited in the detector by protons interacting with two fibres Q_p. The values obtained are $Q_p^{\mathrm{XOR}} = (27440 \pm 120)$ ADC channels for the threshold-XOR method and $Q_p^{tc} = (23600 \pm 80)$ ADC channels for the time coincidence method, where the uncertainties are obtained by considering the variation of the maximum of the fit as a function of the fit boundaries, in the region where the reduced χ^2 is below 1.2. The two values are not consistent with each other according to the t-Student test. In particular, the time coincidence method (more reliable) returns a lower value for Q_μ, which can suggest that the threshold-XOR method is not able in these conditions to fully separate single particle events. These values are not consistent with the preliminary Q_p estimation that has been published ($Q_p = (27950 \pm 50)$ ADC channels[68]), which had been obtained with gaussian fit in the top part as the fitting model Eq. 3.3 had not been considered yet.

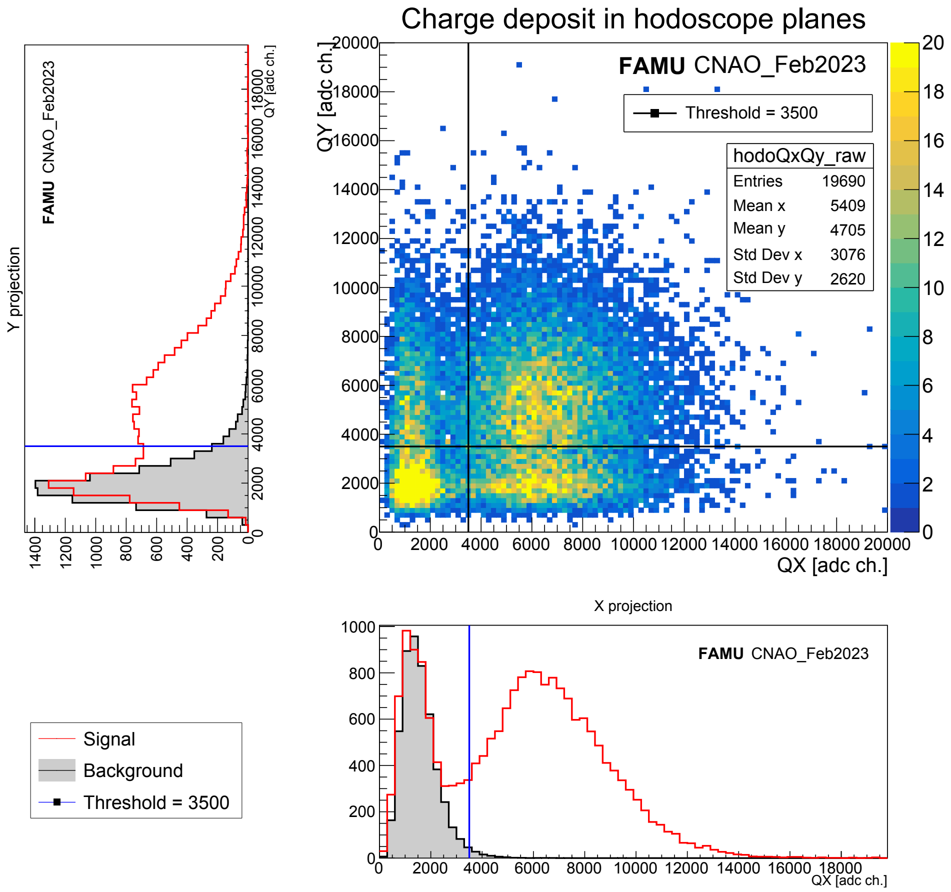

Figure 3.14: *Charge deposit on the X and Y fibre planes during a CNAO run at 150 MeV/c on Hodo-1. It compares well to the simulation (Figure 3.4), considering the presence of electronic noise which shifts the distribution away from the axes. In the threshold-XOR method, the threshold is chosen to optimise the rejection of background without compromising the signal. The threshold reported in these plots is the optimised one (3500 ADC channels) to select events when a particle interacted with both fibre planes.*

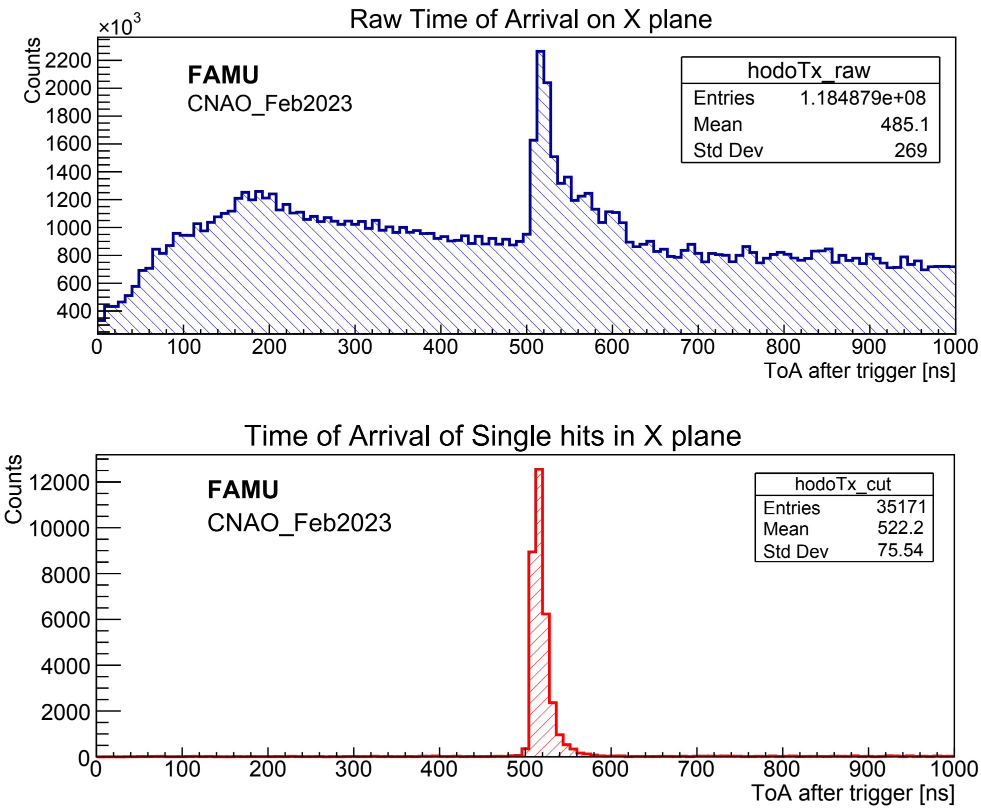

Figure 3.15: *Time of arrival of all reconstructed waveforms in the X detector planes (upper) and time of arrival for events selected by the time coincidence data processing with a threshold of 80 ADC channels on the pulse height (lower). Given the protons are mono-energetic and the digitiser pre-trigger is fixed, this confirms the selected events correspond to protons from the beam.*

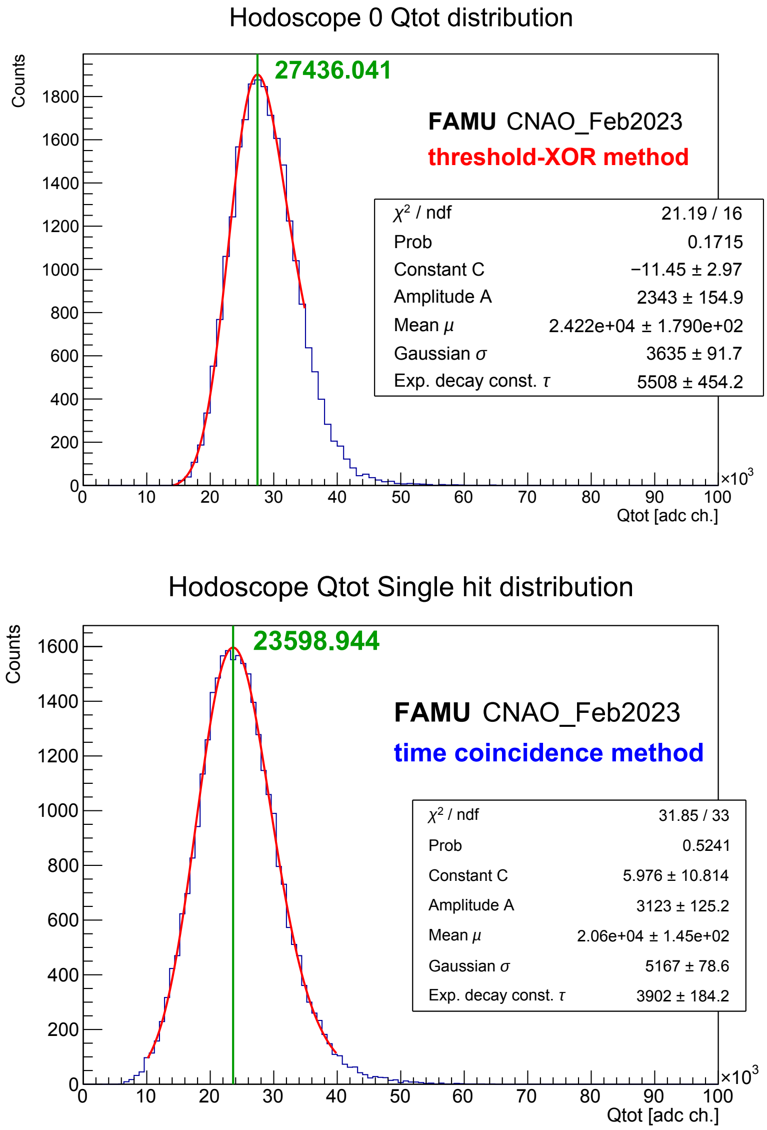

Figure 3.16: *Comparison of the fitted Q_{tot} histograms used to estimate of Q_p using the data selected with the two data reduction methods. The lower average energy for the time coincidence case shows that this method is more strict in selecting single particle data.*

3.5 Hodoscope characterisation with low-flux muon beams at RAL

The FAMU beam monitor (Hodo-4) had to be tested directly at RAL, as the proton beam availability at CNAO was not compatible with the FAMU setup installation schedule. As a consequence, it proved crucial to be able to reduce the muon flux to have a beam intensity suitable for single-particle discrimination. The method, data taking, data analysis and results reported in this Section have been published in [55].

The idea of obtaining low rate conditions at RIKEN-RAL Port1 resulted from observing the values of Q_{tot} after the magnet power supply faults during the December 2023 beam period (RAL202305). It has therefore been decided to de-tune some bending and quadrupole magnets to carry out the measurement at the end of the same beamtime. This data acquisition has been called RAL202306.

The first two quadrupoles (RQ1 and RQ2) were shut down in order to widen the pion bunch, and the first bending magnet (RB1) was de-tuned in order to direct the beam halo, and not its central part, into the beampipe. See Section 2.3 for a detailed path followed by the beam from the target to Port1. The choice of which magnets had to be tuned was done in order not to compromise the beam optics, which would result in not delivering the beam to Port1. The shut-down of the two quadrupoles resulted in a $\sim$90% beam intensity drop. The optimisation of the bending magnet current was carried out progressively in order to make sure that the rate would be as low as required. Figure 3.17 shows the effect of the progressive variation of the RB1 current out if its optimal value. The muon current (proportional to Q_{tot}) decreases, whereas the number of events marked as single coincidences increases until it reaches a maximum. This behaviour means that the muon flux is so low it allows events with only one coincidence, i.e. single-muon spills.

Regarding the actual data acquisition, these data were reduced using the time coincidence method only. Figure 3.18 shows the time of arrival for selected events for three values of the pulse height threshold. There is an evident structure preceeding the muon spill which disappears with the increasing of the threshold. These signals therefore correspond to impurities in the beam, possibly decay electrons, currently under investigation. The threshold has been chosen to be equal to 80 ADC channels, a value which is a compromise to reject beam impurities without compromising the statistics and the estimation of Q_{μ}. A histogram of the number of coincidences per event at different thresholds is shown in figure 3.19, where it is visible that the threshold at 80 ADC channels maximises the selection of single coincidences, and minimises the rejection of good single-coincidence events.

The energy deposit on the two planes, for the events selected during data reduction, is shown in Figure 3.20. The method of time coincidence over pulse height threshold allows to exclude signals from events in which more than one

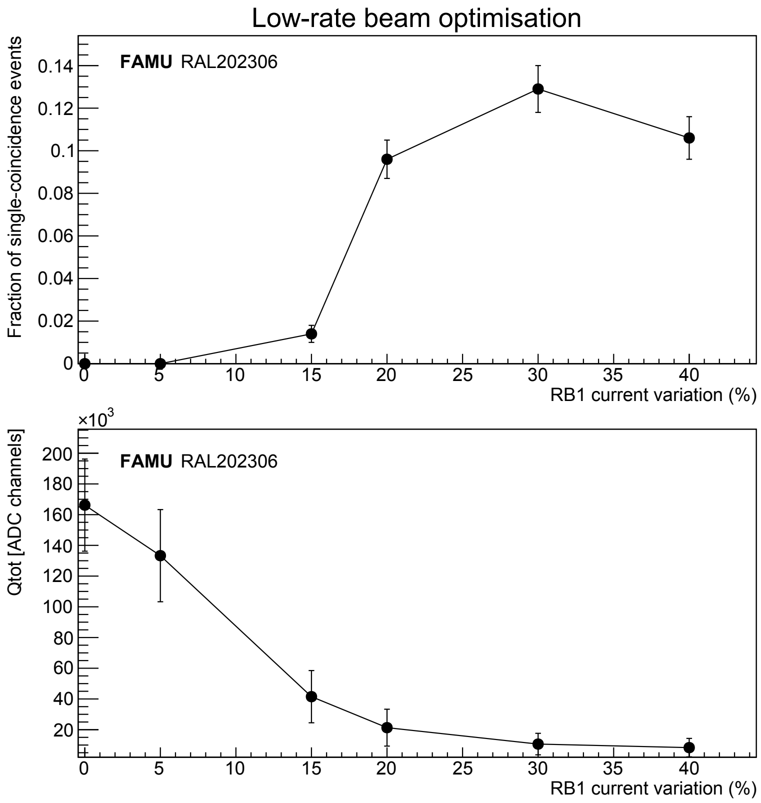

Figure 3.17: *Optimisation of the RB1 current to obtain the low-rate configuration. The upper panel shows the fraction of events selected as single-particle events as a function of the RB1 current displacement, while the lower one shows the related decrease of* Q_{tot}*. Working at RB1+*40% *guarantees low-rate conditions[55].*

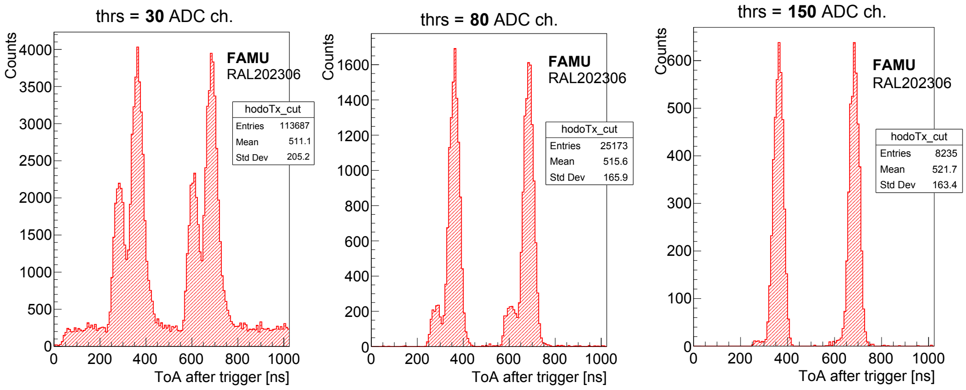

Figure 3.18: *Time of arrival for increasing values of the threshold (left to right: 30, 80, 150): the secondary peak due to decay particles is suppressed, but reducing the statistics on true events.*

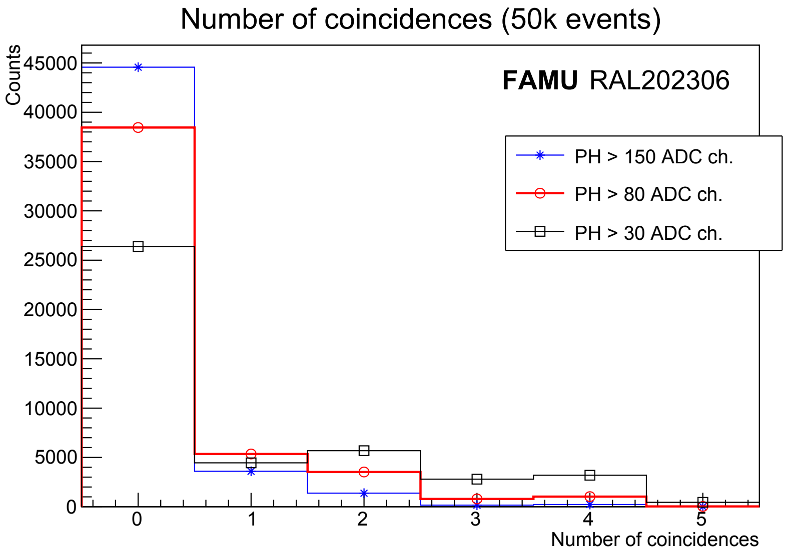

Figure 3.19: *Histograms of the number of coincidences per event as a function of the pulse height threshold. The 80 ADC channel threshold maximises the number of events classified as single events (bin* 1*), allowing to discriminate the beam muons from the background (bin* 0 *and bins* ≥ 2*), without compromising the deposited charge spectrum.*

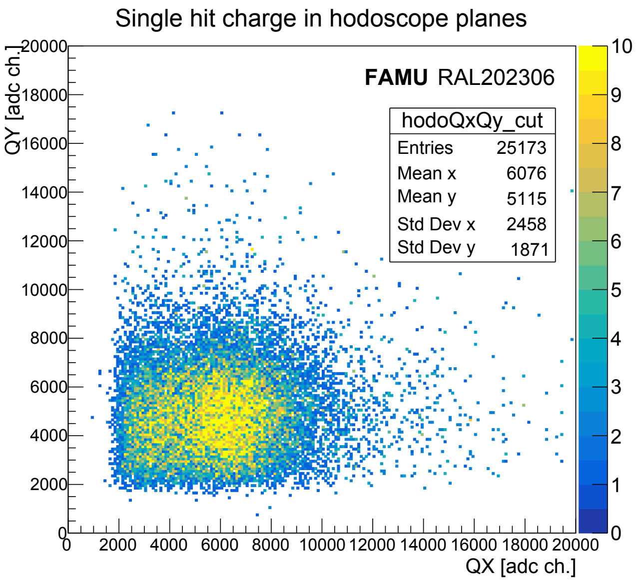

Figure 3.20: *Charge deposit in the two planes of Hodo-1 during the low-flux test beam at RAL for single particle events selected with the time coincidence data processing, with pulse height threshold at 80 ADC channels.*

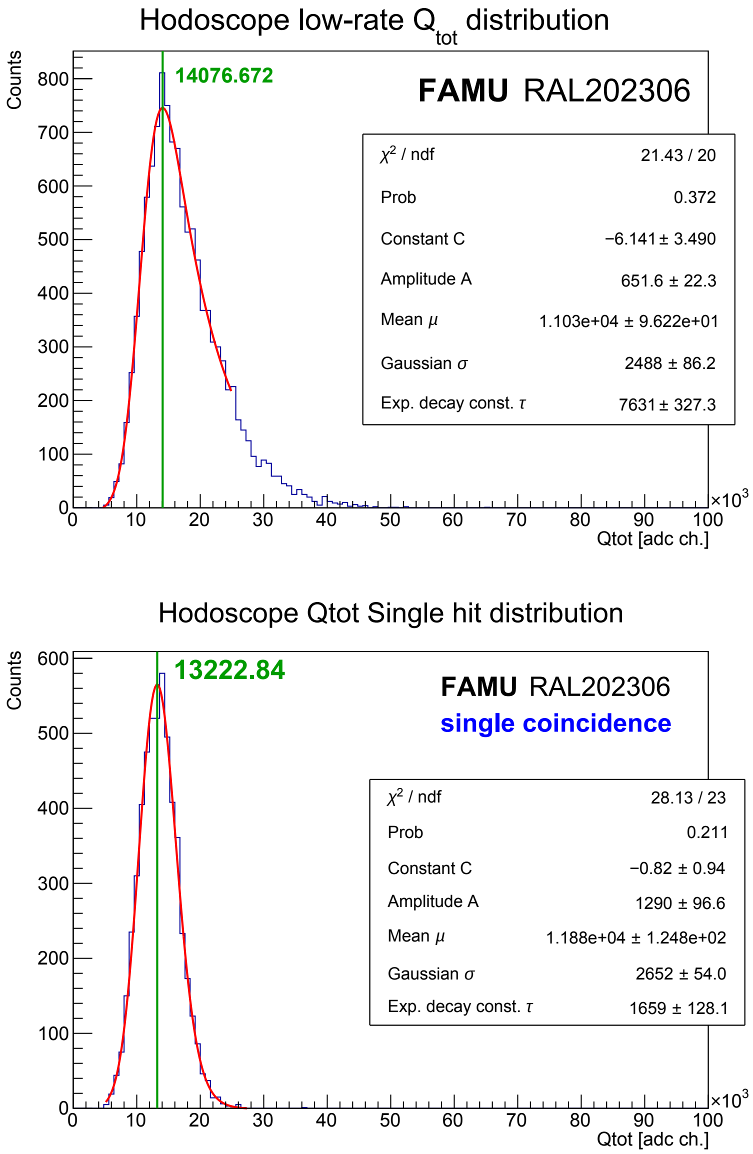

Figure 3.21: *Comparison of the fitted Q_{tot} histograms used to estimate of Q_μ using the data selected with the two coincidence method in the general case (upper) or when requiring a single-particle event (lower)[55] The second approach has been used to calculate Q_μ.*

particle interacted with the hodoscope, or a particle interacted only with one fibre. Figure 3.21 shows the final histograms of Q_{tot} fitted with model 3.3. Two versions are presented: the first one is made just by requiring that at least one time coincidence occured, while the second plot is made by imposing exactly one coincidence per event takes place. This strict condition is in this case crucial to exclude multiple-particle events, which make the distribution asymmetrical.

In order to obtain the uncertainty on the estimation of the maximum, the fit is repeated 2500 times by varying the two fit boundaries in a reasonable range. This allows to find the best region of stability for the fit, in order to optimise the estimation of the maximum. By focusing on stable regions, imposing e.g. $\chi^2/NDF < 1.2$, it is possible to use the variation of the maximum extracted from the fit to determine the uncertainty on its value. Figure 3.22 shows the 2D profile of χ^2/NDF and the fit maximum as a function of the two fit boundaries, noted as Lower and Upper Level Discrimination (LLD/ULD) thresholds, for the single coincidence case (second plot in Figure 3.21).

The resulting estimation for the average charge deposited by a muon interacting with both planes of fibres is $Q_\mu = (13220 \pm 40)$ ADC channels. This values is not to be compared to the one of Q_μ obtained in the previous Section, as they are obtained with two different detectors, with different geometry and SiPM model.

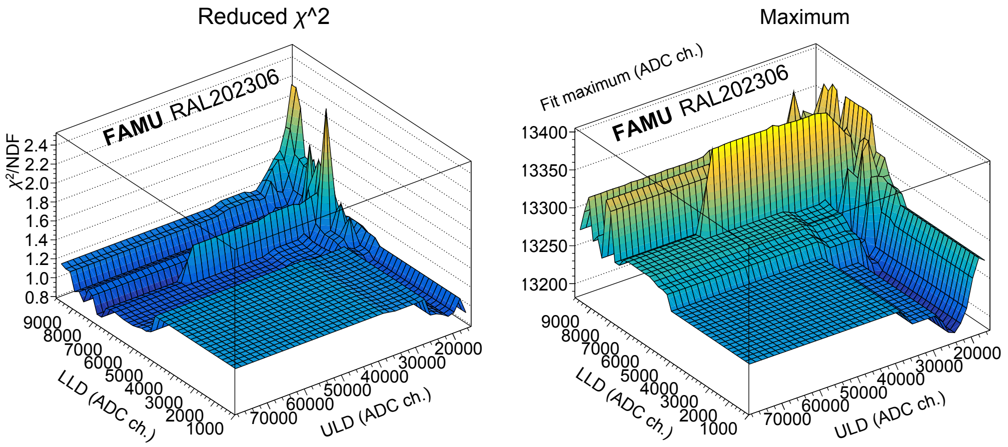

Figure 3.22: *Fit stability plots for the single coincidence processing of the test beam at RAL (left reduced χ^2, right fit maximum) as a function of the fit boundaries LLD (Lower Level Discrimination) and ULD (Upper Level Discrimination). The reduced χ^2 plot is usesful to optimise the fit range, while both and to obtain the uncertainty on Q_μ (for example by checking out the variation of the fit maximum in the region with $\chi^2/NDF < 1.2$).*

3.6 Hodoscope operation with high-flux muon beams at RAL

The use of Hodo-4, the FAMU hodoscope, as a flux-meter during previous experimental runs has then been tested using the result of Q_μ coming from coincidence data reduction and the values of W_1, W_2, η extracted from the Geant4 simulation. This procedure is also the focus of a paper about the low-flux test at RAL[55].

By fitting with a Gaussian profile the full rate beam histogram of the charge deposited in the hodoscope in each muon spill (see Figure 3.23), it is possible to extract the average value of Q_{tot} for the analysed run. However, this flux estimation can also be carried out event-by-event simply taking the value of Q_{tot} and converting it into muon flux. Taking the mean value and converting it into mean muon rate by applying Eq. 3.5, one gets $(1.25 \pm 0.03) \cdot 10^4$ muons/s. This value has been obtained with synchrotron current $\sim 85\%$ the maximum value. It is consistent with the expected order of magnitude for the 55 MeV/c negative muon flux at full synchrotron current ($> 10^4$ muons/s)[48, 49].

By extracting weighing factors for Q_μ at other momenta from the simulation, it has also been possible to estimate the muon flux during high-rate measurements at momentum different from 55 MeV/c. The result is presented in Figure 3.24 and the trend is increasing with momentum, as expected (see Section 2.3).

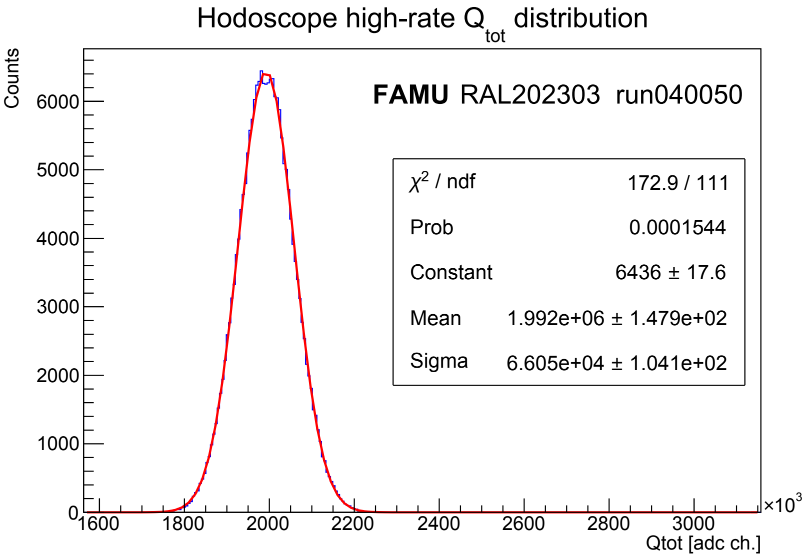

Figure 3.23: *Extraction of average Q_{tot} from the fit of a high-rate Q_{tot} histogram with a Gauss profile[55].*

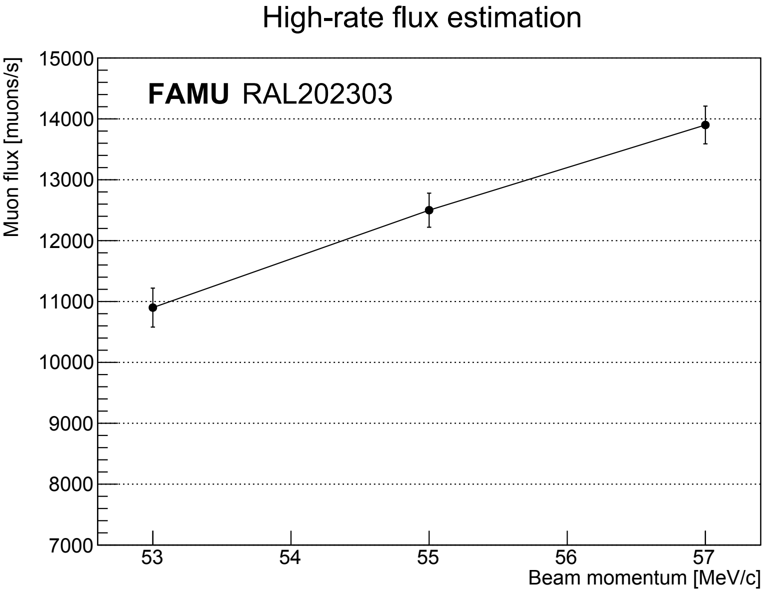

Figure 3.24: *Estimation of the muon flux at RIKEN-RAL Port1, with the beamline in the FAMU configuration, for three values of beam momentum. The correction factor for the value of* Q_μ *is extracted from the simulation[55].*

3.6.1 Hodoscope linearity and beam focusing check

The high-flux measurements are reliable only if the hodoscope operates in a linear regime, which means that Q_{tot} is linearly proportional to the muon flux. This is fundamental, as a real hodoscope will reach a saturation if the energy deposit is too high, and no estimations of flux can be obtained if the detector saturates.

To verify this, the charge deposited in the hodoscope has to be compared to a variable directly related to the number of muons entering the target. A good candidate is the number of muonic X-rays detected by the FAMU X-ray detection system. To avoid high-rate low-energy X-rays, this count was carried out considering only waveform pulses peaking over 60 keV. The saturated pulses are not included in the computation. Measurements were carried out with the full target and different values of flux were obtained through variations in the RB2 current. For each measurement, 5000 events have been acquired, and the procedure was repeated also at beam momenta 53 MeV/c and 57 MeV/c.

The resulting plots are shown in Figure 3.25. The linearity test at 55 MeV/c (central plot, red fit) proves great linearity. It was not possible to explore the linearity at higher fluxes due to flux limitation at the time of the measurement. The detector linearity is a key point in proving that the presented analysis method can be used to estimate the muon flux using linear models like Equation 3.2 and its derivates.

On the other hand, the data acquired at higher and lower momenta have

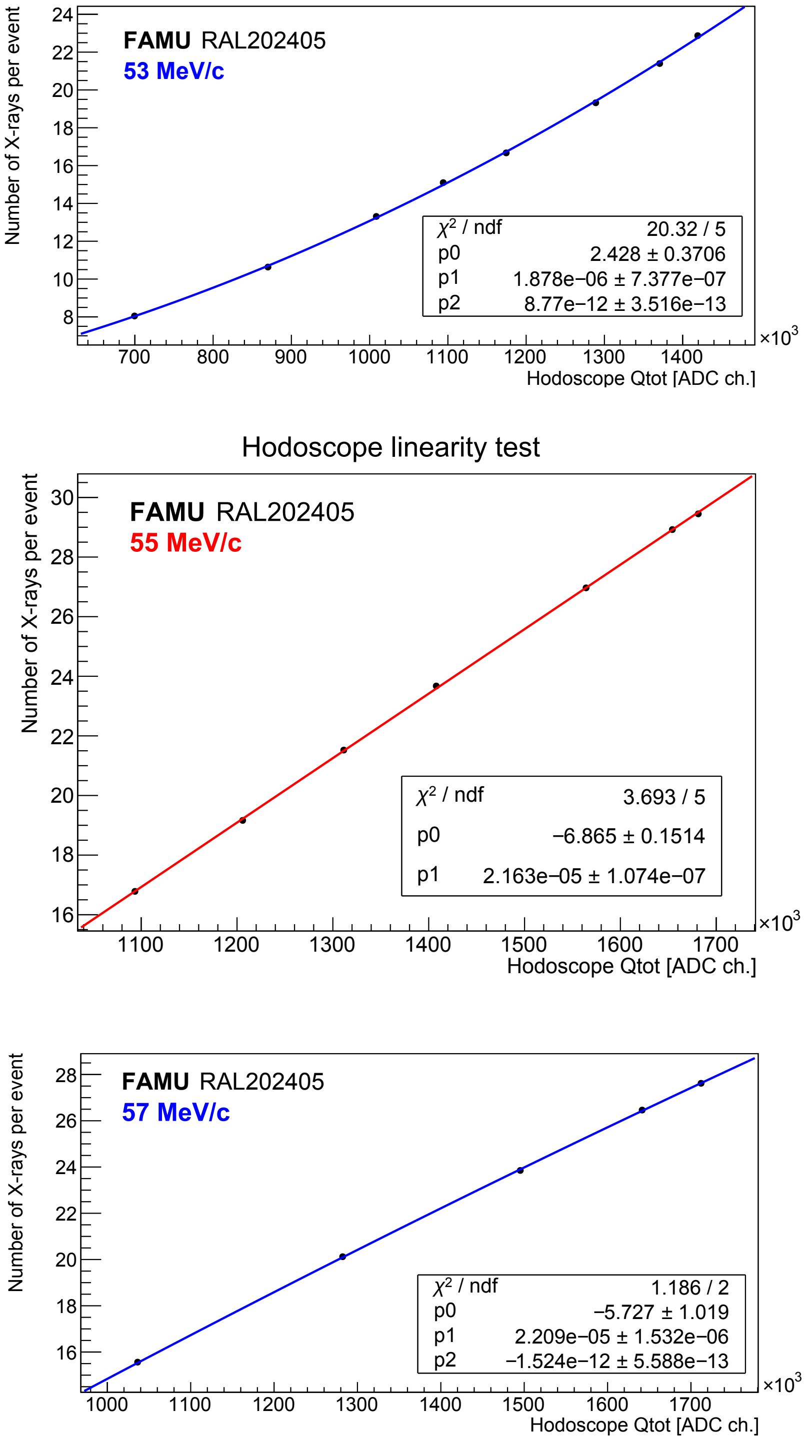

Figure 3.25: *Successful hodoscope linearity test, comparing the hodoscope* Q_{tot} *and the number of reconstructed non-saturated X-ray signals with energy over 60 keV. The latter quantity is definitely proportional to the number of muons injected in the target. Non-linearities (of opposite sign) for momenta over and below 55 MeV/c come from the fact that the beam focusing was optimised for 55 MeV/c only, the FAMU working point.*

a visible quadratic component, of opposite sign (Figure 3.25, upper and lower plot, blue fits). This is because the beam focusing is optimised for working at 55 MeV/c. In particular, as explained in Section 2.3, the quadrupole magnets RQ9, RQ10 and RQ11 have been set in order to focus the 55 MeV/c beam in the target and maximise the deposit of muons in the gas, ensuring that most muons in each bunch pass through the slit of the FAMU lead collimator, which is positioned downstream of the hodoscope. The beam focus is therefore not optimised at other values of momentum, like the ones investigated in this part of the work. When the muon flux is reduced by de-tuning the value of a bending magnet, the beam spot maximum moves to a different position on the horizontal axis. However, if the focus is optimal, the beam is mostly injected in the collimator anyways. On the other hand, if the focus is not optimised, the beam spot is a bit larger, and a variation in its symmetry results in a variation of the number of muons entering the target. An example of modification of the beam shape on the X axis as the RB2 magnet is de-tuned for this measurement is presented in Figure 3.26.

In conclusion, the FAMU beam monitor observable, Q_{tot}, is linear to the muon flux, provided that the beam focusing of the beamline is optimised. The non-linearities at $p'_\mu \neq 55$ MeV/c are due to the beam halo scraping the collimator and not reaching the hodoscope. This also confirms the quality of the beam focusing at 55 MeV/c achieved during beam commissioning.

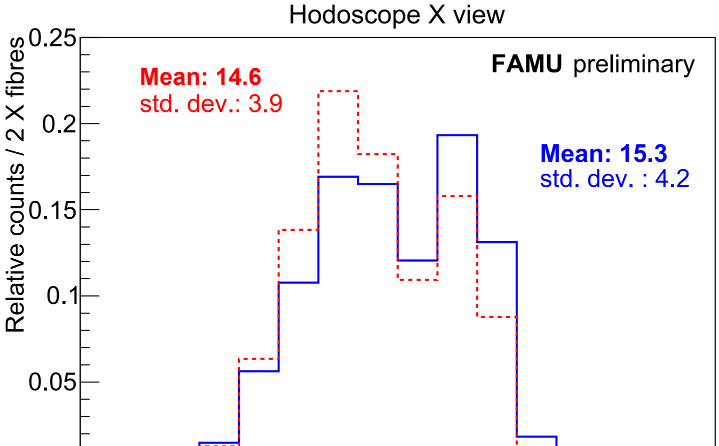

Figure 3.26: *Comparison of the shape on the X axis (horizontal) of the 55 MeV/c muon beam at Port1 between standard optimised condition (blue solid line) and the same beam tuned for the maximum beam reduction used for the hodoscope linearity test (red dashed line): the beam spot size remains fixed, whereas it becomes asymmetrical as we get away from the optimum. When the last three quadrupole magnets are not optimised, for example for the other values of momenta, such asymmetry results in a reduction of the number of muons trespassing the FAMU lead collimator, resulting in the deviations from linearity visible in Figure 3.25.*

3.7 Summary

In conclusion, among the three proposed models of 32 × 32 scintillating fibre hodoscope, Hodo-4 has been chosen as the FAMU beam monitor. The design of its active area consists of 1 mm interspaced fibres, which is the optimum between a wide detector area and small detector thickness. However, this model complicates the response function. The simulation in Geant4, supported by the one carried out in FLUKA-CERN, enabled to understand the detector response function with a low and a high flux of muons. Together with the low muon flux measurement carried out at RIKEN-RAL in December 2023, it permitted a calibration in muon flux, which enables the use of the detector as a flux-meter.

The estimated flux in the FAMU setup (Figure 3.24) is the same order of magnitude of the RIKEN maximum flux at the same momentum (Figure 2.7). The detector and operational procedures described in this chapter can be applied to other heavy particle beams, and this activity may prompt further collaboration with RIKEN-RAL and other facilities to develop a time-resolved muon beam monitor capable of 2D beam spot mapping and flux measurements.

Details on the use of this detector to normalise FAMU data over the incoming muon beam flux are reported in Section 4.3. All these considerations are valid, provided that the hodoscope reads a deposited charge linear to the true muon flux. The detector linearity was verified with by varying the flux manually with beam optics de-tuning (Figure 3.25).

Chapter 4

FAMU data analysis

This chapter outlines the workflow of the entire FAMU data analysis team, with a detailed focus on the tasks I personally carried out. Specifically, my individual tasks were the muon beam characterisation (Section 4.1.1), the X-ray detector performance (Section 4.4), and the data normalisation on muon beam intensity and gas condition (Section 4.3). I also gave contributions in the optimisation of the data selection cuts (Section 4.2.2) and in the delayed X-ray statistics estimation (Section 4.5).

4.1 FAMU data taking

Three beamtime windows were assigned to the FAMU experiment in 2023 by the scientific committees of the ISIS Neutron and Muon Source in July, October and December. Each of these data taking windows is called a *period* and it is referred to with a code *RALYYYYNN*, where YYYY is the year and NN is the period number. Each period is divided in batches, where a *batch* is the set of contiguous measurements taked with the same laser wavelength.

The first acquisition period in July 2023, RAL202303, was used for the beam, target, laser and entire setup commissioning. Therefore, no physics data acquisition was made.

The second and third period in 2023, namely *RAL202304* (October) and *RAL202305* (December), are instead the first two FAMU physics data takings. The main features of the batches in these two periods are reported in Table 4.1. The spectral region covered by these data acquisitions is shown in Figure 4.1 and compared to the latest theoretical predictions for the *hfs* wavelength. In particular, 14 wavelengths have been measured in 2023 with the required statistics (at least 21 – 22 hours of live time). The different muon flux, laser performances or live time among different measurements are then normalised and equalised as described in Section 4.3.

The data acquisition periods for 2024 with the upgraded detector setup were in July and October, named *RAL202404* and *RAL202405*, respectively.

However, the data analysis carried out in this work is only focused on 2023 data.

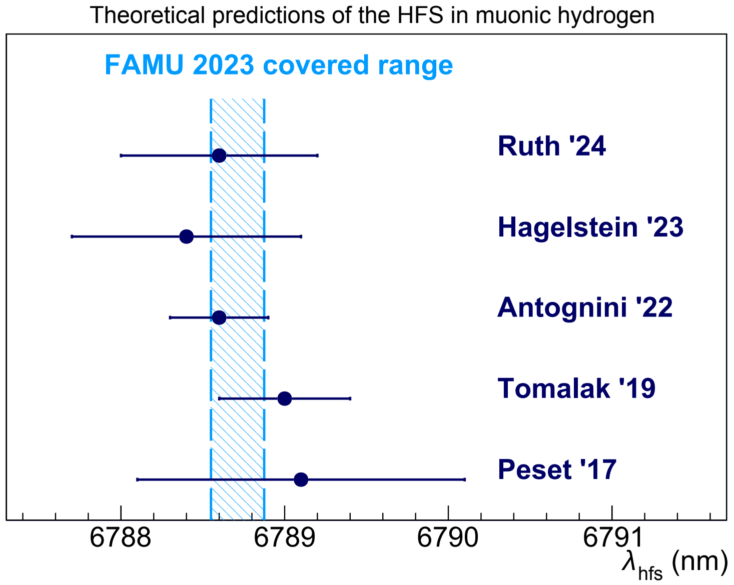

Figure 4.1: *Comparison among the latest predictions for the hfs (corresponding to the predicions for the proton Zemach radius shown in Figure 1.3) and the spectral range covered in the 2023 beamtime.*

Each detector is calibrated before every data acquisition period with radioactive sources of ^{241}Am (60 keV gamma ray), ^{133}Ba (multi-γ with main peaks at 31 keV, 81 keV, 356 keV) and ^{137}Cs (662 keV gamma ray). In this way, the standard scale for QuickLook (the routine which produces on-line plots to check whether everything is working properly) is set for all detectors and their stability through time is checked. To do so, the beam is kept off and the digitisers are set to produce trigger signals out of a detector and use these signals to trigger the whole DAQ system instead of the typical beam trigger. A particular case is represented by the germanium detector, for which the fast pre-amplified signals are used to trigger the DAQ but the spectrum is obtained from the shaped signals (see Section 2.4.4 for details on the DAQ). For optimised results, during proper data analysis any drift or variation in calibrations is followed and corrected also by looking at the prompt emission.

4.1.1 Muon beam performance

The FAMU beam hodoscope described in Chapter 3 allowed beam shape and flux monitoring during the data acquisitions. Figure 4.2 shows the variation of the estimated muon flux over the two data acquisition periods in October (RAL202304) and December 2023 (RAL202305).

Several beam magnet power supply faults were experienced during period RAL202305, specifically on RQ6 (2pm, 7 Dec.), RB3 (5pm, 11 Dec.), RQ1

Table 4.1: *Resume of RAL202304 (October 2023) and RAL202305 (December 2023) data taking periods.*

Batch ID	**Wavelength (nm)**	**Start time**	**Live time (h)**	**Live time (%)**	**Runs**	**Events**
11	6788.550	2023-10-12 09:15:18	22.1	90.2	17	3091146
13	6788.650	2023-10-13 11:02:31	22.0	80.0	16	3106954
19	6788.850	2023-10-14 16:22:03	22.6	90.9	15	3130785
21	6788.600	2023-10-15 19:19:51	22.4	92.9	16	3094365
23	6788.750	2023-10-16 20:07:39	21.3	85.2	15	2982172
29	6788.650 (II)	2023-10-18 00:56:55	5.87	83.3	4	582145

Batch ID	**Wavelength (nm)**	**Start time**	**Live time (h)**	**Live time (%)**	**Runs**	**Events**
9	6788.800	2023-12-07 17:46:10	22.5	79.5	16	3036797
11	6788.700	2023-12-08 22:17:44	23.8	54.9	16	3096532
12	6788.575	2023-12-10 18:13:27	21.7	93.1	14	2924997
14	6788.675	2023-12-11 18:19:19	22.2	92.5	14	2986890
18	6788.775	2023-12-12 22:55:26	22.8	93.1	15	2985861
20	6788.625	2023-12-14 00:12:32	22.0	75.3	15	2978204
22	6788.725	2023-12-15 05:41:00	22.1	93.2	14	2944857
24	6788.825	2023-12-16 05:56:30	22.0	78.6	15	2960087
26	6788.875	2023-12-17 10:24:28	20.0	92.6	12	2572928

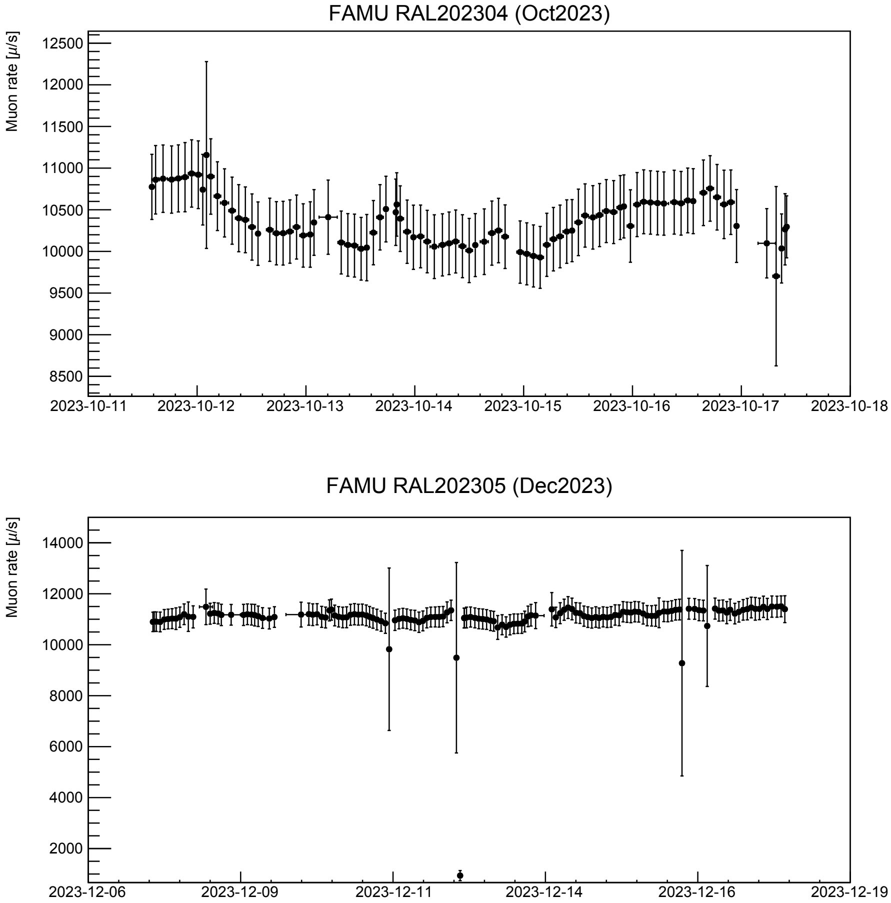

Figure 4.2: *Run-wise variation of the average muon flux during the October and December 2023 data acquisitions. The flux is measured with the FAMU beam monitor with Equation 3.5 using the value of k determined in Chapter 3. The outliers in the December data correspond to the fault of magnet power supplies discussed here.*

(10pm, 12 Dec.), RB1 (2pm, 16 Dec.) and RQ11 (1am, 17 Dec.). These faults are the outliers in muon flux visible in the second plot in Figure 4.2. In fact, these events correspond to an unoptimised beam delivery, resulting in reduced or no muon beam delivered to Port 1. RAL engineers identified a dose of neutrons higher than expected on the power supplies. The issue has been solved by further shielding the power supplies from radiation. These shieldings mitigated the number of faults experienced in later beam-times.

In addition, the beam was set to reduce the proton pulse width from 60 to 40 ns during the July 2024 run. In principle, this wouldn't cause any flux change, but some muon flux oscillations have been observed, despite the stable synchrotron current. The preliminary results of the first tests on this data acquisition, presented in Figure 4.3 show that these oscillations appear to be correlated to the drifts of the proton pulse width. The full data analysis is still ongoing and further measurements and models are being proposed to verify and try to explain this behaviour. However, the matching information from the hodoscope and the number of detected X-rays proves once again that the former is a good beam monitor.

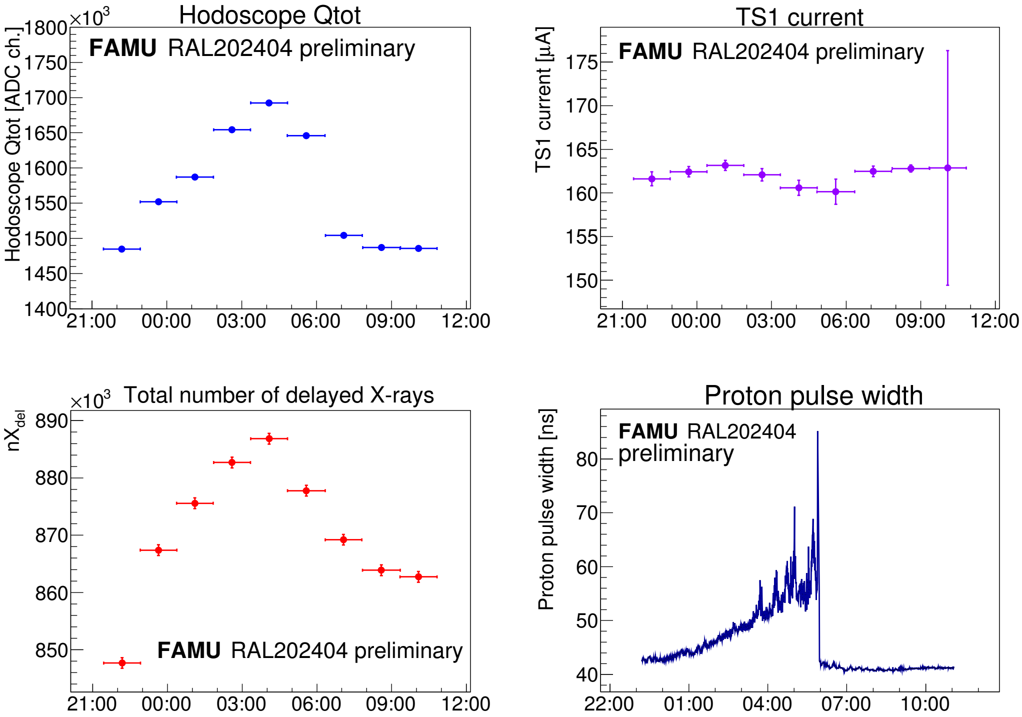

Figure 4.3: *One of the oscillations in hodoscope Q_{tot} (top left) observed in July 2024. The related oscillation in number of delayes X-rays (bottom left) and the absence of oscillations in TS1 current (top right) prove that the muon flux oscillation is real and not related to the proton production. However, this behaviour appears related to drifts in the proton pulse width (bottom right).*

4.1.2 Laser beam performance

The histogram of the laser wavelengths measured during 2023 is shown in Figure 4.4. The histogram is made with the instantaneous value of wavelength saved for each event. It is important to notice that narrower and more regular peaks are visible for December. This is thanks to an automatic wavelength keeper which was added to the laser software to automatise part of the shifters' work and optimise the laser stability.

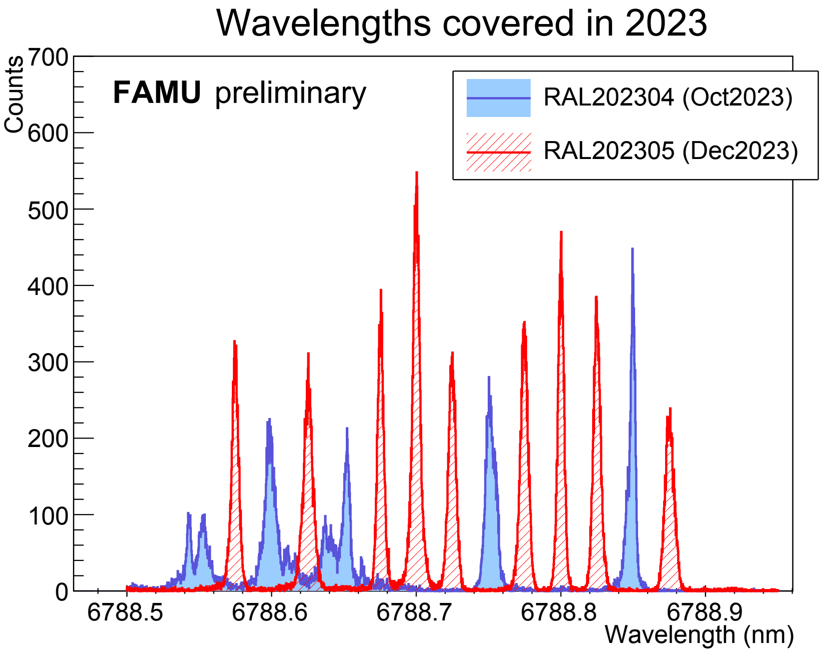

Figure 4.4: *Histogram of the wavelengths measured in 2023 by the FAMU experiment. Courtesy of M. Baruzzo.*

A typical distribution of the energy delivered by each laser pulse is shown in Figure 4.5. It is important to notice that the transition probability is proportional to the laser energy (as it is proportional to the number of photons interacting with the μH atoms). For this reason, it is important to take this distribution into account for data selection and to normalise events happening at different energy. In addition, the system is not capable of delivering the same energy for every wavelength, and it is therefore important to take into account of this variation among different batches for data normalisation.

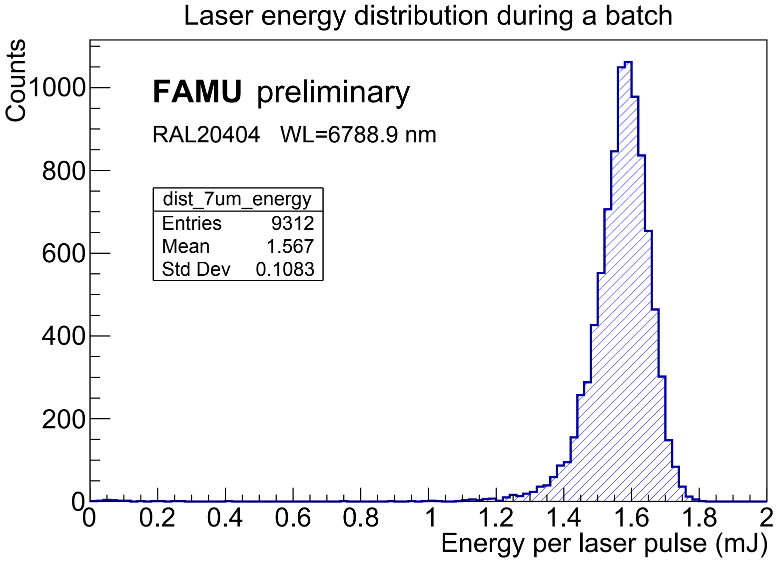

Figure 4.5: *Example of energy distribution during a batch of data acquisition with fixed wavelength. Courtesy of M. Baruzzo.*

4.2 Data analysis workflow

The data analysis for the FAMU experiment starts from the raw or first-level data described in Section 2.4.4 and saved by the data acquisition software in .root format. The software writes a *file* every 400 events, and 500 files (i.e. 200k events) form a *run*.

At this point, data processing is carried out on-line through a program called FAMUAnalysis which runs on all raw files producing the so-called *second-level files*. This phase of the analysis process is mostly focused on:

- extracting the value of hodoscope Q_{tot} and the beam XY profile for each event;

- extracting the time and pulse height of every peak in the waveform for all 35 detectors.

Lastly, another piece of software called QuickLook runs on the level 2 files to extract some preliminary plots useful for on-line monitoring of the setup. These plots, which are clearly not intended to substitute the full off-line analysis, are made available shortly after the related raw file is saved, thanks to the FAMU on-line data processing. The whole data analysis workflow is reported in this Section. Specifically, this procedure for data processing is well described in the following subsection (4.2.1), whereas the actual analysis workflow on these data (from the single X-rays to the final resonance plot) is described in subsection 4.2.2.

4.2.1 On-line data processing: level 2 data and QuickLook

As already mentioned, FAMUAnalysis is a custom software written in C++ and ROOT, which handles the raw files to perform the on-line data processing and writes the level 2 files. This data processing, however, can also be carried out off-line in case re-processing is needed after fine tuning of the code, or if a modified version of the software is needed for some specific analysis items.

Hodoscope on-line analysis

For every event, FAMUAnalysis calculates the integral over a threshold (in order to avoid small baseline fluctuations) of the waveform for each channel of the hodoscope, as already mentioned in Sections 3.2 and 3.6. The integration is carried out on raw data by summing the height of every point over threshold, no further algorithms are applied to smooth or fit the waveforms. Figure 4.6 shows an example of waveform from a channel of the hodoscope, with the integral marked in red. For each fibre, the value of integral is saved as Q^{Xi}_{fib} on the X plane and Q^{Yi}_{fib} on the Y plane, with $i = 1, ..., 32$. The 64 contributions are then also summed to obtain

$$Q_{tot} = \sum_{i=1}^{32} \left(Q^{Xi}_{fib} + Q^{Yi}_{fib} \right) . \tag{4.1}$$

Figure 4.7 shows the output of QuickLook of hodoscope data, i.e. the histogram of Q_{tot}, the plot of Q^{Xi}_{fib} and Q^{Yi}_{fib} as a function of the fibre number i. In addition, a 2D superposition of the two latter plots is produced, in order to help visualising the beam shape. This is not to be compared to the actual beam shape that can be measured with low flux (Figure 3.13), as it can only be obtained by imposing coincidences, which is not possible at high flux as in normal FAMU operation.

Channel X-16 is visibly not working in Figure 4.7. All connections have been tested and no issues were found. A direct test on the IV curve of the SiPM, which would allow to check if it's working, is not possible in this configuration, as 8 SiPMs are biased with the same LEMO connector. Another possible reason for this falure might be a deterioration in the optical coupling between the SiPM and the fibre, or a damage in the scintillating fibre itself. In order to address this issue, the detector should be opened and inspected, which could damage other channels. In addition, the detector commissioning and calibration have been carried out while this channel was already in these conditions. For all these reasons, it has been decided not to attempt a hardware fix on this damaged channel.

X-ray detectors on-line analysis

Regarding the X-ray detectors, they are treated differently by FAMUAnalysis as their aim is to extract all the possible X-rays detected during an event.

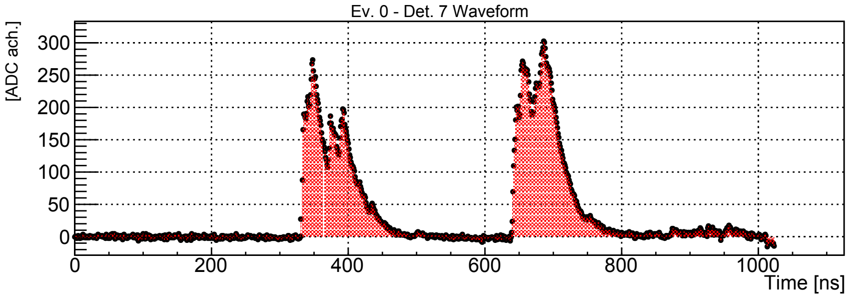

Figure 4.6: *Example of waveform from a channel of the hodoscope corresponding to a fibre immersed in the beam. The double-bunch structure of each spill is clearly visible in the waveform. FAMUAnalysis performs signal integration extracting the value of Q_i for each fibre, corresponding to the red area, which is then used to compute Q_{tot} with Equation 4.1.*

FAMUAnalysis runs on the waveforms looking for peaks and it extracts useful information such as the initial, peak and final time, the pulse height (proportional to the energy released in the crystal), along with general parameters such as the baseline level and oscillation. The point-by-point derivative (calculated with ROOT) is used to extract the pulse parameter for both efficiency and computational reasons. For illustration purposes, detector LaBr4 is taken for reference in this section and the following one.

Figure 4.8 shows a pulse in a detector recognised by FAMUAnalysis: the waveform derivative is calculated (lower plot) and it is used to compute the main features of the pulse: initial time (first line, green), peak time (second line, blue), final time (third line, red), and hence the pulse height in correspondance to the peak. FAMUAnalysis is also good at recognising pulses affected by pile-up, as one can see in Figure 4.9: the first pulse is considered ended and the second one starts whenever the derivative starts increasing after a decrease (enabling not only pile-up on signal tails, as the one shown in the current plot, but also pile-up on the rises, quite common for prompt X-rays). The pulse height is extracted from an extrapolation of the first pulse shape. FAMUAnalysis returns a data structure for each recognised pulse which contains all the important information needed for data analysis. In addition, FAMUAnalysis also returns a binary flag with four digits: $f = \texttt{SUOP}$, where `S` is to mark saturated pulses, `U` is for unresolved pulses, `O` for pulses growing over an unresolved signal and `P` for signals deconvolved from a pile-up from one or more preceeding signals ($1 = \text{yes}, 2 = \text{no}$). The higher the value of this flag, the lower the reliability of the pulse parameters extracted by FAMUAnalysis.

During data acquisition, the QuickLook tool collects the pulses from the level 2 file and makes some quick plots useful to check the condition of the detectors. For example, the time and energy distribution of the reconstructed X-rays are plotted for every detector, as shown for example in Figure 4.10. These plots are clearly dominated by prompt emission and therefore the oxygen

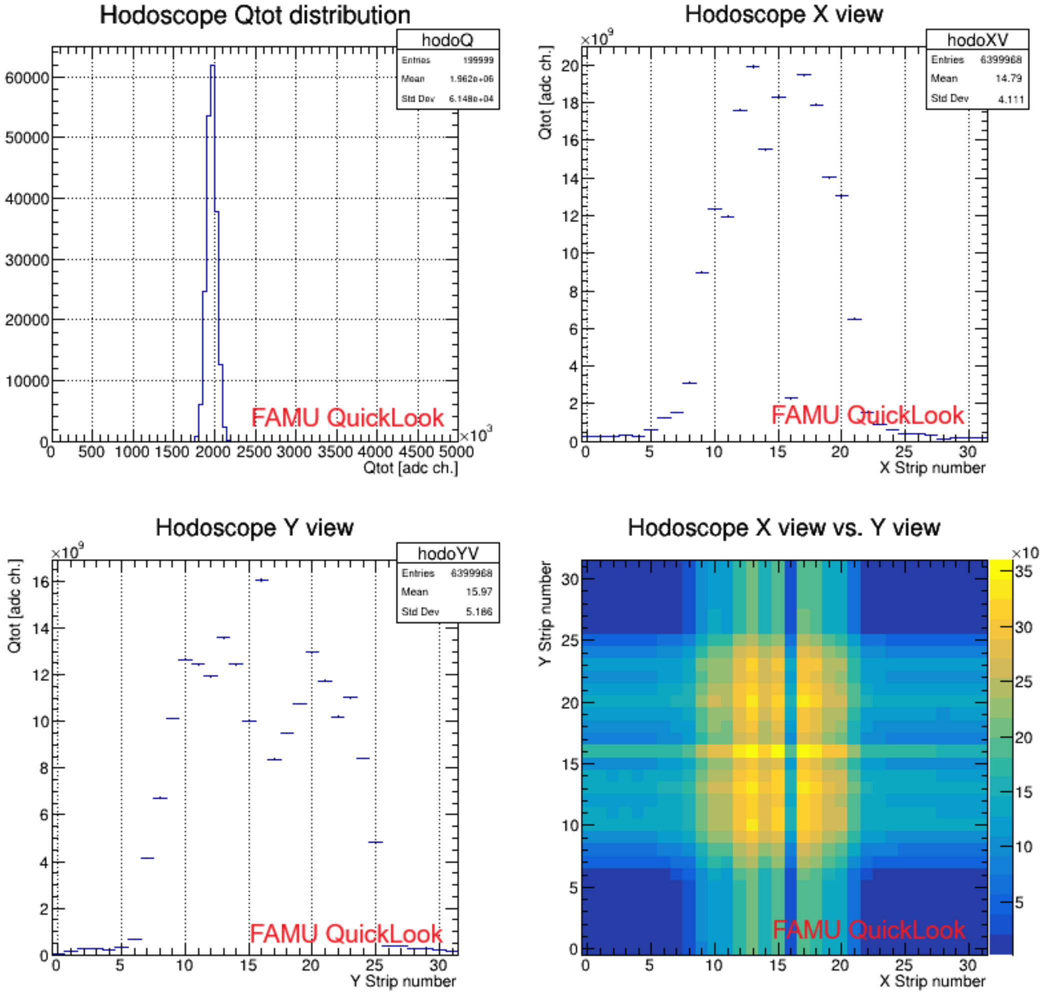

Figure 4.7: *Plots produced by the QuickLook on the hodoscope main features: the Q_{tot} histogram, the Q_{fibre} histograms on the X and Y axes and their combination for beam visualisation. The latter is not to be intended as a beam heatmap as it is not obtained by requiring coincidences (as, for example, Figure 3.13), because the high flux does not allow single particle discrimination. Channel X-16 is visibly not working.*

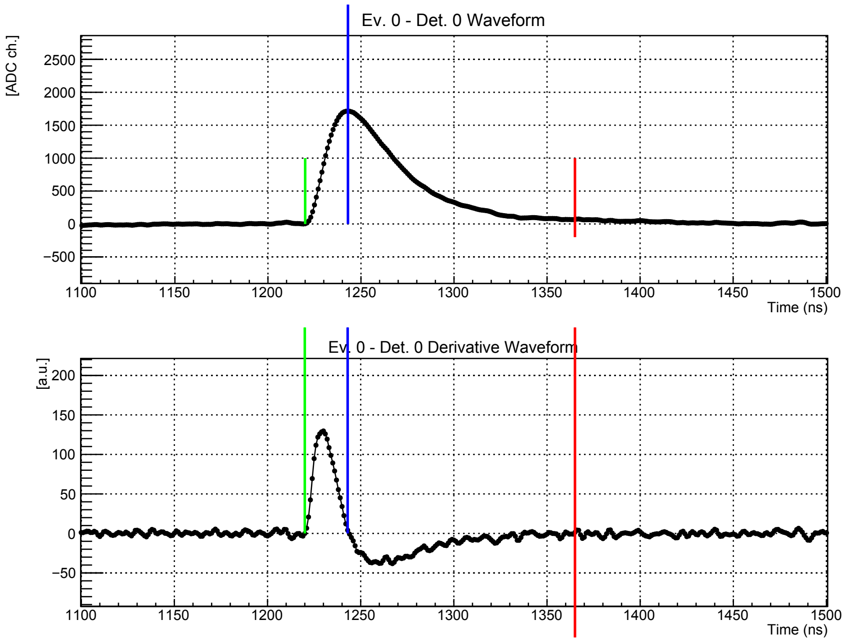

Figure 4.8: *A pulse measured by a detector: upper plot is the waveform, lower is its derivative. Optimised thresholds on the derivative are used to detect when a pulse is starting, reaching the peak point and ending. Three coloured lines mark the start, peak and stop of this pulse (green, blue and red, respectively).*

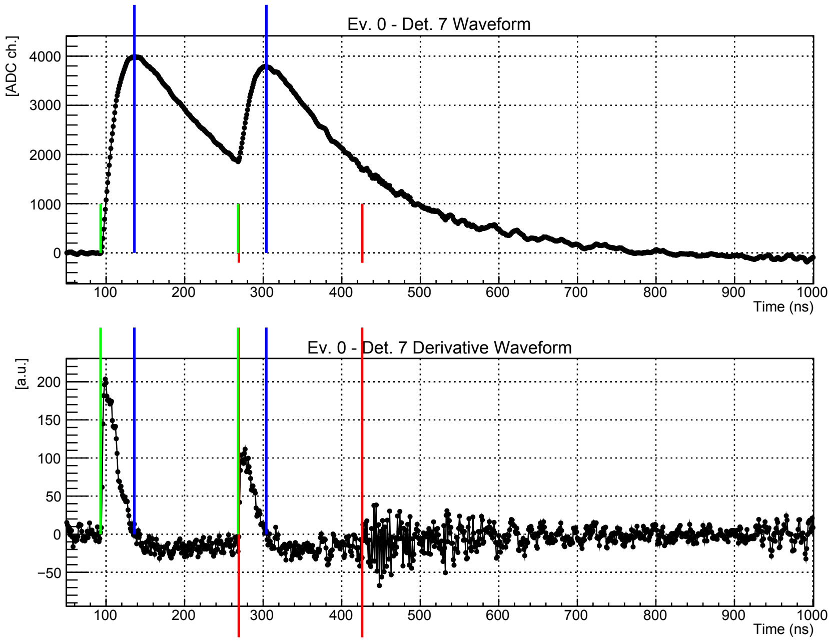

Figure 4.9: *Two pile-up pulses de-convolved by FAMUAnalysis and recognised as separate pulses. However, a flag is returned to mark the fact that the parameters extracted for the second pulse are deconvolved from pile up and might be affected by bigger uncertainties.*

peaks are not directly visible and require data selection, which is being carried out during off-line data analysis, as explained in Section 4.2.2.

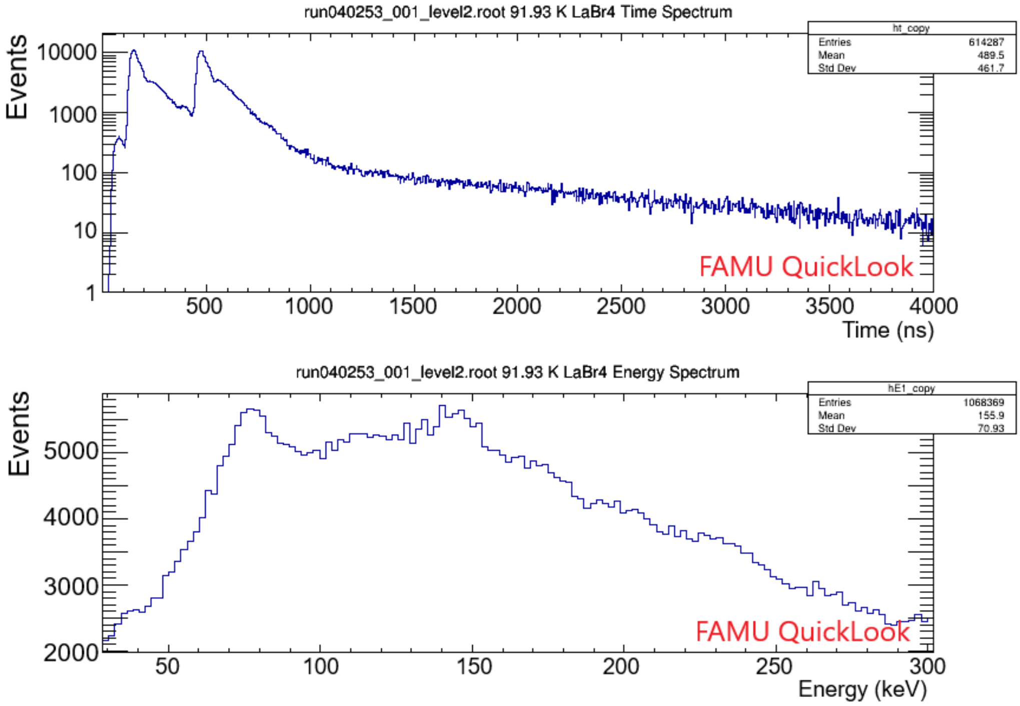

Figure 4.10: *Plots produced by the QuickLook for a typical detector (LaBr4): the upper is the time occurrencies of the X-rays in the range 0 – 1600 ns and the lower is the raw energy spectrum in a broad area (30 – 300 keV) around the region of interest.*

4.2.2 Off-line level 2 data analysis

The off-line data analysis is a key part for the experiment as it allows to select the information contained in level 2 files to extract detector performance and the data required to construct the plot of the signal as a function of the laser wavelength (illustrated in Figure 2.2). In this section, the path between the level 2 files and the final resonance plot is followed using detector LaBr4 for reference. The analysis of detector features and performances has led to further optimisation in the methods and thresholds of FAMUAnalysis, and it sometimes resulted in requiring an *a posteriori* data reprocessing to extract more reliable level 2 datasets. In fact, the spectra acquired for each detector can't be used as-they-are, as they contain much information which can be extracted only by skimming the data, i.e. imposing condition on some parameters. The correlation plot between energy and time of arrival of X-rays for LaBr4 is shown in Figure 4.11, where the two muon beam bunches (approximately at $t_s = 150$ ns and $t_s = 480$ ns) are clearly visible as they are correlated to enhanced production of X-rays on all the measured range of energies, whereas the delayed signals ($t_s \gtrsim 800$ ns) are mostly at low energies (50 – 300 keV). For example, the prompt X-ray plot extracted with proper data selection from the raw one, is shown in Figure 4.12.

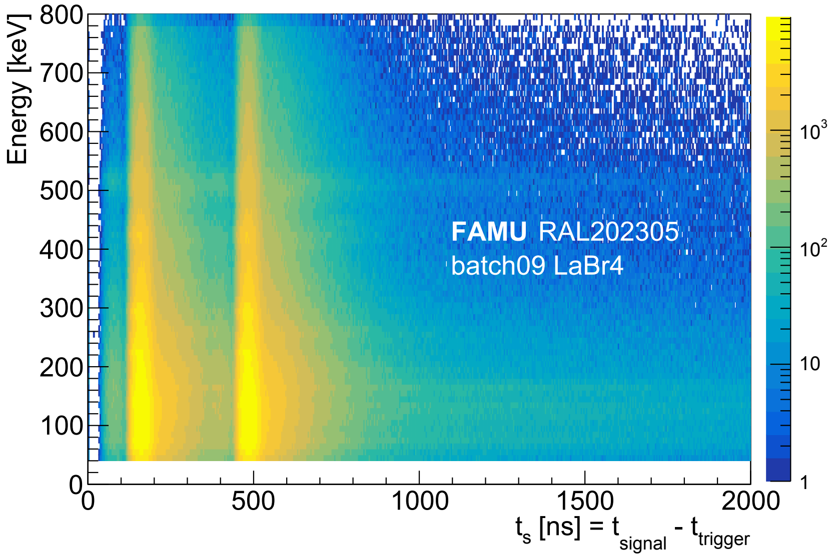

Figure 4.11: *Correlation plot between the time of arrival and the energy of reconstructed X-rays for LaBr4in RAL202305, obtained without cuts. Most signals belong to the prompt region, i.e. the time around the two muon pulses (arriving at around 150 and 480 ns in this plot). Most delayed signals ($t_s \gtrsim 800$ ns) have energy below 300 ns and are emitted by the gas.*

Clearly, a crucial phase of off-line analysis is data skimming, i.e. the introduction of cuts and selection on data in order to clean the spectra and optimise the signal-to-noise ratio. Some general cuts applied to the detectors

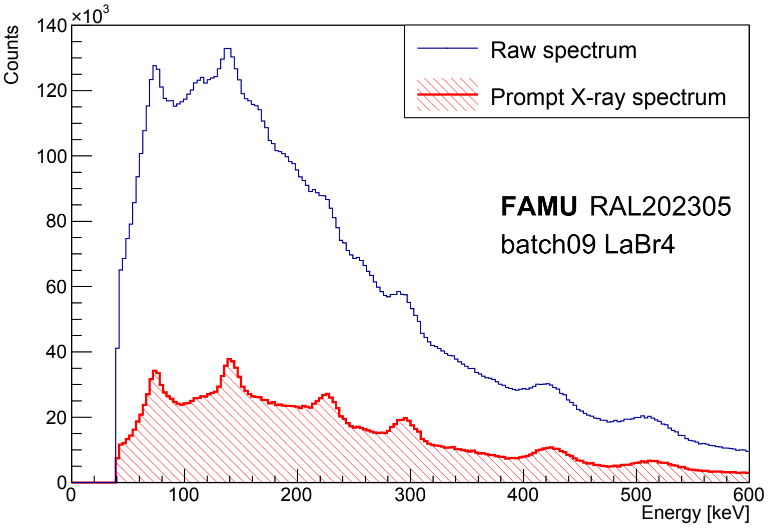

Figure 4.12: *The comparison between the raw energy spectrum and the one obtained with standard selection and prompt timing selection shows the importance of the cuts in optimising the signal-to-noise ratio.*

to carry out data skimming are on the reconstruction flag f, the time since the previous pulse on the same detector (Δt) and the baseline mean (bsl) and root mean square (RMS_{bsl}) of the detector in the current event. The optimised value for the reconstruction flag is $f < 10$ to exclude saturation, unresolved signals or signals growing over unresolved signals. This selection allows signals from pile-up reconstruction, but it is important to avoid pile-up on the rise when the two pulses are too close because the pulse height reconstruction is not reliable. For this reason, $\Delta t > 30$ ns is generally imposed for delayed signals on LaBr detectors and $\Delta t > 100$ ns for 1″-MIB detectors, as the latter have longer rises and tails. On the other hand, pile-up is totally avoided for prompt signals imposing $f = 0$. In addition, outliers for the baseline are considered anomalies to be rejected, by imposing $|bsl| < 10$ and $RMS_{bsl} < 20$. For this study, detector LaBr4 is shown in this Section as an example. The cuts imposed to this detector, hereby called the *standard set of cuts* for the experiment, are shown in Figure 4.13. The standard set of cuts is also resumed in Table 4.2. At the moment, the standard set of cuts for ½″-MIB detectors is still undergoing optimisation, for this reason this class of detectors has not been considered in this work.

The prompt X-ray spectrum (Figure 4.14) is used to check detector performances over time and to keep track the energy calibration drifts. For this reason, a fine calibration is applied for every run based on the prompt X-rays. The flag cut is made stricter ($f = 0$) to have optimal energy resolution, and the prompt timing cut has been applied: $t \in [120\text{ ns}, 220\text{ ns}] \cap [450\text{ ns}, 550\text{ ns}]$. The prompt peaks observed are the following, with the corresponding atoms responsible for the emission: 75 keV (μC), 141 keV (μAg), 210 keV & 230 keV

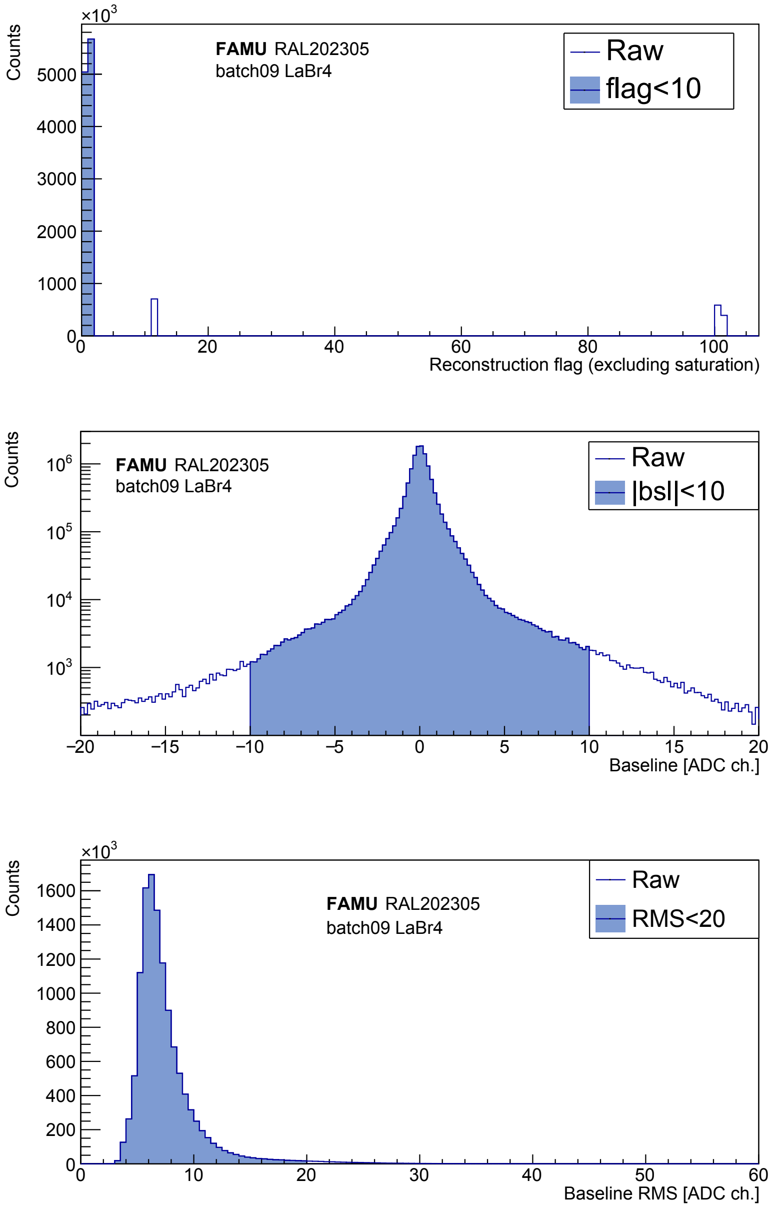

Figure 4.13: *Signal cuts on LaBr4 detector: signal reconstruction flag (required $f < 10$ i.e. no saturation, unresolved or over-unresolved signals), time since previous pulse ($\Delta_t > 30ns$), baseline average level ($|bsl| < 10$) and baseline oscillation ($RMS_{bsl} < 20$).*

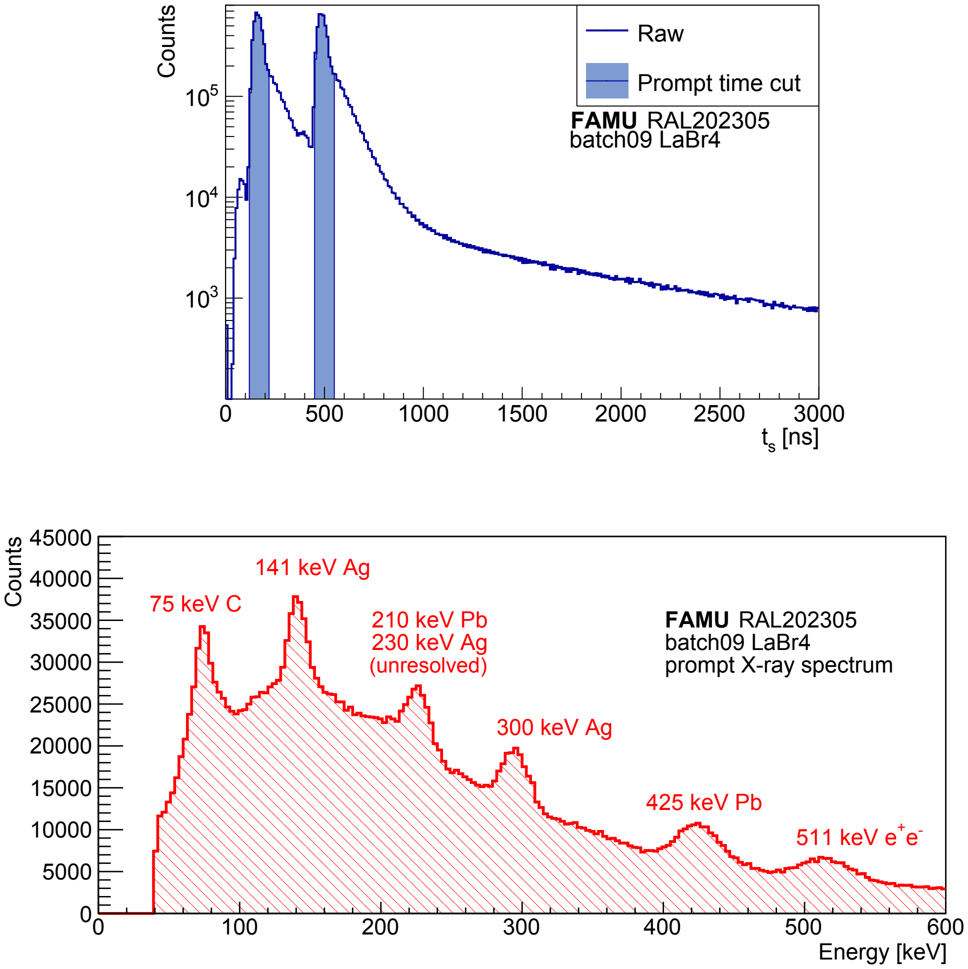

Figure 4.14: *Time cuts on LaBr4 to extract prompt signals ($t \in [120\ ns, 220\ ns] \cap [450\ ns, 550\ ns]$) and resulting energy spectrum in RAL202305 batch09 with marked peaks. The unresolved 210 – 230 keV peaks have not been used for calibration.*

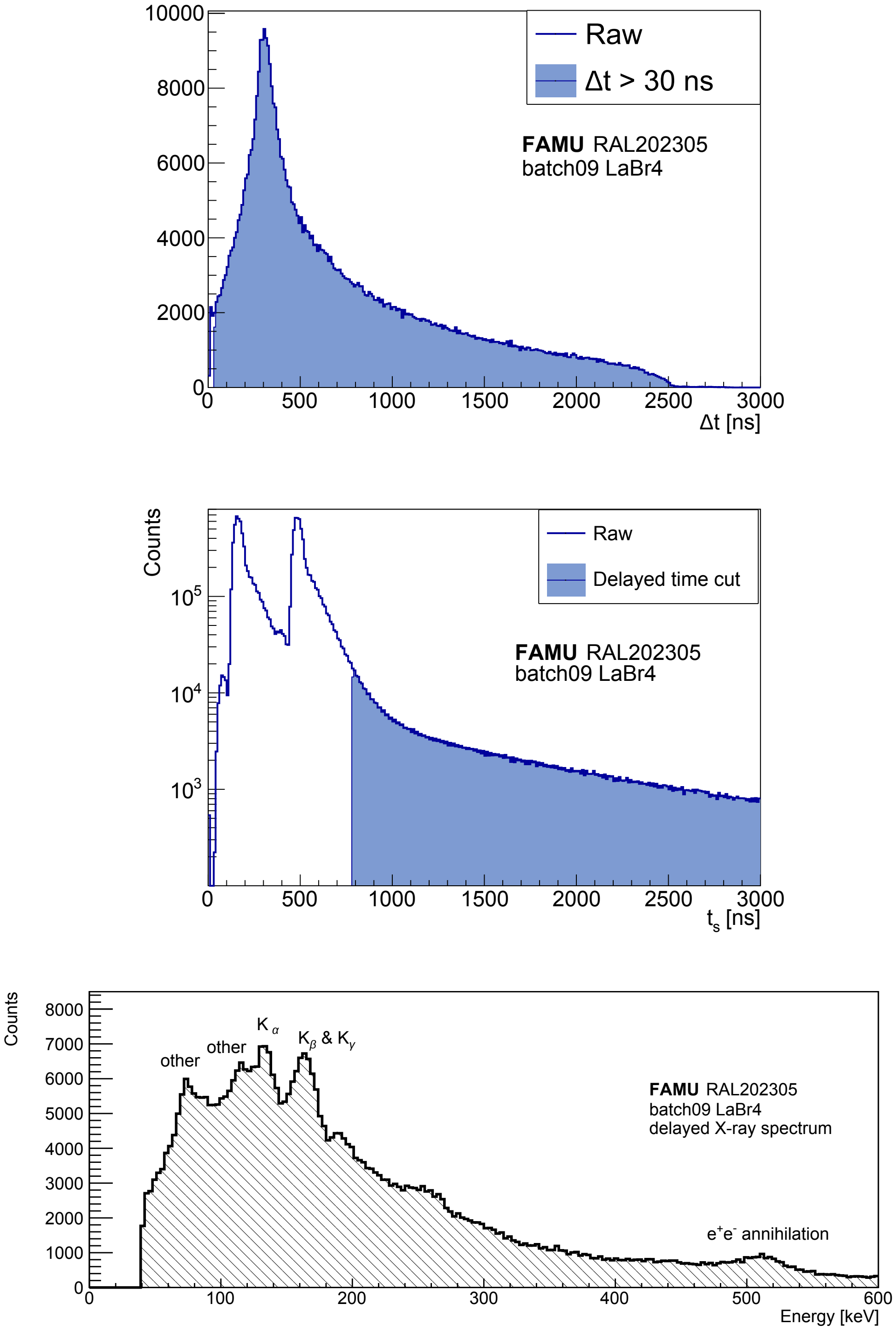

Figure 4.15: *Time cuts on LaBr4 to extract delayed signals ($t \in [780\ ns, 3000\ ns]$ ns) and resulting energy spectrum in RAL202305. The cut on the time since the previous signal has very little impact (see first plot). The peak in the Δ_t distribution at 300 ns corresponds to the time difference between the lower bound of the time cut (780 ns) and the centroid of the second muon beam bunch (480 ns).*

Table 4.2: *Standard set of cuts for X-ray data skimming for LaBr and 1″ MIB detectors. The reconstruction flag is a binary number with four digits* f = `SUOP` *where* `S` *=saturated,* `U` *=unresolved,* `O` *=over an unresolved pulse and* `P` *=pile-up (*1 *=yes,* 0 *=no). Data selection for ½″ detectors is still under study.*

Param.	Description	Prompt cut	Delayed cut
f	Reconstruction flag	$f = 0$	$f < 10$
bsl	Event baseline avg.	$\lvert bsl \rvert < 10$	$\lvert bsl \rvert < 10$
RMS_{bsl}	Event baseline RMS	$RMS_{bsl} < 10$	$RMS_{bsl} < 10$
E	Calibrated energy	$E > 40$ keV	$E > 40$ keV
Δt	Since previous pulse		$\Delta t > 30$ ns LaBr $\Delta t > 100$ ns MIB
t_s	Time after trigger	$t \in [120, 220]$ $\cap[450, 550]$ (ns)	$t \in [780, 3000]$ (ns)

(μPb and μAg, not used for calibration as they are generally merged into one broad peak), 300 keV (μAg), 430 keV (μPb), and 511 keV (e^+e^- annihilation).

The delayed X-ray spectrum (Figure 4.15), instead, is the one used to extract the signal described in Section 2.1, i.e. the difference between the number of delayed μO X-ray with the laser pulse and the one without the laser pulse. For this plot, the time requirement is $t \in [780 \text{ ns}, 3000 \text{ ns}]$. Looking at the spectrum structures, the delayed region shows two main peaks corresponding to the μO $K_\alpha = 133$ keV, and the unresolved contribution from μO $K_\beta = 158$ keV and $K_\gamma = 167$ keV. Two more peaks, one at $\sim$ 80 keV and the other one at $\sim$ 120 keV, are observed (marked as *other* in Figure 4.15). These peaks were not present in the data taken with previous versions of the target, which had no lead and no silver. The exact processes causing these emissions are currently being investigated, but they are probably due to the presence of these materials in the final FAMU target.

As the laser is injected in the chamber every other muon beam spill, half of the events in Figure 4.15 have the laser on and half of them have the laser off. This dataset is therefore divided in two sub-datasets laser (L) and no-laser (nL), and the signal is represented by the number of μO X-rays in the spectrum obtained by subtracting the background no-laser to the spectrum with laser ($L - nL$). However, before performing this subtraction it is important to notice that any excess would have to be carefully evaluated not only as a function of the laser wavelength, but also taking in consideration some other factors. For example, the laser energy delivered in each pulse is proportional to the number of photons and therefore to the probability of excitation. In addition, the number of muons delivered to the target needs to be monitored, and potentially corrected for, as it is proportional to the number of target μH atoms for the laser, which is also proportional to the amount of gas in the target, which might change during the data taking. These studies and the related corrections are thoroughly described in the following Section 4.3, whereas some steps towards the final resonance plot and the state of the art are presented in Section 4.5.

4.3 Data normalisation

This section is focused on the data normalisation tasks for the FAMU experiment. In particular, the focus of this Chapter is the normalisation on the incoming muon flux (thanks to the FAMU hodoscope) and the gaseous target conditions. The idea behind this normalisation is to find the time-dependent expression of two weights to correct the signal for the flux ($w_{Q_{tot}}$) and gas conditions (w_{PT}), as follows:

$$N_X \;\longmapsto\; N'_X = w_{Q_{tot}}\; w_{PT}\; N_X. \tag{4.2}$$

Much work is being carried out also in the normalisation on the laser energy and wavelength, as mentioned also in Section 4.1.2.

4.3.1 Muon beam normalisation

The muon beam flux is related to the number of μH atoms produced in the target and it is therefore proportional to the measured effect.

In order to find a good variable for beam normalisation, it is important to verify correlations among three levels of information:

- the synchrotron current delivered to the TS1 branch (`TS1`) and the current delivered to the muon production target (`MuC`) gives information about the proton flux delivered to the muon production target;
- the hodoscope deposited charge per trigger (Q_{tot}) is proportional to the muon flux transported by the RIKEN facility and delivered to the FAMU setup;
- the number of prompt (`nXpro`) and delayed (`nXdel`) X-rays give information about the number of muonic atoms formed in the target, and therefore the amount of muons entering the target window and stopping in its volume.

In order to perform a solid beam normalisation, it is important to verify the correlation among these variables and identify a good variable to normalise on. The main candidate for normalisation is the hodoscope reading (Q_{tot}).

During the October 2023 experimental run (RAL202304), the beam turned out to be stable (in terms of TS1 current, hodoscope Q_{tot}, number of X-rays).

On the other hand, multiple RIKEN magnets fault happened during the December 2023 run (RAL202305), as already mentioned in Section 4.1.1. In particular, the faults that took place are: RQ6 (2pm, 7 Dec.), RB3 (5pm, 11 Dec.), RQ1 (10pm, 12 Dec.), RB1 (2pm, 16 Dec.), RQ11 (1am, 17 Dec.). During each of these faults, the power supply of a beamline magnet tripped due to radiation damage, resulting in a sudden decrease of the muon flux. As a consequence, these data present some outliers in the muon flux and they are interesting to test correlations among variables.

For this reason, the plots reported in this Section are referred to the December 2023 experimental run (RAL202305).

Figure 4.16 shows the comparison between `TS1` and Q_{tot}. Each point corresponds to an acquisition run (200k events, corresponding to 4000 seconds of full rate beam). The outliers in the Q_{tot} plot correspond to the faults in the RIKEN-RAL beamline, and they are therefore not expected to appear in the `TS1` plot. In fact, the outliers are not present in `TS1` and still appear in the Q_{tot}/`TS1` ratio. For this reason, Q_{tot} is expected to be a better variable for normalisation and data selection. However, it is important to check for a correlation between Q_{tot} and the actual number of muons per spill injected in the target.

To do so, Q_{tot} is compared to the number of prompt X-rays per event (`nXpro`) in Figure 4.17. In this case, the outliers are present also in the number of prompt X-rays per trigger. Furthermore, the outliers have compatible `nXpro`/Q_{tot} ratio as normal beam. This suggests that the hodoscope flux reading is proportional to the number of muons actually interacting with the target.

As a consequence, it has been chosen to normalise linearly over the oscillations of Q_{tot}. The next step is to decide if the correction should be applied event-by-event or run-by-run. In fact, the value of Q_{tot} oscillates for every event (spill) as one can see in Figure 3.23. However, it is important to understand if this oscillation is physical or not, i.e. if it actually corresponds to an event-by-event oscillation of flux or if it is due to the hodoscope resolution. Figure 4.18 is carried out by comparing event-by-event the number of X-rays counted by one detector (LaBr4) and the value of Q_{tot} in the range of its oscillation. There is no apparent correlation, which suggests that this oscillation is not physical but due to the detector resolution. For this reason, it has been decided to apply a run-wise correction factor based on the run-wise mean of Q_{tot}, as follows:

$$w_{Q_{tot}} = Q_0/Q_{tot}^{avg}, \tag{4.3}$$

where Q_0 is a potentially arbitrary value, constant during all data acquisitions. The value $Q_0 = 2 \cdot 10^6$ ADC ch. was chosen in order to have a correction factor close to 1 in order to keep the physical meaning of N'_X as net number of laser-induced delayed μO X-rays.

4.3.2 Gas condition normalisation

The gas target is featured with a pressure sensor and two temperature sensors to monitor its conditions during the preparation for beamtime and throughout the experimental phase. In particular, assuming that the ideal gas law holds ($PV = nRT$, with pressure P, volume V, temperature T, gas constant R and amount of substance n), an ideal sealed gas container would have $P/T = nR/V =$ constant. To verify if this is true, or to evaluate the effect of potential gas losses, the variation of P/T has been studied during all data acquisition periods.

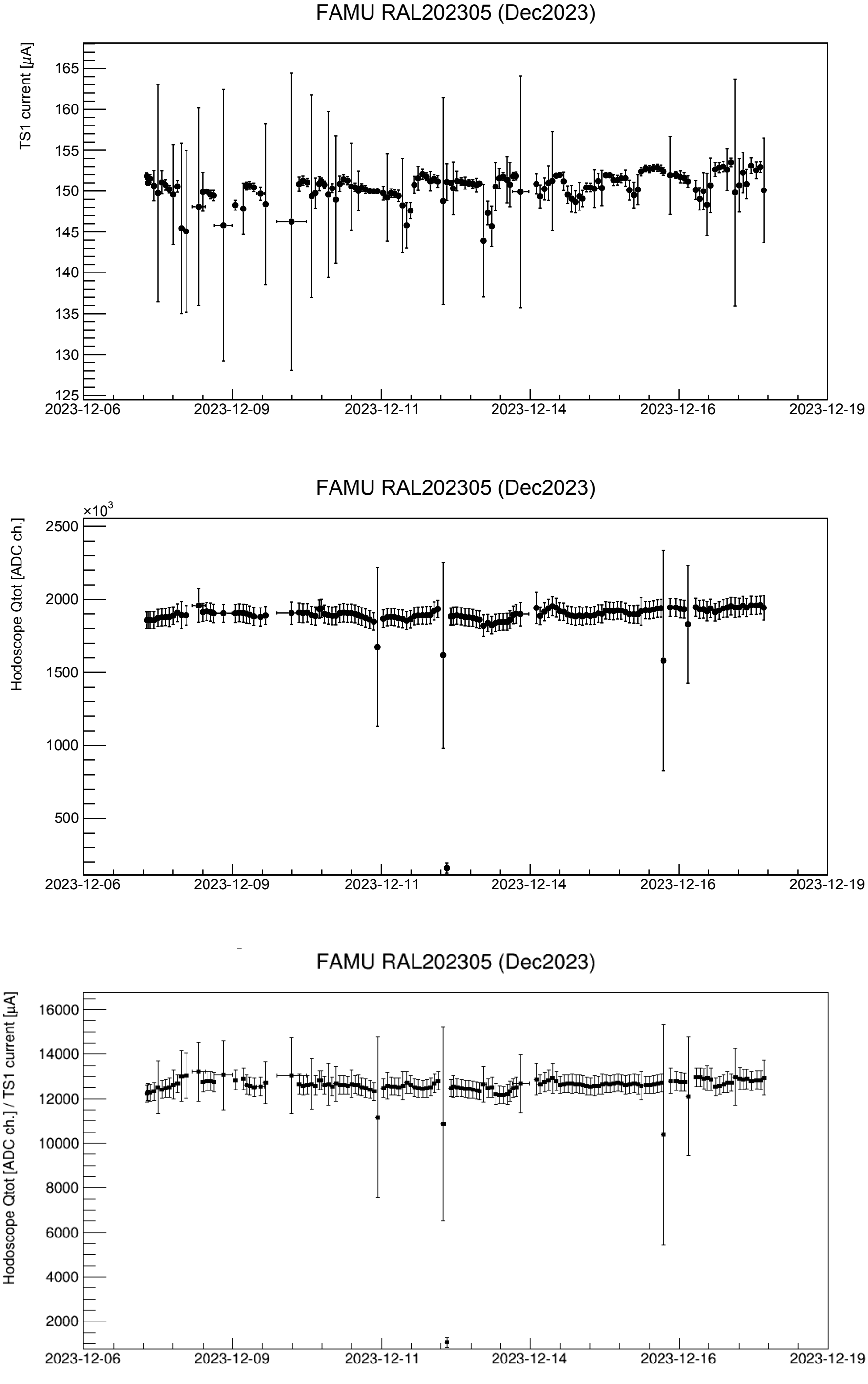

Figure 4.16: *Run-wise variation of the synchrotron current delivered to TS1, the average hodoscope deposited charge Q_{tot} per trigger and their ratio, respectively. The outliers in Q_{tot} are not balanced out, confirming they are due to issues in the muon beamline and not in the proton one.*

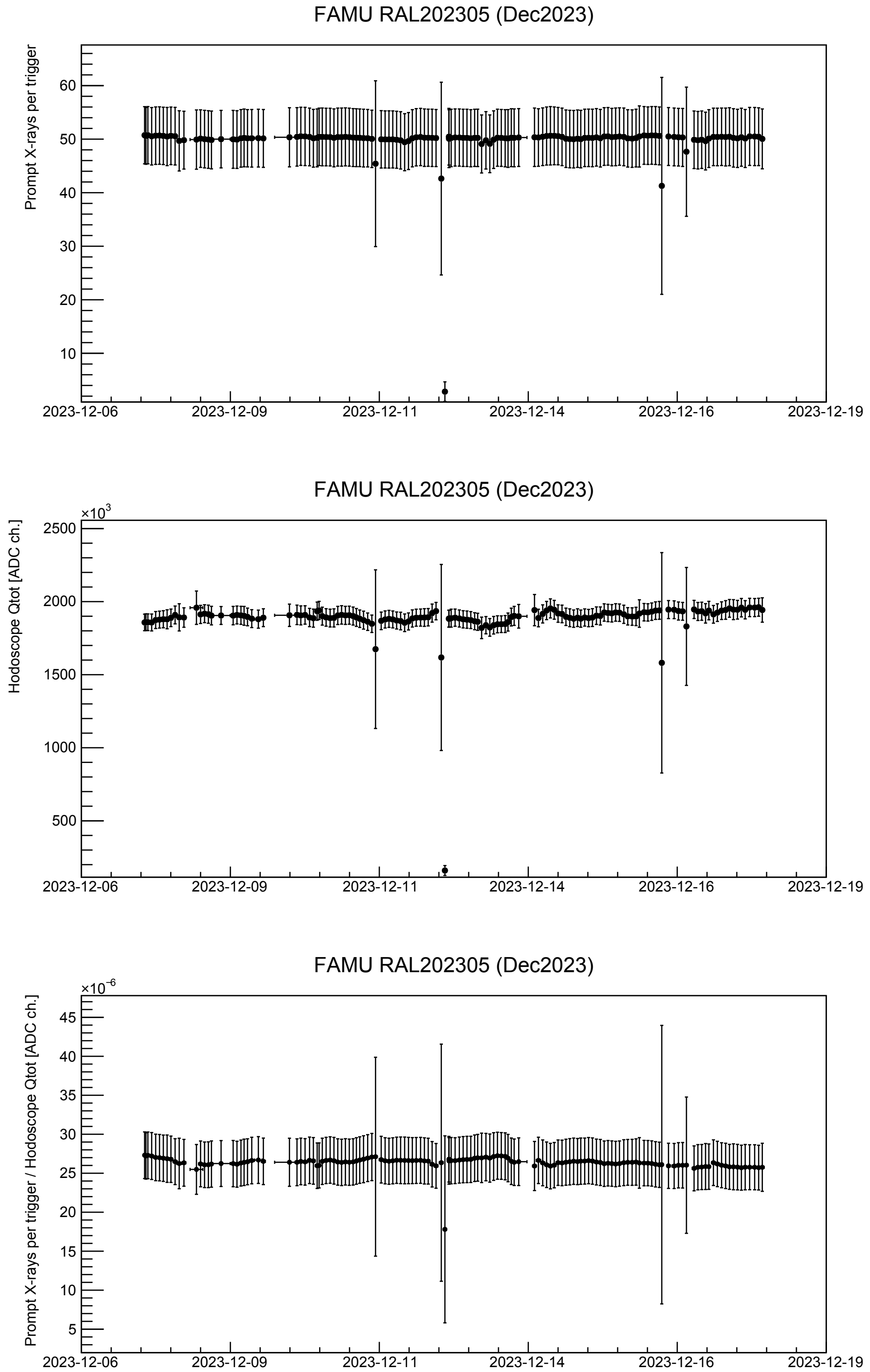

Figure 4.17: *Run-wise variation of the average number of detected prompt X-rays per trigger, the average hodoscope deposited charge Q_{tot} per trigger and their ratio, respectively. The outliers in Q_{tot} are present also in the number of X-rays, and the ratio is constant.*

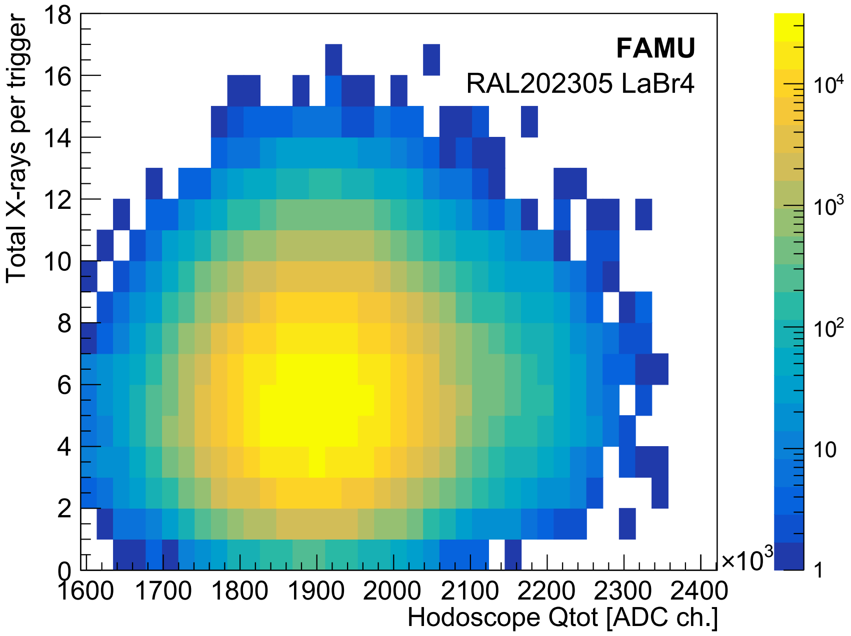

Figure 4.18: *No visible correlation between the total number of X-rays and the event-by-event oscillation of* Q_{tot}*. This suggests that the oscillation is due to the hodoscope resolution.*

In particular, the variation of pressure, temperature and their ratio over acquisition runs during RAL202305 (December 2023) is shown in Figure 4.19. In six occasions, the temperature sensor failed and returned non-trusted values (visible in the plots with big uncertainties and not taken into account for this study). The ratio plot (third) shows a clear linear decrease of the P/T ratio, which has been fitted successfully with a linear model to extract the decrease rate. In addition, the clear linearity of this profile, despite the oscillations in pressure and temperature, confirms the good working conditions of the pressure and temperature sensors.

A first hypothesis to explain the loss could be that the ideal gas equation does not hold in these conditions. The other option is to use the van der Waals equation for real gases: $(P + an^2/V)(V - bn) = nRT$. However, this equation is generally needed for very high pressures (> 50 bar) where inter-atom Van der Waals forces are relevant, whereas the pressure used in this experiment is $7 - 8$ bar. In addition, if we assume that the container is perfectly sealed, i.e. volume V and amount of substance n are constant, the van der Waals equation can be re-written as $P = C_0 + C_1 T$, with C0, C1 positive constants. As a consequence, this would not explain the linear decrease in P/T.

For these reasons, the shape P/T plot is attributed to an actual gass leakage. Regarding the RAL202305 data specifically, assuming the ideal equation

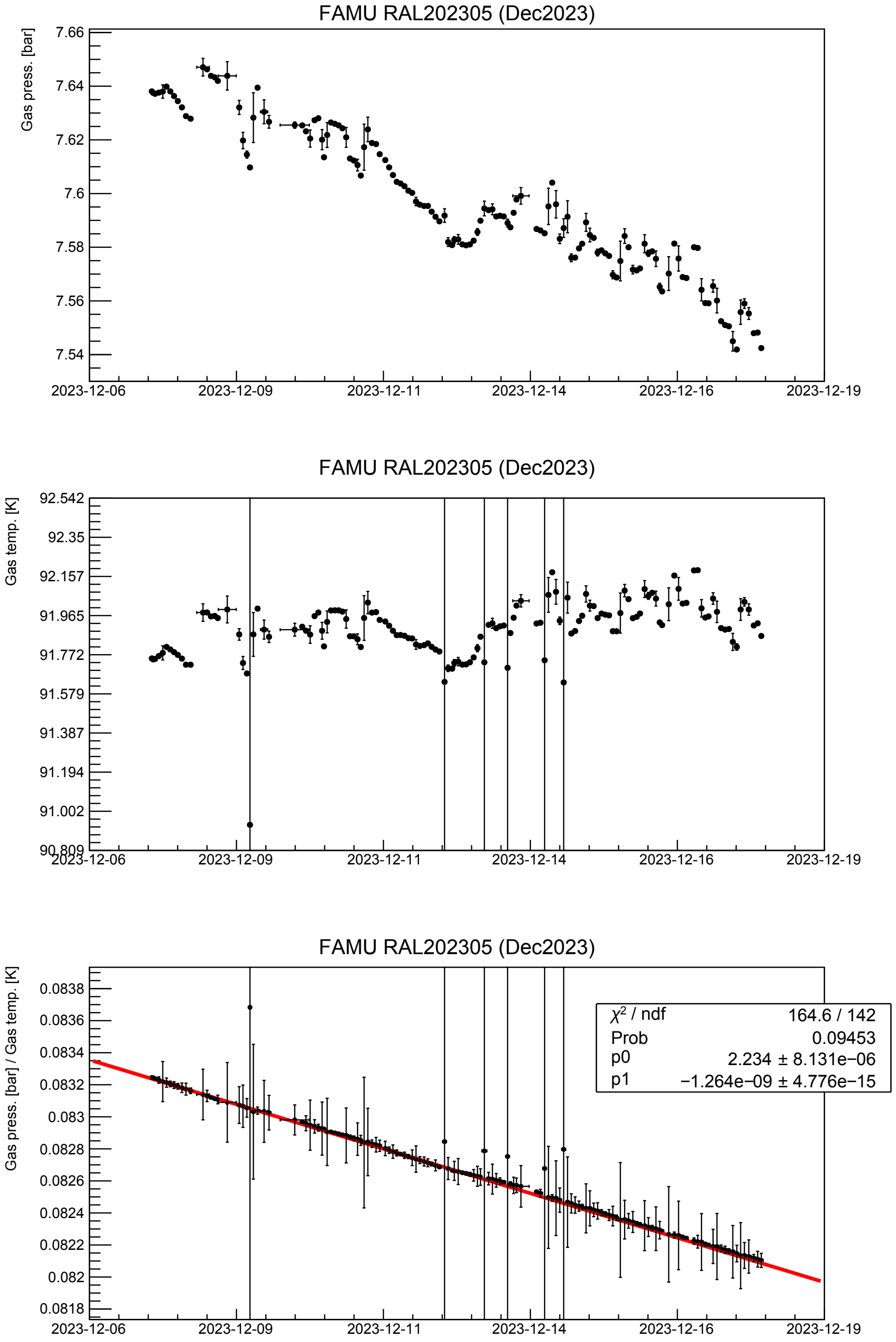

Figure 4.19: *Run-wise variation of the average gas pressure, gas temperature and their ratio. In particular, the ratio is related to the amount of gas in the target* ($P/T \sim n$) *and it has a clear linear diminution, which has been fitted.*

for gases holds, the P/T ratio can be written as a function of time t as:

$$\frac{P}{T} - \frac{P_0}{T_0} = k_{PT}(t - t_0), \tag{4.4}$$

where k_{PT} is the linear coefficient p_1 obtained from the fit of P/T. The actual gas leakage rate can be estimated to be about -1 nmol/s, which corresponds to -1.4% gas loss during the whole RAL202305 period (12 days), considering the initial amount of gas is ~ 1 mol. If the effect of the resonance is the order of 1%, it appears crucial to correct for this leakage.

Combining Equation 4.4 and the ideal gas equation (Vconst. $\Rightarrow P/T \sim n$), one can write the following expression for the gas loss:

$$\frac{n}{n_0} \propto \frac{P/T}{P_0/T_0} = \frac{k_{PT}}{P_0/T_0}t + \left(1 - \frac{k_{PT}\ t_0}{P_0/T_0}\right), \tag{4.5}$$

which corresponds to the left plot in Figure 4.20. In order to correct for this effect, a candidate expressions for the correction factor is its symmetry over the horizontal line $y = 1$, i.e.:

$$w_{PT} = 2 - \frac{P/T}{P_0/T_0} = \frac{k_{PT}}{P_0/T_0}t - \left(1 + \frac{k_{PT}\ t_0}{P_0/T_0}\right), \tag{4.6}$$

which corresponds to the second plot in Figure 4.20, where it has been calculated for each point and not from the fit (for check purposes). In order to verify this expression for w_{PT}, the bottom panel of Figure 4.20 shows the gas loss in Equation 4.5 multiplied by w_{PT} in Equation 4.6. The gas loss must be corrected: in fact, by applying w_{PT}, the maximum residual discrepancy is of only about 0.02% (while the uncorrected one is 1.4%).

Given the good linearity of P/T during all data acquisition periods, it has been decided to fit P/T over time and apply a correction using the fit parameters. Given the small discrepancy over a run duration (about 1 h), it has been decided to apply a run-wise correction using Equation 4.6 with the median time of the run as t.

The correction factor for the target gas has to be equalised among all acquisition periods. In fact, the initial amount of gas during each data taking may be slightly different, so the initial reference has to be the same. An example is shown in Figure 4.21: the two data acquisition periods A and B (grey) have slightly different initial P/T ratio. The first value ($(P_0/T_0)_A$) is taken for reference, therefore value of w_{PT} for the second data acquisition period must be referred to $(P_0/T_0)_A$. In this example, the value of P_0/T_0 in Equation 4.6 will always be the same, whereas t_0 and k_{PT} will be determined every time.

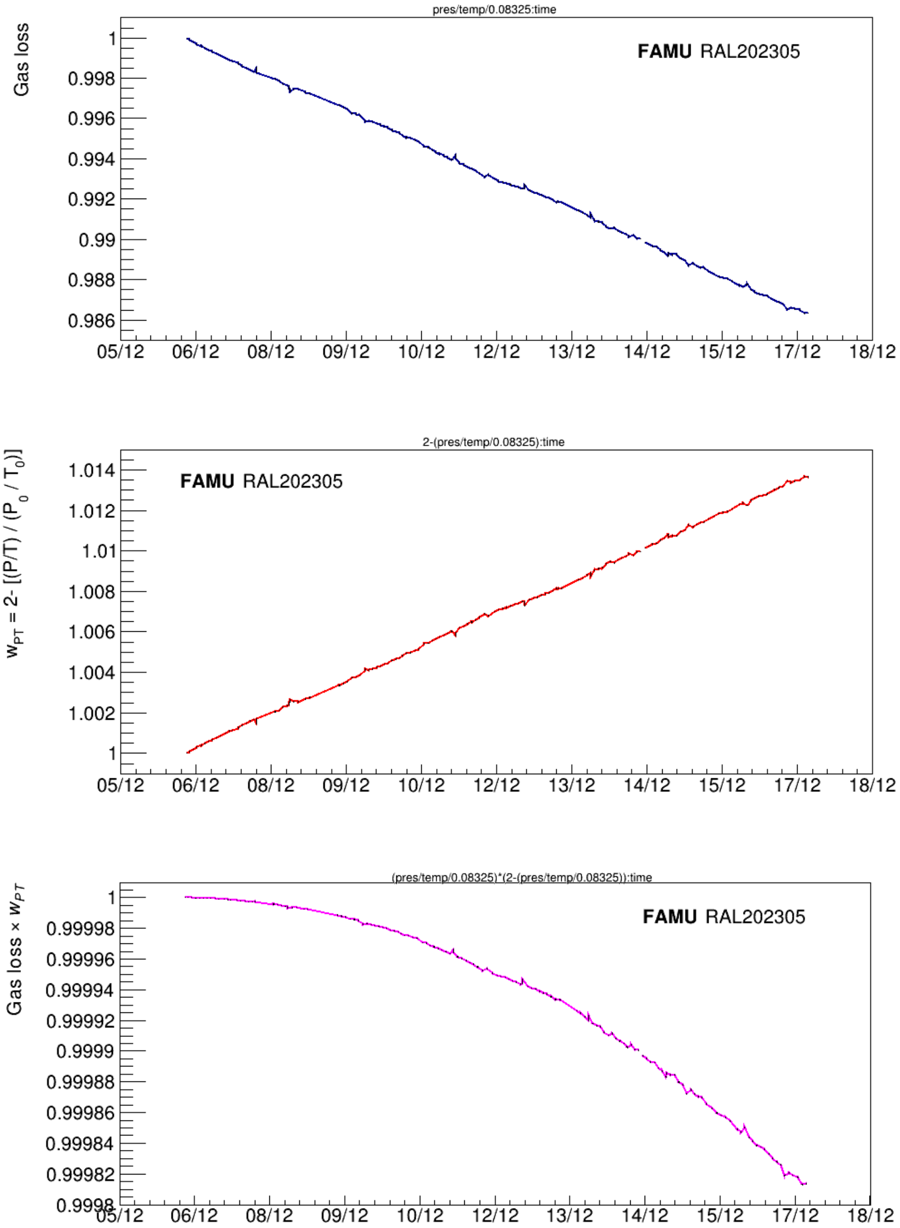

Figure 4.20: *Gas loss normalisation. Upper panel: relative gas loss during December 2023 (total -1.4%). Central panel: value of the correction factor w_{PT}, computed event-by-event. Bottom panel: the two values multiplied by each other (i.e. the gas loss corrected by w_{PT}) show a residual discrepancy of $\sim 0.02\%$, showing that w_{PT} is a good correction factor for the gas loss.*

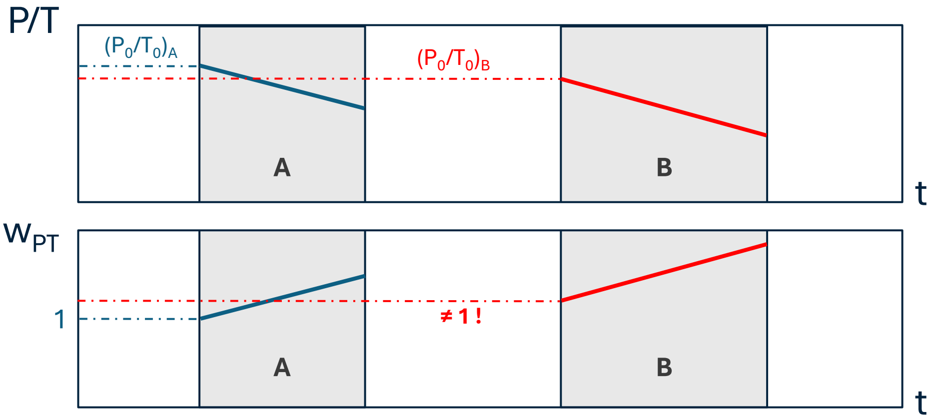

Figure 4.21: *Supposing that two beamtime periods A and B have slightly different initial amount of gas (proportional to P/T), the correction factor for the target gas conditions w_{PT} needs to be referred to the same value of initial P/T for every data acquisition. For example, if $(P_0/T_0)_A$ is the reference, w_{PT} will not be 1 at the beginning of period B, as $(P_0/T_0)_B \neq (P_0/T_0)_A$.*

4.3.3 Data normalisation summary

In conclusion, the variables to equalise for target and muon beam conditions have been studied in this chapter in order to develop a normalisation protocol on these variables. The normalisation is averaged for each run, and it can be written as in Equation 4.2, where $w_{Q_{tot}}$ and w_{PT} are calculated using Equations 4.3 and 4.6, respectively. In these equations it is important to notice that Q_0 and P_0/T_0 are the same for all data takings in order to inter-calibrate them, whereas Q_{tot}^{avg} and t are determined for every run, while k_{PT} and t_0 are fixed in a data acquisition period, but will change among different periods.

4.4 X-ray detector performance

All detector behaviours have been analysed carefully during the 2023 acquisition periods. The off-line data processing described in Section 4.2.2 was applied to all detectors and the cut thresholds were optimised on the whole detector setup. For an example of data skimming applied to detector read by PMTs (LaBr) see the aforementioned section of this work. Figure 4.22 summarises some of the cuts carried out on a 1″-SiPM detector (MIB89) taken for reference, and the resulting prompt and delayed X-ray spectra are shown in Figure 4.23. No particular issues were found with these MIB detectors, apart from the different time features of the typical pulses which required several optimisations of FAMUAnalysis and therefore raw data reprocessing.

However, detector LaBr2, belonging to the central ring of detectors with PMT-based reaout, showed some atypical behaviour. In fact, first of all, the number of X-rays measured by these detector was consistently much higher (by a factor $\sim 2-3$) than all other detectors. This fact could not be justified with the position of the detector, as other detectors in symmetrical position with respect to the target showed a similar behaviour. For reference, Figure 4.24 shows a comparison among LaBr2, LaBr4 and MIB89 in terms of distribution of the number of reconstructed X-rays per event (i.e. per trigger). While LaBr4 and MIB89 (which show a behaviour perfectly in accordance to the other detectors of their class) detect respectively 3 and 5 X-rays per event as mode, LaBr2 detects a mode of 87 X-rays with an asymmetrical distribution giving an even higher average (14.2). Such a behaviour is generally consistent with an oscillation in the beamline which causes noise issues. In fact, having a look at the waveforms and the reconstruction flag, it turned out that saturated pulses are common for LaBr2, and that they are generally followed by an instability that can be recognised by FAMUAnalysis as a collection of pulses, as in the example shown in Figure 4.25. In addition, such oscillations have a crucial contribution in enhancing the noise of the LaBr2 detector baseline. In fact, as one can observe in Figure 4.26, the distribution of RMS_{bsl} is much different from the one of the other detectors, as it has a higher-RMS structure due to such baseline oscillations. In this case, the standard set of cuts would include most of these events. For this reason, it has been decided to apply a stricter cut $RMS_{bsl} < 10$, which enabled to extract prompt and delayed spectra for this detector, shown in Figure 4.27. For the delayed spectrum, the signals below 60 keV (instead of just 40 keV as in the standard set of cuts) was applied to remove the soft spectrum which is strongly affected by these noise effects. Still, the calibration prompt peaks are visible and the detector resolution is not greatly affected by the noise with this data skimming. However, the oxygen peaks have lower statistics with respect to other detectors in symmetrical position with respect to the target.

Data skimming cuts for ½″ detectors and the germanium detectors are currently being studied and have not been included in this work.

In order to check if any other data selection had to be applied, it has

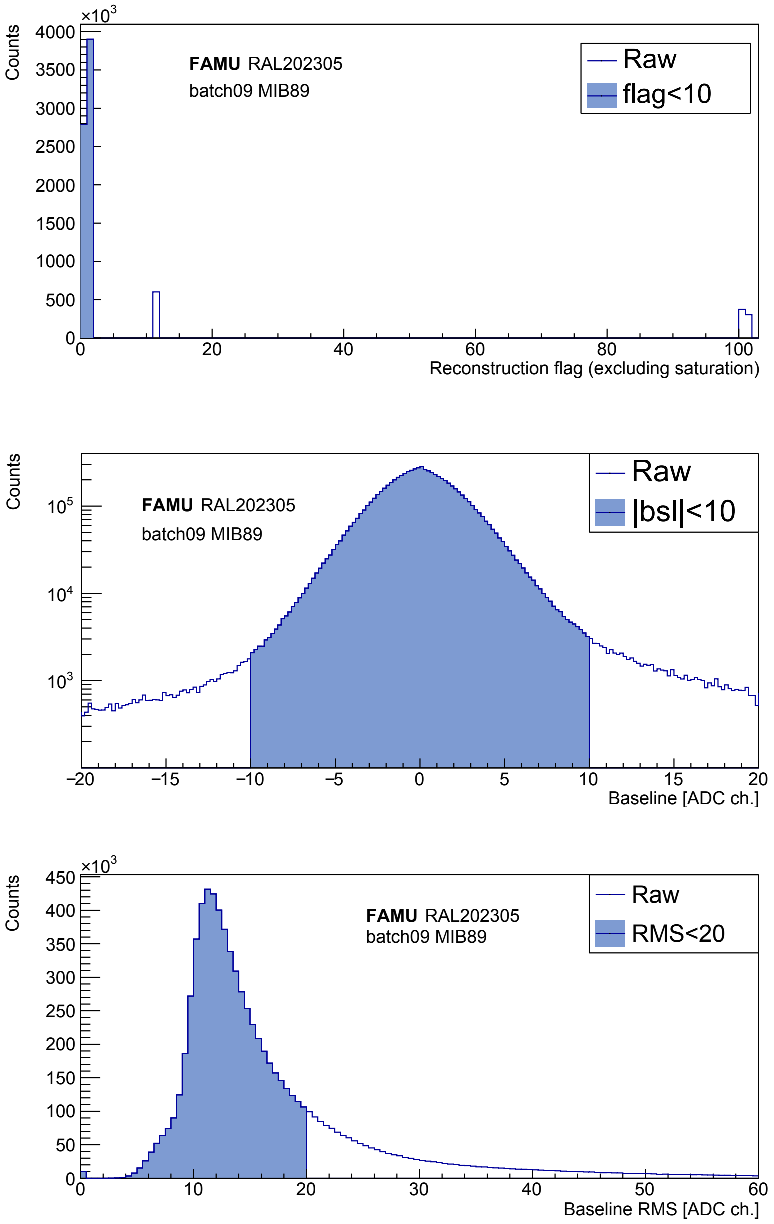

Figure 4.22: *Standard set of cuts applied to MIB89 detector in RAL202305 data.*

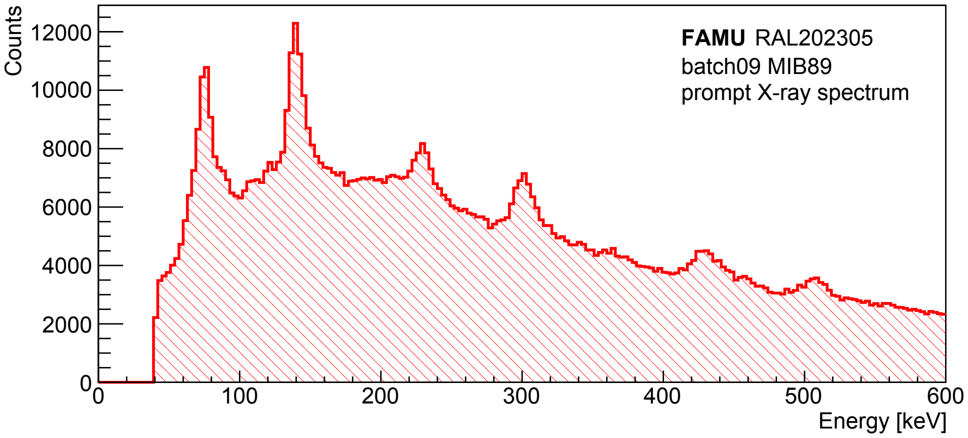

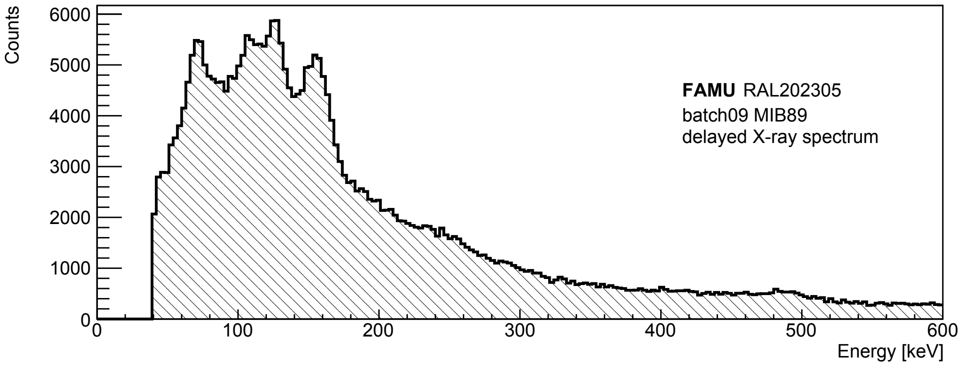

Figure 4.23: *Prompt (upper, $t \in [120\ ns, 220\ ns] \cap [450\ ns, 550\ ns]$) and delayed (lower, $t \in [780\ ns, 3000\ ns]\ ns$) spectra of detector MIB89 in RAL202305 batch09.*

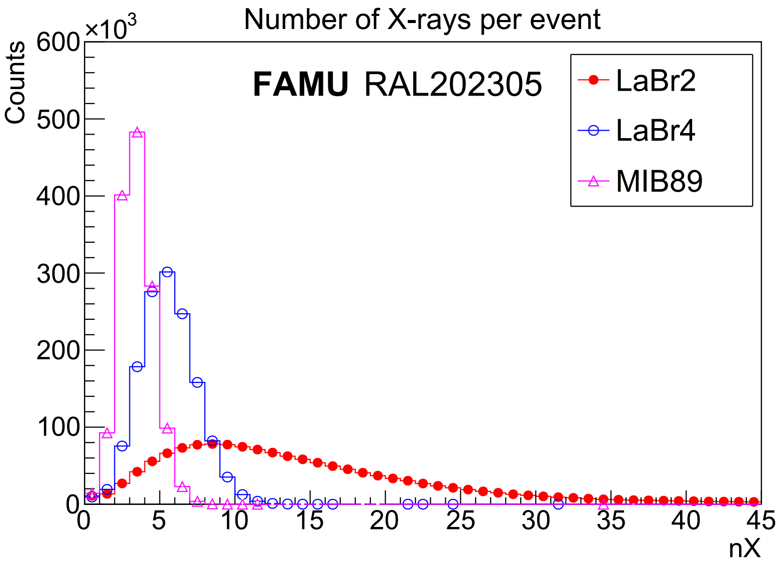

Figure 4.24: *Comparison between the number of reconstructed X-rays per event (`nX`) detected by LaBr4, MIB89 and LaBr2 in a selection of RAL202305 data. Detector LaBr2 is the only one with `nX` sensibly different from all other 1″-PMT detectors, which initially led to think it might have some noise issues.*

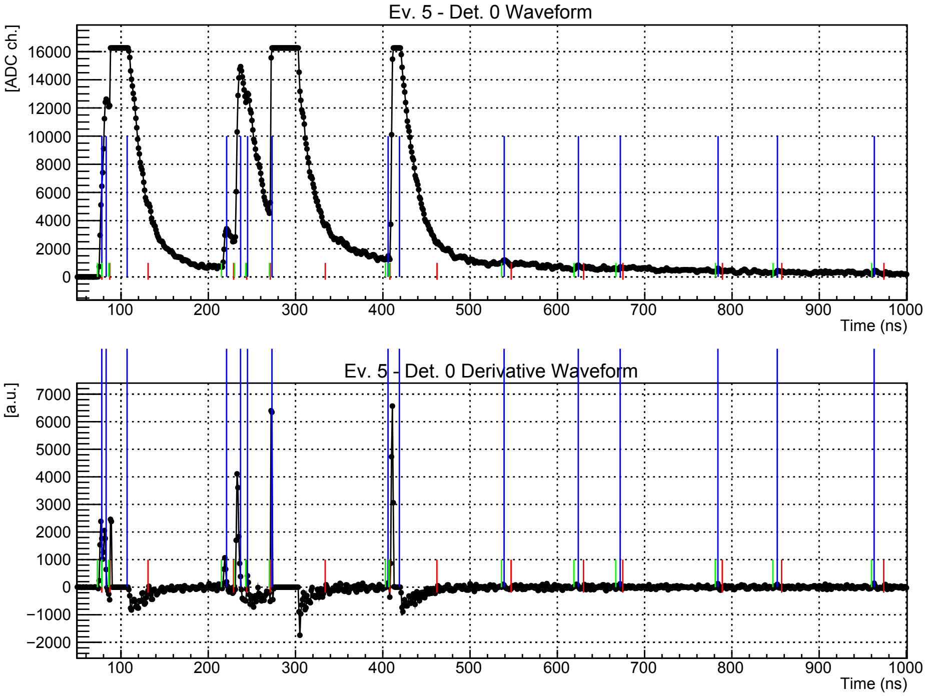

Figure 4.25: *Example of signal saturation for LaBr2: the oscillations following the saturation are recognised as pulses, enhancing the apparent number of detected X-rays and resulting in the distribution in Figure 4.24. Data cuts for LaBr2 were set in order to exclude these spure pulses (for example with a threshold in energy and excluding events when the flag marks that a saturation has happened).*

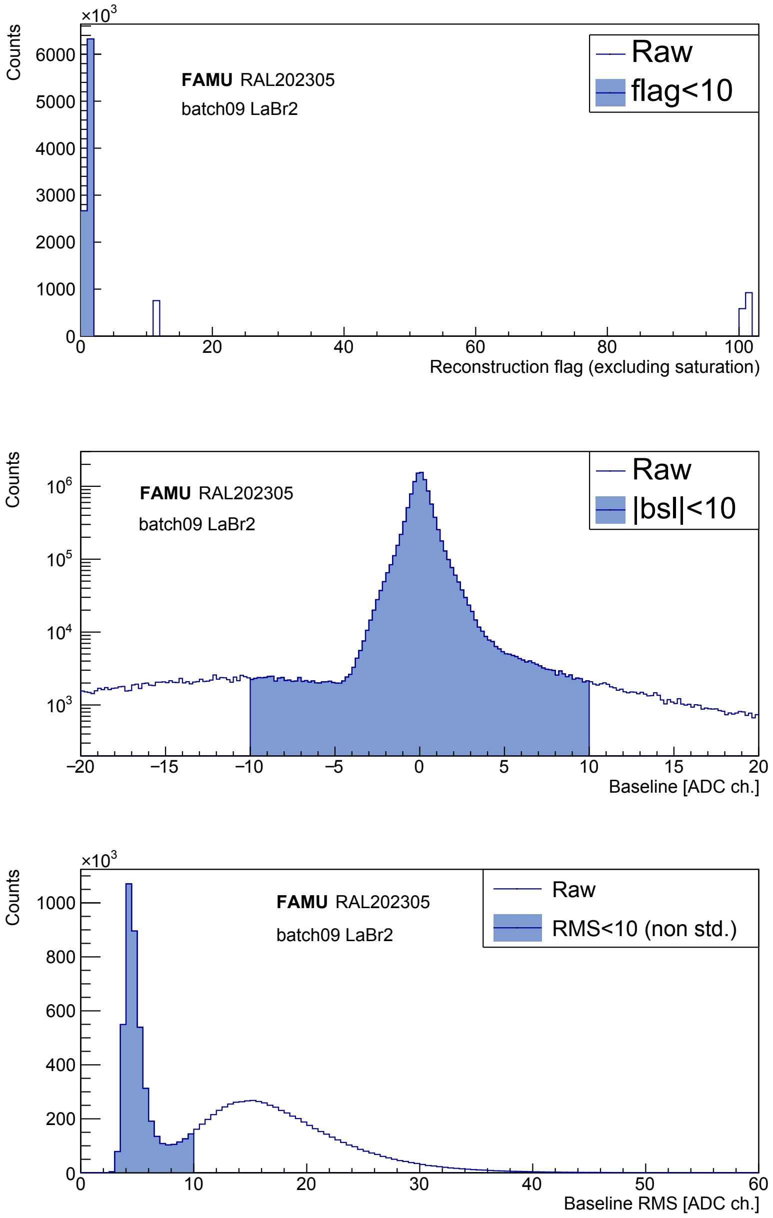

Figure 4.26: *Signal cuts on LaBr2 detector: signal reconstruction flag (required* $f < 10$ *i.e. no saturation, unresolved or over-unresolved signals), time since previous pulse* ($\Delta_t > 30ns$)*, baseline average level* ($|bsl| < 10$) *and baseline oscillation* ($RMS_{bsl} < 10$*, different from the standard cut). It is clearly visible how these plots are different from those of other 1″ detectors (Figures 4.13 and 4.22). In particular, the oscillation of the baseline seems the leading factor in the LaBr2 noise issue. A stricter threshold (60 keV instead of 40 keV) has been imposed as LaBr2 soft spectrum is strongly dominated by noise.*

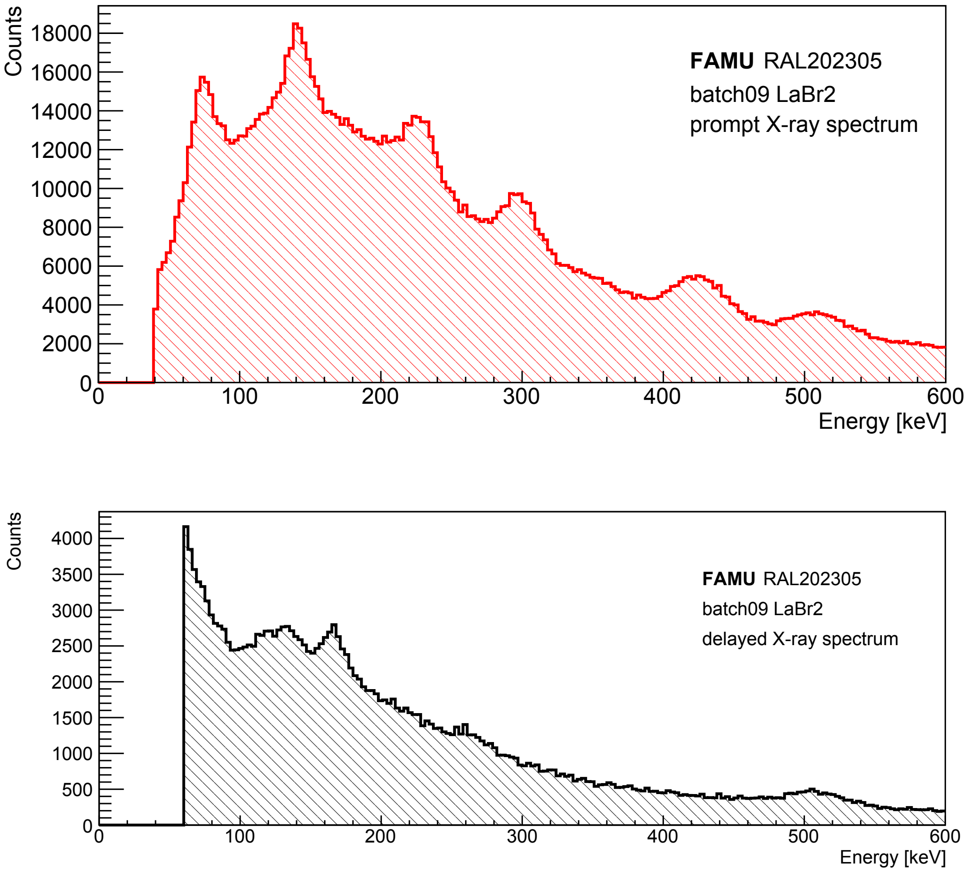

Figure 4.27: *Prompt (upper, $t \in [120\ ns, 220\ ns] \cap [450\ ns, 550\ ns]$) and delayed (lower, $t \in [780\ ns, 3000\ ns]$ ns) spectra of detector LaBr2 in RAL202305 batch09.*

been decided to check for any multiple-event detector inactivity. Assuming that the distribution of the number of X-rays per event follows a Poisson distribution, the probability of observing no X-rays for n consecutive events is $p_\mu(n) = e^{n\mu}$, where μ is the average number of events observed per event. For a typical detector, $\mu = 3$ (see Figure 4.24), and therefore $p(3) \simeq 0.1‰$. As a consequence, significative multiple-event inactivity for more than 3 consecutive events should be due to a detector or beam fault and it is therefore be rejected from the dataset. To study this behaviour, the distribution of the total number of X-rays over 40 keV in the current and the next j events, `nX`j was extracted for values of j up to 8. The histograms of `nX`, `nX4` and `nX8` are plotted in Figure 4.28 for the whole RAL202305 dataset. It can be noted that the distributions of higher j have some events with `nX`$j \simeq 0$.

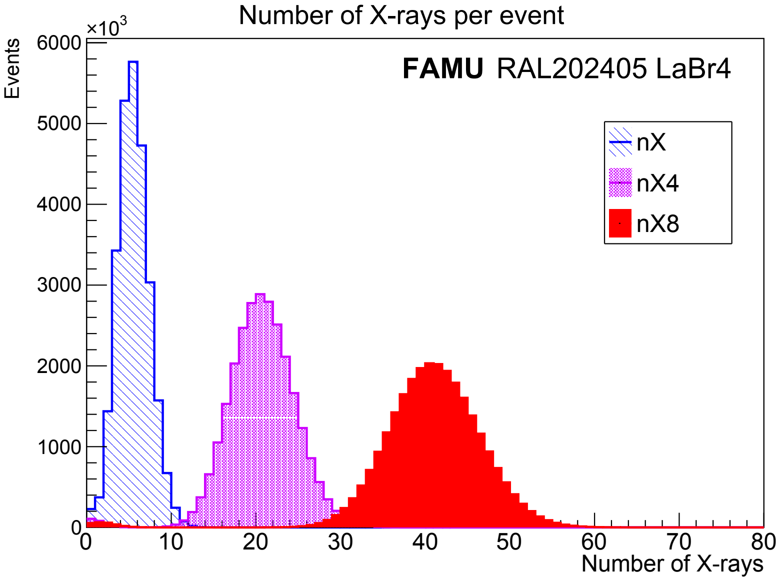

Figure 4.28: *Histogram of the number of reconstructed X-rays detected by LaBr4 in the whole RAL202305 period for one event (nX), for 4 subsequent events (nX4) and for 8 subsequent events (nX8).*

In order to check if this is due to detector or beam fault, the correlation of these events with the beam has been studied. Figure 4.29 is a distribution of the values of hodoscope Q_{tot}, where the main peak around $(1.9 \cdot 10^6)$ ADC channels corresponds to standard beam and lower values are related to the beam magnet faults described in Section 4.1.1. The 2D correlation plot between `nX8` and Q_{tot} is shown in Figure 4.30. It shows quite clearly that the events of detector lethargy are correlated with the beam faults and not to detector faults. Repeating this analysis on all detector it has been shown that no evidence of temporary detector lethargy out of the beam faults is observed. As a consequence, no data rejection for detector fault is needed for RAL202305 data, as events with reduced hodoscope Q_{tot} are already rejected in the analysis process.

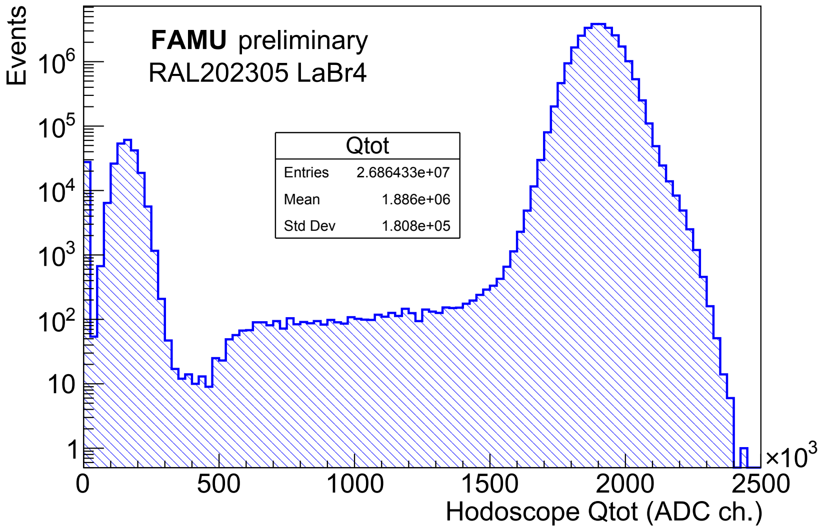

Figure 4.29: *Distribution of the values (in log scale) of the hodoscope* Q_{tot} *during RAL202305. The values away from the mean of the main peak correspond to the beamline faults.*

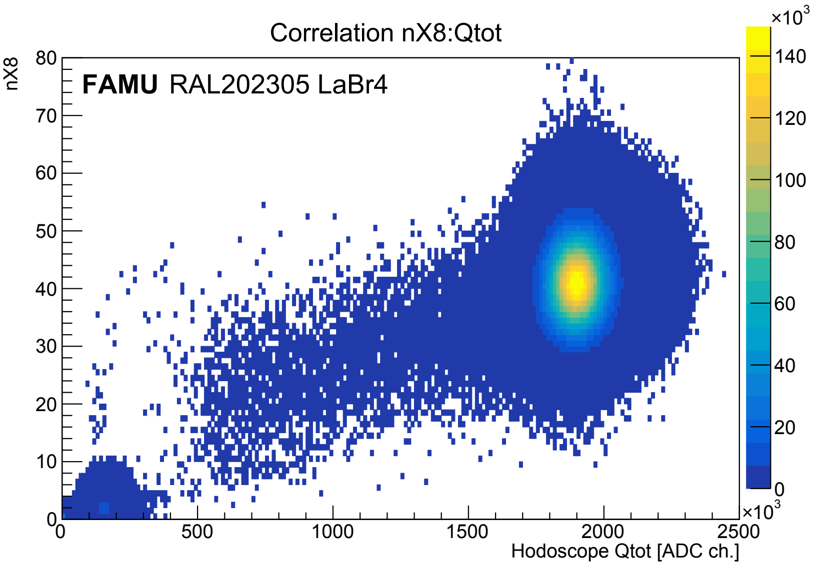

Figure 4.30: *The correlation plot between the number of reconstructed X-rays for 8 subsequent events (`nX8`) for LaBr4 and the hodoscope* Q_{tot} *during RAL202305 reveals that the zeros and low outliers in the `nX8` distribution correspond to the beamline faults.*

4.5 Delayed X-ray plots

After these studies were completed, all the software and cuts optimised and the datasets re-calibrated with prompt peaks, it was possible to sum the signals from all detectors to extract the required information. As in the last Section, batch09 from RAL202305 is reported here for reference. The aim of this part of the work was identifying the net number of X-rays resulting from delayed transfer of the muon from hydrogen to oxygen, in order to have an idea of the statistics of the experiment, verify that a significant amount of muons is effectively deposited in the gas, and check the quality of the detectors and their positioning.

The plot from 22.5 hours of data taking measured with all 1″-PMT (LaBr) scintillating detectors with the gas mixture is shown in the upper panel in Figure 4.31 as a black line. By subtracting this measurement with one carried out with pure hydrogen in July 2023 (red filled spectrum in the same plot) it was possible to extract the net oxygen contribution (bottom panel). The resolution is comparable with the one for single detectors: this is a clear marker that the calibration with prompt X-rays is successful.

It is particularly interesting to notice that the two unrecognised peaks in the delayed spectrum, described in Section 4.2.2 and marked as *other* in Figure 4.15, are present in both the hydrogen and mixture spectra shown in the upper panel in Figure 4.31. This confirms that the emissions causing these peaks are related to processes involving the materials of which the target is made of, and not the gases themselves. The subtraction plot (bottom panel in Figure 4.31) shows a peak asymmetry on the left due to incomplete charge collection and detection of X-rays which underwent Compton scattering in the target material.

Table 4.3 and Figure 4.32 show an estimation of this net contribution for each detector. These maps allow to identify damaged detectors, along with detectors in position where the X-ray propagation out of the target is strongly suppressed. For example, detectors positioned near the vertical tend to measure less X-rays due to the enhanced absorbtion by the optical cavity assembly and mirrors. This was well expected, indeed, detectors were arranged in order to maximise the coverage at angles close to the horizontal. They also show quite clearly that LaBr detectors have higher X-ray reconstruction efficiency with respect to 1″-SiPM detectors, which is mostly due to faster signals and therefore less saturated, unresolved or over-unresolved signals, and lower pile-up yield.

Figure 4.33 shows the total μO emission rate as a function of time, for all detectors, over the whole dataset of batch09 (both laser, L, and no-laser, nL). These plots are similar to those used to estimate the muon transfer rates in the previous phases of the experiment [45, 46]. When data are separated in L and nL sub-datasets, any net signal during a batch would have to show up in this plot as in the illustration in Chapter 2, Figure 2.2.

The actual separation of data in laser and no-laser sub-datasets has not

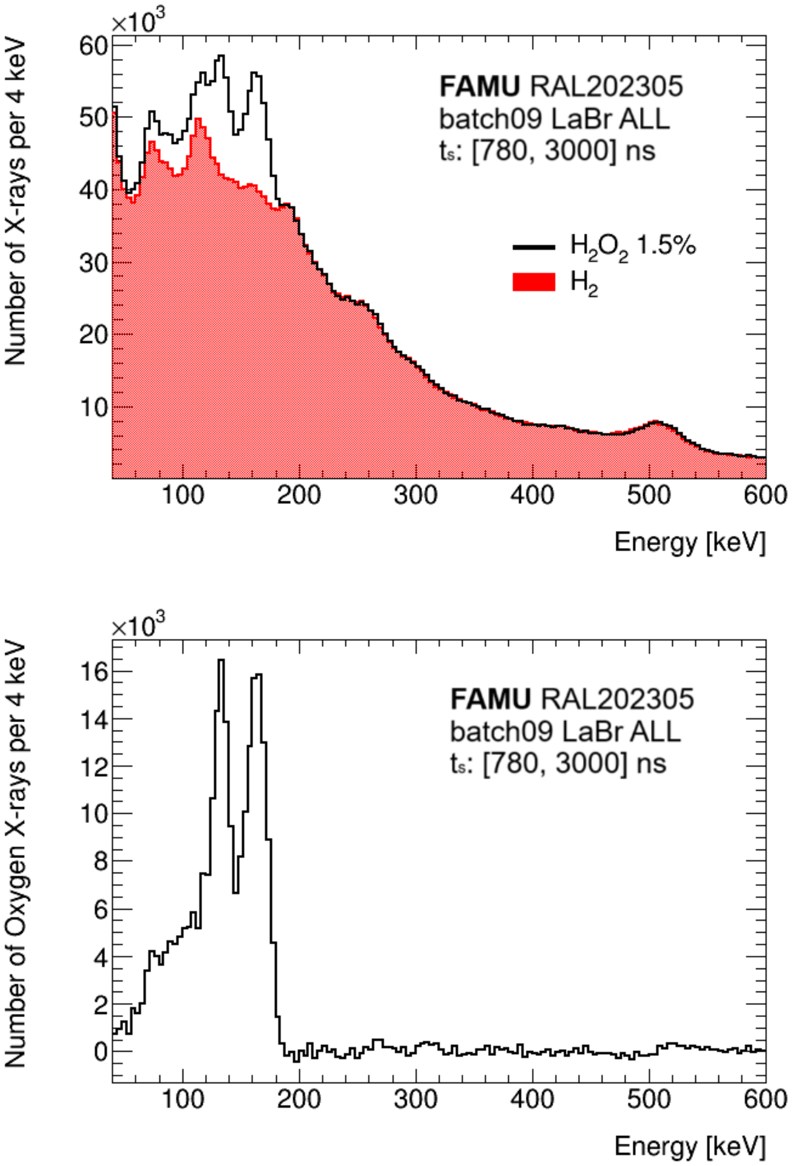

Figure 4.31: *Subtraction of the normalised* H_2 *delayed background, measured in July 2023 as part of RAL202303, from the delayed spectrum in RAL202305 batch09, for LaBr4. Upper plot shows the two histograms, lower plot the net subtraction which is the net oxygen contribution. Similar subtraction plots were also made for every detector and they have been used to calculate the net number of oxygen X-rays for each detector in table 4.3.*

Table 4.3: *Total number of μO X-rays calculated for each detector on RAL202305 batch09 data by subtracting the H_2 background (see Figure 4.31). A graphical representation of these data is shown in Figure 4.32. The data processing for ½″-SiPM detectors is still under tuning and they have not been included in the study.*

Detector	**Ring**	**#μO X in 22.5h $[\times 10^3]$ no data selection**	**#μO X in 22.5h $[\times 10^3]$ standard selection**	**Selection efficiency**
LaBr2	Central	33 ± 3	21 ± 2	64%
LaBr4	Central	47 ± 2	44 ± 2	93%
LaBr5	Central	34 ± 2	32 ± 2	97%
LaBr6	Central	44 ± 2	42 ± 2	95%
LaBr7	Central	41 ± 2	40 ± 2	97%
LaBr8	Central	38 ± 2	37 ± 2	97%
Total 1″-PMT		$\mathbf{236 \pm 6}$	$\mathbf{215 \pm 6}$	**91%**

Detector	**Ring**	**#μO X in 22.5h $[\times 10^3]$ no data selection**	**#μO X in 22.5h $[\times 10^3]$ standard selection**	**Selection efficiency**
MIB72	Front	23 ± 2	18 ± 2	78%
MIB76	Front	25 ± 2	19 ± 2	73%
MIB79	Front	29 ± 2	25 ± 2	86%
MIB80	Front	27 ± 2	24 ± 2	87%
MIB81	Front	22 ± 2	20 ± 2	90%
MIB82	Front	21 ± 2	19 ± 2	91%
MIB83	Front	20 ± 2	16 ± 2	81%
MIB84	Front	32 ± 2	27 ± 2	86%
MIB85	Front	25 ± 2	23 ± 2	89%
MIB86	Front	19 ± 2	15 ± 2	79%
MIB71	Central	29 ± 3	16 ± 2	56%
MIB74	Central	24 ± 2	9 ± 2	39%
MIB78	Central	31 ± 2	25 ± 2	82%
MIB87	Central	37 ± 3	27 ± 2	71%
MIB88	Central	42 ± 2	29 ± 2	69%
MIB89	Central	44 ± 3	31 ± 2	71%
Total 1″-SiPM		$\mathbf{450 \pm 9}$	$\mathbf{346 \pm 9}$	**77%**
Total FAMU (excl. ½″-SiPM)		$\mathbf{686 \pm 11}$	$\mathbf{561 \pm 11}$	**82%**

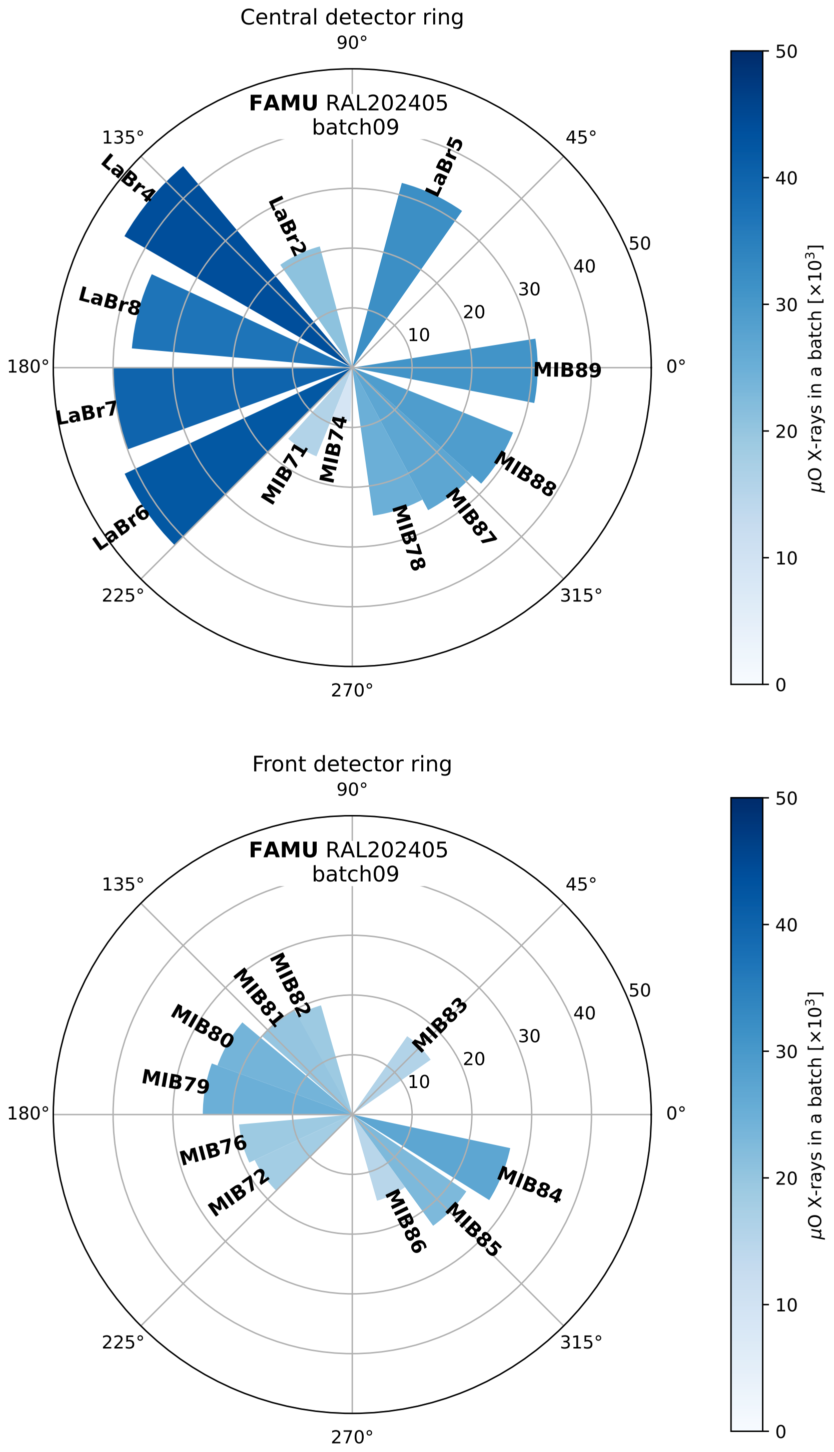

Figure 4.32: *Distribution of the reconstructed μO X-rays during a typical batch (RAL202305 batch09, 22.5 hours) on central and front ring detectors with the standard set of data selection cuts (see data in Table 4.3).*

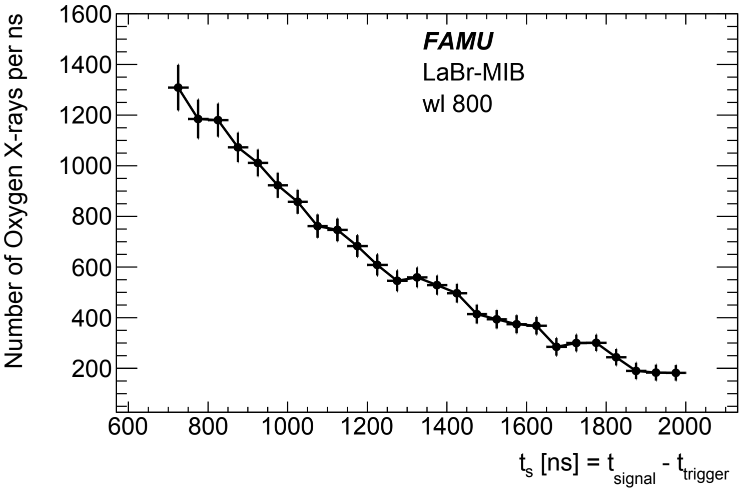

Figure 4.33: *Plot of the total μO emission rate in the delayed region, as a function of time, for all detector during batch09 in RAL202305 (22.5 hours of data acquisition with laser). This is the plot performed on all data without carrying out the $L - nL$ subtraction.*

been done yet as the experiment aims at a blinded analysis protocol. In this way, cognitive biases in the finding of hints of signal in given areas of the spectrum should be avoided. However, before this unblinding can be done, it is still important to set up a testing protocol for systematics in order to make sure that they are not conditioning the data acquired. For example, the plots in Figure 4.34 show the comparison and subtraction between two subset extracted by dividing batch09 in two parts based on the parity of the event number. Such studies should be repeated on the two sub-datasets L and nL (i.e. performing $nL - nL$ and $L - L$ subtraction tests) to make sure that no difference appears among events within these sub-datasets. This comparison should be carried out for all detectors and batches prior to the final phase of the analysis aimed at extracting the resonance plot. These studies are currently undergoing. At that point, the blinding should be applied to the batch number and the wavelength in order for the analysis group not to know which wavelength data are being analysed. The data unblinding should be carried out all at once at the end of the analysis procedure. For this reason, no $L - nL$ subtraction has been carried out yet, and therefore no plots about this are presented in this work.

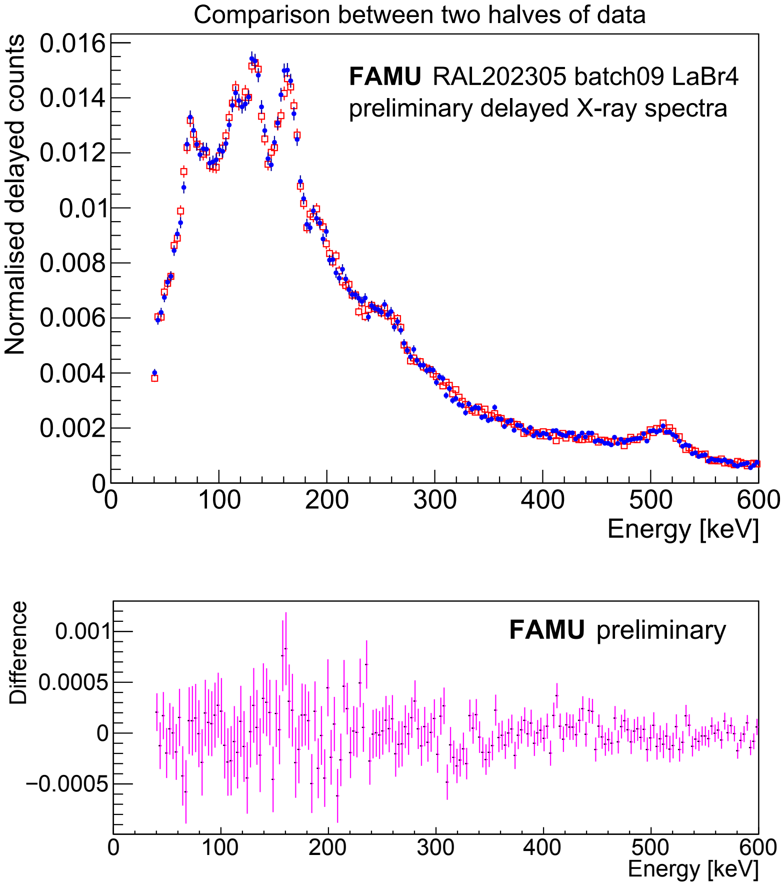

Figure 4.34: *Example of test for systematics: the dataset of batch09 in RAL202305 for LaBr4 has been randomly divided event-wise in two sub-dataset of nearly the same size. The reconstructed and skimmed delayed X-rays are compared in the upper plot and subtracted in the lower one. Such study, applied here as an example on one detector and on the whole dataset* $(L + nL)$ *should be repeated on the two dataset subsets* L *and* nL *for all batches and all detectors in order to make sure the* $L - nL$ *subtraction is not characterised by net systematic effects.*

4.6 Summary

The whole data analysis procedure for the FAMU experiment has been described in this last Chapter. In particular, data need a thorough normalisation, which is aimed at correcting fluctuations and drifts in:

- the number of events collected in a single batch;
- the muon beam, specifically its fluctuations in flux which are corrected by their run-wise average;
- the laser beam, specifically in terms of energy delivered per event (which is proportional to the number of photons and thus to the probability of interaction);
- the amount of gas in the target, which is slightly decreasing over time by ~ 1 nmol/s.

In addition, data skimming is crucial to make sure each dataset is free of nuisance data such as:

- X-rays collected with oscillating or out-of-average baseline, with bad pile-up reconstruction or saturation;
- events collected when the muon beam was low due to beam faults, for example during magnet HV issues in RAL202305;
- events collected when the laser energy was too low or the wavelength was out of range;
- events in which detector lethargy was present, i.e. a detector was not observing X-rays for several subsequent events suggesting it was malfunctioning.

Finally, the next steps for data analysis were presented in order to give a broad picture of the path followed to reach a final resonance plot, from which hopefully extracting an estimate for the hyperfine splitting in μH. Currently, the data analysis group is not yet in this phase, as some studies of systematics and data blinding are required before being able to perform the final $L - nL$ subtractions for each batch, but this path will be followed in the next months of work.

Conclusion

This PhD thesis work in Physics at the University of Pavia has been carried out in the framework of the FAMU experiment, at the Rutherford Appleton Laboratory in Didcot, United Kingdom. The experiment is funded by Istituto Nazionale di Fisica Nucleare (INFN) and carried out at the RIKEN-RAL Port1 decay muon facility, part of the ISIS Neutron and Muon Source.

In particular, the main experimental focus has been on the muon beam monitor. Thanks to the work presented in this thesis, specifically in Chapter 3, this detector was converted from being a simple hodoscope for beam focusing and centering, to a complete beam monitor with flux-meter capabilities. This was made possible by combining a low-flux measurement carried out directly at the Port1 beamline by beam optics de-tuning, and a complete simulation in Geant4 of the energy deposited in the detector (Q_{tot}), in order to develop an efficient and reliable model to convert the Q_{tot} into the instantaneous muon flux. The simulation has been validated by comparison with a model developed on the same geometry using FLUKA.

Thanks to this detector upgrade, it was possible to develop a strategy for the calibration of FAMU data as a function of the incoming muon beam and the gaseous target conditions. This strategy, combined with the normalisation on the laser condition, has been implemented in the full FAMU analysis workflow, as described in chapter 4. In addition, much work was carried out on the X-ray detector data analysis in FAMU, in order to optimise the count of delayed μO X-rays which constitutes the core of the analysis procedure.

As of today, the analysis workflow is ready to be carried out, after completing the required systematic studies described in the last chapter. The analysis and unblinding of 2023 and 2024 data is to be carried out in the next months. The expected uncertainty on the Zemach radius is lower than the predicted resonance width, i.e. better than 0.003 fm. Such a result would be better by one order of magnitude of the current most accurate experimental values.

Bibliography

[1] C.E. Carlson. «The proton radius puzzle». In: *Progress in Particle and Nuclear Physics* 82 (2015), pp. 59–77. DOI: `10.1016/j.ppnp.2015.01.002`.

[2] A. Antognini, F. Hagelstein, and V. Pascalutsa. «The Proton Structure in and out of Muonic Hydrogen». In: *Annual Review of Nuclear and Particle Science* 72 (2022), pp. 389–418. DOI: `10.1146/annurev-nucl-101920-024709`.

[3] M. N. Rosenbluth. «High Energy Elastic Scattering of Electrons on Protons». In: *Phys. Rev.* 79 (4 1950), pp. 615–619. DOI: `10.1103/PhysRev.79.615`.

[4] D. R. Yennie, M. M. Lévy, and D. G. Ravenhall. «Electromagnetic Structure of Nucleons». In: *Rev. Mod. Phys.* 29 (1 1957), pp. 144–157. DOI: `10.1103/RevModPhys.29.144`.

[5] M.O. Distler, J.C. Bernauer, and T. Walcher. «The RMS charge radius of the proton and Zemach moments». In: *Physics Letters B* 696.4 (2011), pp. 343–347. DOI: `https://doi.org/10.1016/j.physletb.2010.12.067`.

[6] P.J. Mohr, B.N. Taylor, and D.B. Newell. «CODATA recommended values of the fundamental physical constants: 2010». In: *Rev. Mod. Phys.* 84 (4 2012), pp. 1527–1605. DOI: `10.1103/RevModPhys.84.1527`.

[7] R. Pohl, A. Antognini, F. Nez, et al. «The size of the proton». In: *Nature* 466 (2010), pp. 213–216. DOI: `10.1038/nature09250`.

[8] A. Antognini, F. Nez, K. Schuhmann, et al. «Proton Structure from the Measurement of 2S-2P Transition Frequencies of Muonic Hydrogen». In: *Science* 339.6118 (2013), pp. 417–420. DOI: `10.1126/science.1230016`.

[9] A. De Rújula. «QED is not endangered by the proton's size». In: *Physics Letters B* 693.5 (2010), pp. 555–558. DOI: `10.1016/j.physletb.2010.08.074`.

[10] I.C. Cloët and G.A. Miller. «Third Zemach moment of the proton». In: *Phys. Rev. C* 83 (1 2011), p. 012201. DOI: `10.1103/PhysRevC.83.012201`.

[11] W. Xiong, A. Gasparian, H. Gao, et al. «A small proton charge radius from an electron-proton scattering experiment». In: *Nature* 575 (2019), pp. 147–150. DOI: `10.1038/s41586-019-1721-2`.

[12] E. Tiesinga et al. «CODATA recommended values of the fundamental physical constants: 2018». In: *Rev. Mod. Phys.* 93 (2 2021), p. 025010. DOI: `10.1103/RevModPhys.93.025010`.

[13] J. C. Bernauer, P. Achenbach, C. Ayerbe Gayoso, et al. «High-Precision Determination of the Electric and Magnetic Form Factors of the Proton». In: *Phys. Rev. Lett.* 105 (24 Dec. 2010), p. 242001. DOI: `10.1103/PhysRevLett.105.242001`.

[14] X. Zhan, K. Allada, D.S. Armstrong, et al. «High-precision measurement of the proton elastic form factor ratio $\mu p G_E/G_M$ at low Q^2». In: *Physics Letters B* 705.1 (2011), pp. 59–64. DOI: `10.1016/j.physletb.2011.10.002`.

[15] Mihovilovič, M., Achenbach, P., Beranek, T., et al. «The proton charge radius extracted from the initial-state radiation experiment at MAMI». In: *Eur. Phys. J. A* 57.3 (2021), p. 107. DOI: `10.1140/epja/s10050-021-00414-x`.

[16] A. Beyer, L. Maisenbacher, A. Matveev, et al. «The Rydberg constant and proton size from atomic hydrogen». In: *Science* 358.6359 (2017), pp. 79–85. DOI: `10.1126/science.aah6677`.

[17] H. Fleurbaey, S. Galtier, S. Thomas, et al. «New Measurement of the $1S-3S$ Transition Frequency of Hydrogen: Contribution to the Proton Charge Radius Puzzle». In: *Phys. Rev. Lett.* 120 (18 2018), p. 183001. DOI: `10.1103/PhysRevLett.120.183001`.

[18] N. Bezginov, T. Valdez, M. Horbatsch, et al. «A measurement of the atomic hydrogen Lamb shift and the proton charge radius». In: *Science* 365.6457 (2019), pp. 1007–1012. DOI: `10.1126/science.aau7807`.

[19] A. Grinin, ed. *Two-photon frequency comb spectroscopy of atomic hydrogen. PhD Thesis in Physics at the Ludwig Maximilian University of Munich.* 2024. DOI: `10.5282/edoc.27002`. URL: `https://edoc.ub.uni-muenchen.de/27002/` (visited on 2024).

[20] A. D. Brandt, S. F. Cooper, C. Rasor, et al. «Measurement of the $2S_{1/2}-8D_{5/2}$ Transition in Hydrogen». In: *Phys. Rev. Lett.* 128 (2 Jan. 2022), p. 023001. DOI: `10.1103/PhysRevLett.128.023001`.

[21] W. Xiong and C. Peng. «Proton Electric Charge Radius from Lepton Scattering». In: *Universe* 9.4 (2023). DOI: `10.3390/universe9040182`.

[22] P. Amaro, A. Adamczak, M. Abdou Ahmed, et al. «Laser excitation of the 1s-hyperfine transition in muonic hydrogen». In: *SciPost Phys.* 13 (2022), p. 020. DOI: `10.21468/SciPostPhys.13.2.020`.

[23] C. Pizzolotto, A. Adamczak, D. Bakalov, et al. «The FAMU experiment: muonic hydrogen high precision spectroscopy studies». In: *Eur. Phys. J. A* 56 (2020), p. 185. DOI: `10.1140/epja/s10050-020-00195-9`.

[24] S. Kanda, K. Ishida, M. Iwasaki, et al. «Measurement of the proton Zemach radius from the hyperfine splitting in muonic hydrogen atom». In: *Journal of Physics: Conference Series* 1138.1 (2018), p. 012009. DOI: `10.1088/1742-6596/1138/1/012009`.

[25] D. Findlay, J. Thomason, S. Fletcher, et al., eds. *FAMU experiment website*. URL: `https://web.infn.it/FAMU/the-project/` (visited on 2024).

[26] S. Kanda, ed. *Measurement of the proton Zemach radius from the hyperfine splitting in muonic hydrogen atom. presentation at the PSAS2018 Conference*. URL: `https://indico.cern.ch/event/671322/contributions/2949167/` (visited on 2024).

[27] C. Peset and A. Pineda. «Model-independent determination of the two-photon exchange contribution to hyperfine splitting in muonic hydrogen». In: *J. High Energ. Phys.* 60 (2017). DOI: `10.1007/JHEP04(2017)060`.

[28] O. Tomalak. «Two-photon exchange correction to the Lamb shift and hyperfine splitting of S levels». In: *Eur. Phys. J. A* 55.64 (2019). DOI: `10.1140/epja/i2019-12743-1`.

[29] F. Hagelstein, V. Lensky, and V. Pascalutsa. «Chiral perturbation theory of the hyperfine splitting in (muonic) hydrogen». In: *Eur. Phys. J. C* 83.762 (2023). DOI: `10.1140/epjc/s10052-023-11866-4`.

[30] D. Ruth, K. Slifer, J.-P. Chen, et al. «New spin structure constraints on hyperfine splitting and proton Zemach radius». In: *Physics Letters B* 859 (2024), p. 139116. DOI: `10.1016/j.physletb.2024.139116`.

[31] A. Dupays, A. Beswick, B. Lepetit, et al. «Proton Zemach radius from measurements of the hyperfine splitting of hydrogen and muonic hydrogen». In: *Phys. Rev. A* 68 (5 2003), p. 052503. DOI: `10.1103/PhysRevA.68.052503`.

[32] A. Volotka, V. Shabaev, G. Plunien, et al. «Zemach and magnetic radius of the proton from the hyperfine splitting in hydrogen». In: *Eur. Phys. J. D* 33 (2005), pp. 23–27. DOI: `10.1140/epjd/e2005-00025-9`.

[33] J.L. Friar and I. Sick. «Zemach moments for hydrogen and deuterium». In: *Physics Letters B* 579.3 (2004), pp. 285–289. DOI: `10.1016/j.physletb.2003.11.018`.

[34] T. Okumura, T. Azuma, D.A. Bennett, et al. «Deexcitation Dynamics of Muonic Atoms Revealed by High-Precision Spectroscopy of Electronic K X Rays». In: *Phys. Rev. Lett.* 127 (5 2021), p. 053001. DOI: `10.1103/PhysRevLett.127.053001`.

[35] T.P. Gorringe and D.W. Hertzog. «Precision muon physics». In: *Progress in Particle and Nuclear Physics* 84 (2015), pp. 73–123. DOI: `10.1016/j.ppnp.2015.06.001`.

[36] D.F. Measday. «The nuclear physics of muon capture». In: *Physics Reports* 354.4 (2001), pp. 243–409. DOI: `10.1016/S0370-1573(01)00012-6`.

[37] M. Cataldo, ed. *Optimization of negative muon experiments for elemental analysis at the RIKEN-RAL facility. PhD Thesis in Physics at the University of Milano-Bicocca.* 2024. URL: `https://hdl.handle.net/10281/472079` (visited on 2024).

[38] T. Yamazaki, K. Nagamine, S. Nagamiya, et al. «Negative muon spin rotation». In: *Physica Scripta* 11 (1975), pp. 133–139. DOI: `10.1088/0031-8949/11/3-4/004`.

[39] T. Suzuki, D. F. Measday, and J. P. Roalsvig. «Total nuclear capture rates for negative muons». In: *Phys. Rev. C* 35 (6 1987), pp. 2212–2224. DOI: `10.1103/PhysRevC.35.2212`.

[40] D.R. Zinatulina. «Electronic Catalogue of Mesoroentgen Spectra». In: *Phys. Atom. Nuclei* 82 (2019), pp. 243–249. DOI: `10.1134/S1063778819030165`.

[41] R. Engfer et al. «Charge-distribution parameters, isotope shifts, isomer shifts, and magnetic hyperfine constants from muonic atoms». In: *Atomic Data and Nuclear Data Tables* 14.5 (1974). Nuclear Charge and Moment Distributions, pp. 509–597. DOI: `10.1016/S0092-640X(74)80003-3`.

[42] S. Sturniolo and A. Hillier. «Mudirac: A Dirac equation solver for elemental analysis with muonic X-rays». In: *X-Ray Spectrometry* 50.3 (2021), pp. 180–196. DOI: `10.1002/xrs.3212`.

[43] D. Bakalov et al. «Experimental method to measure the hyperfine splitting of muonic hydrogen (μ-p)1S». In: *Physics Letters A* 172.4 (1993), pp. 277–280. DOI: `10.1016/0375-9601(93)91021-V`.

[44] A. Adamczak, G. Baccolo, S. Banfi, et al. «The FAMU experiment at RIKEN-RAL to study the muon transfer rate from hydrogen to other gases». In: *Journal of Instrumentation* 13.12 (2018), P12033. DOI: `10.1088/1748-0221/13/12/P12033`.

[45] E. Mocchiutti, A. Adamczak, D. Bakalov, et al. «First measurement of the temperature dependence of muon transfer rate from muonic hydrogen atoms to oxygen». In: *Physics Letters A* 384.26 (2020), p. 126667. DOI: `10.1016/j.physleta.2020.126667`.

[46] C. Pizzolotto, A. Sbrizzi, A. Adamczak, et al. «Measurement of the muon transfer rate from muonic hydrogen to oxygen in the range 70-336 K». In: *Physics Letters A* 403 (2021), p. 127401. DOI: `10.1016/j.physleta.2021.127401`.

[47] A. Werthmüller, A. Adamczak, R. Jacot-Guillarmod, et al. «Energy dependence of the charge exchange reaction from muonic hydrogen to oxygen». In: *Hyperfine Interactions* 116 (1998), pp. 1–16. DOI: `10.1023/A:1012618721239`.

[48] A. D. Hillier et al. «Muons at ISIS». In: *Philosophical Transactions of the Royal Society A* 377.2137 (2019), p. 20180064. DOI: `10.1098/rsta.2018.0064`.

[49] T. Matsuzaki, K. Ishida, K. Nagamine, et al. «The RIKEN-RAL pulsed Muon Facility». In: *NIM A* 465.2 (2001), pp. 365–383. DOI: `10.1016/S0168-9002(01)00694-5`.

[50] A.P. Letchford et al. «Testing, Installation, Commissioning and First Operation of the ISIS RFQ Pre-Injector Upgrade». In: *Proceedings of the 2005 Particle Accelerator Conference*. 2005, pp. 695–697. DOI: `10.1109/PAC.2005.1590531`.

[51] J.W.G. Thomason. «The ISIS Spallation Neutron and Muon Source—The first thirty-three years». In: *NIM A* 917 (2019), pp. 61–67. DOI: `10.1016/j.nima.2018.11.129`.

[52] D. Findlay, J. Thomason, S. Fletcher, et al., eds. *A Practical Guide to the ISIS Neutron and Muon Source*. 2021. URL: `https://www.isis.stfc.ac.uk/Pages/News21_PracticalGuide.aspx`.

[53] G.H. Eaton, A. Carne, S.F.J. Cox, et al. «Commissioning of the Rutherford Appleton Laboratory pulsed muon facility». In: *NIM A* 269.3 (1988), pp. 483–491. DOI: `10.1016/0168-9002(88)90124-6`.

[54] S.J. Blundell et al. «Chapter 13: making muons». In: *Muon Spectroscopy: An Introduction*. Oxford University Press, 2021. DOI: `10.1093/oso/9780198858959.003.0013`.

[55] R. Rossini, G. Baldazzi, S. Banfi, et al. «The muon beam monitor for the FAMU experiment: design, simulation, test, and operation». In: *Frontiers in Detector Science and Technology* 2 (2024). DOI: `10.3389/fdest.2024.1438902`.

[56] R. Rossini, A. Adamczak, D. Bakalov, et al. «Status of the detector setup for the FAMU experiment at RIKEN-RAL for a precision measurement of the Zemach radius of the proton in muonic hydrogen». In: *Journal of Instrumentation (JINST)* 19.02 (2024), p. C02034. DOI: `10.1088/1748-0221/19/02/C02034`.

[57] D. Bakalov and M. Stoilov. «Toward the measurement of the hyperfine structure of muonic hydrogen in the FAMU experiment: Multi-pass cavity optimization for experiments with pulsed sources». In: *EPJ Web of Conferences* 181.01033 (2018). DOI: `10.1051/epjconf/201818101033`.

[58] M. Baruzzo, J.J. Suárez-Vargas, L.I. Stoychev, et al. «A mid-IR laser source for muonic hydrogen spectroscopy: The FAMU laser system». In: *Optics & Laser Technology* 179 (2024), p. 111375. DOI: `10.1016/j.optlastec.2024.111375`.

[59] R. Rossini for the FAMU Collaboration. «The 2024 LaBr3(Ce) detector setup for the FAMU experiment». In: *NIM A* 1069 (2024), p. 169953. DOI: `10.1016/j.nima.2024.169953`.

[60] G. Baldazzi, A. Vacchi, C. Labanti, et al. «The LaBr3(Ce) based detection system for the FAMU experiment». In: *Journal of Instrumentation (JINST)* 12 (2017), p. C03067. DOI: `10.1088/1748-0221/12/03/C03067`.

[61] M. Bonesini, R. Benocci, R. Bertoni, et al. «Large area LaBr3:Ce crystals read by SiPM arrays with improved timing and temperature gain drift control». In: *NIM A* 1046 (2023), p. 167677. DOI: `10.1016/j.nima.2022.167677`.

[62] M. Bonesini, R. Bertoni, R. Benocci, et al. «One inch LaBr3:Ce detectors, with temperature control and improved time resolution for low energy X-rays spectroscopy». In: *Proceedings of Science* 398 (2022), p. 770. DOI: `10.22323/1.398.0770`.

[63] M. Bonesini, R. Bertoni, A. Abba, et al. «Improving the time resolution of large area LaBr3:Ce detectors with SiPM array readout». In: *Condensed Matter* 4 (8 2023), p. 99.

[64] R. Rossini, O. Cremonesi, M. Cataldo, et al. «The role of gamma-ray spectrometry and Monte Carlo simulation in the characterisation of meteorites». In: *J. Radioanal. Nucl. Chem. (JRNC)* 333 (7 2024), pp. 3571–3575. DOI: `10.1007/s10967-023-09296-3`.

[65] C. Alduino, K. Alfonso, D. R. Artusa, et al. «The projected background for the CUORE experiment». In: *Eur. Phys. J. C* 77 (8 2017), p. 543. DOI: `10.1140/epjc/s10052-017-5080-6`.

[66] S. Agostinelli, J. Allison, K. Amako, et al. «Geant4—a simulation toolkit». In: *NIM A* 506.3 (2003), pp. 250–303. DOI: `10.1016/S0168-9002(03)01368-8`.

[67] M. Soldani, G. Ballerini, M. Bonesini, et al. «High performance DAQ for muon spectroscopy experiments». In: *NIM A* 936 (2019), pp. 327–328. DOI: `10.1016/j.nima.2018.11.003`.

[68] R. Rossini, R. Benocci, R. Bertoni, et al. «Characterisation of a low-momentum high-rate muon beam monitor for the FAMU experiment at the CNAO-XPR beam facility». In: *Journal of Instrumentation (JINST)* 19.01 (2024), p. C01024. DOI: `10.1088/1748-0221/19/01/C01024`.

[69] M. Bonesini, R. Bertoni, F. Chignoli, et al. «The construction of the Fiber-SiPM beam monitor system of the R484 and R582 experiments at the RIKEN-RAL muon facility». In: *Journal of Instrumentation (JINST)* 12.3 (2017), p. C03035. DOI: `10.1088/1748-0221/12/03/C03035`.

[70] M. Bonesini, R. Benocci, R. Bertoni, et al. «The upgraded beam monitor system of the FAMU experiment at RIKEN–RAL». In: *NIM A* 936 (2019), pp. 592–594. DOI: `10.1016/j.nima.2018.08.092`.

[71] R. Rossini, R. Benocci, R. Bertoni, et al. «Characterisation of muon and proton beam monitors based on scintillating fibres with a SiPM readout». In: *NIM A* 1046 (2023), p. 167684. DOI: `10.1016/j.nima.2022.167684`.

[72] R. Rossini, R. Benocci, R. Bertoni, et al. «Characterisation of a scintillating fibre-based hodoscope exposed to the CNAO low-energy proton beam». In: *NIM A* 1046 (2023), p. 167746. DOI: `10.1016/j.nima.2022.167746`.

[73] R. Brun and F. Rademakers. «ROOT — An object oriented data analysis framework». In: *NIM A* 389.1 (1997), pp. 81–86. DOI: `10.1016/S0168-9002(97)00048-X`.

[74] G. Battistoni, T. Boehlen, F. Cerutti, et al. «Overview of the FLUKA code». In: *Annals of Nuclear Energy* 82 (2015), pp. 10–18. DOI: `10.1016/j.anucene.2014.11.007`.

[75] C. Ahdida, D.. Bozzato, D. Calzolari, et al. «New Capabilities of the FLUKA Multi-Purpose Code». In: *Frontiers in Physics* 9 (2022), p. 788253. DOI: `10.3389/fphy.2021.788253`.

[76] V. Vlachoudis. «Flair: A powerful but user friendly graphical interface for FLUKA». In: *International Conference on Mathematics, Computational Methods & Reactor Physics 2009*. 2009, pp. 790–800.

List of publications

- **R. Rossini, G. Baldazzi, S. Banfi, et al., "The muon beam monitor for the FAMU experiment: design, simulation, test, and operation," Frontiers in Detector Science and Technology, vol. 2, 2024, issn: 2813-8031. doi: 10.3389/fdest.2024.1438902.** *This paper contains the core of the work carried out in this PhD thesis.*

- R. Rossini on behalf of the FAMU Collaboration, "The 2024 LaBr3(Ce) detector setup for the FAMU experiment", acceptet for publication on NIM A.

- R. Rossini on behalf of the FAMU Collaboration, "First operations of the FAMU experiment at RIKEN-RAL", submitted to Proceedings of Science.

- R. Rossini, M. Bonesini, M. Cataldo, et al., "A muon beam monitor for the CHNet-MAXI experiment at the RIKEN-RAL laboratory", Nuclear Instruments and Methods in Physics Research Section A: Accelerators, Spectrometers, Detectors and Associated Equipment, vol. 1069, p. 169 894, 2024. doi: 10.1016/j.nima.2024.169824.

- R. Rossini, A. Adamczak, D. Bakalov, et al., "Status of the detector setup for the FAMU experiment at RIKEN-RAL for a precision measurement of the Zemach radius of the proton in muonic hydrogen," Journal of Instrumentation, vol. 19, no. 02, p. C02034, 2024. doi: 10.1088/1748-0221/19/02/C02034.

- R. Rossini, R. Benocci, R. Bertoni, et al., "Characterisation of a low-momentum high-rate muon beam monitor for the FAMU experiment at the CNAO-XPR beam facility," Journal of Instrumentation, vol. 19, no. 01, p. C01024, 2024. doi: 10.1088/1748-0221/19/01/C01024.

- R. Rossini, M. Bonesini, M. Cataldo, et al., "A muon beam monitor for the CHNet-MAXI experiment at the RIKEN-RAL laboratory," NIM A, vol. 1069, p. 169 824, 2024, issn: 0168-9002. Doi: 10.1016/j.nima.2024.169824

- M. Bonesini, R. Benocci, R. Bertoni, et al., “Large area LaBr3:Ce crystals read by SiPM arrays with improved timing and temperature gain drift control,” NIM A, vol. 1046, p. 167 677, 2023, issn: 0168-9002. doi: 10.1016/j.nima.2022.167677.

- M. Bonesini, R. Benocci, R. Bertoni, et al., “One inch LaBr3:Ce detectors, with temperature control and improved time resolution for low energy x-rays spectroscopy,” PoS, vol. EPS-HEP2023, p. 547, 2023. doi: 10.22323/1.449.0547.

- M. Bonesini, C. De Vecchi, A. Menegolli, et al., “Comparison of new SiPM devices for applications in High-Energy Physics,” NIM A, vol. 1047, p. 167 903, 2023, issn: 0168-9002. doi: 10.1016/j.nima.2022.167903.

- A. Vacchi, E. Mocchiutti, A. Adamczak, et al., “Investigating the proton structure: The FAMU experiment,” Nuclear Physics News, pp. 1–8, 2023. doi: 10.1080/10619127.2023.2198913.

Research papers not related to the activity in the FAMU experiment:

- A. Menegolli, G. Raselli, S. Copello, et al., “A goniometric measurement system for reflection, diffusion, and transmission characterization in the VUV range,” Nuclear Instruments and Methods in Physics Research Section A: Accelerators, Spectrometers, Detectors and Associated Equipment, vol. 1066, p. 169 666, 2024. doi: 10.1016/j.nima.2024.169666.

- G. Raselli, F. Boffelli, S. Copello, et al., “A cryogenic system for measuring in the VUV range the absolute quantum efficiency of light detectors with large sensitive area,” Nuclear Instruments and Methods in Physics Research Section A: Accelerators, Spectrometers, Detectors and Associated Equipment, vol. 1068, p. 169 807, 2024. doi: 10.1016/j.nima.2024.169807.

- R. Rossini, O. Cremonesi, M. Cataldo, D. Di Martino, M. Laubenstein, and M. Clemenza, “The role of gamma-ray spectrometry and Monte Carlo simulation in the characterisation of meteorites,” J Radioanal Nucl Chem, 2024. doi: 10.1007/s10967-023-09296-3.

- R. Rossini, R. Benocci, R. Bertoni, et al., “Characterisation of a scintillating fibre-based hodoscope exposed to the CNAO low-energy proton beam,” NIM A, vol. 1046, p. 167 746, 2023, issn: 0168-9002. doi: 10.1016/j.nima.2022.167746.

- R. Rossini, R. Benocci, R. Bertoni, et al., “Characterisation of muon and proton beam monitors based on scintillating fibres with a SiPM read-out,” NIM A, vol. 1046, p. 167 684, 2023, issn: 0168-9002. Doi: 10.1016/j.nima.2022.167684.

- A. Mazzinghi, L. Castelli, C. Ruberto, et al., “X-ray and neutron imaging for cultural heritage: The INFN-CHNet experience,” Eur. Phys. J. Plus, vol. 139, p. 635, 2024. Doi: 10.1140/epjp/s13360-024-05429-z.

- R. Rossini, M. Clemenza, D. Di Martino, et al., “Low-background gamma spectrometry and neutron diffraction in the study of stony meteorites,” Applied Radiation and Isotopes, vol. 193, p. 110 653, 2023, issn: 0969-8043. doi: 10.1016/j.apradiso.2023.110653.

- R. Rossini, D. Di Martino, T. Agoro, et al., “A new multidisciplinary non-destructive protocol for the analysis of stony meteorites: gamma spectroscopy, neutron and muon techniques supported by Raman microscopy and sem-eds,” J. Anal. At. Spectrom., vol. 38, pp. 293–302, 2 2023. Doi: 10.1039/D2JA00263A

- C. Petroselli, L. Bomben, S. Carsi, et al., “A portable γ spectroscopy detector for didactic applications,” Il Nuovo Cimento C, p. 191, 5 2023. doi: 10.1393/ncc/i2023-23191-9.

- M. Musa, R. Rossini, D. Di Martino, M. Riccardi, M. Clemenza, and G. Gorini, “Combining micro-Raman spectroscopy and scanning electron microscopy mapping: A stony meteorite study,” Materials, vol. 14, no. 24, 2021, issn: 1996-1944. doi: 10.3390/ma14247585.